VOL. 06 NO. 02

DECEMBER 2025

ISSN:2738-2184

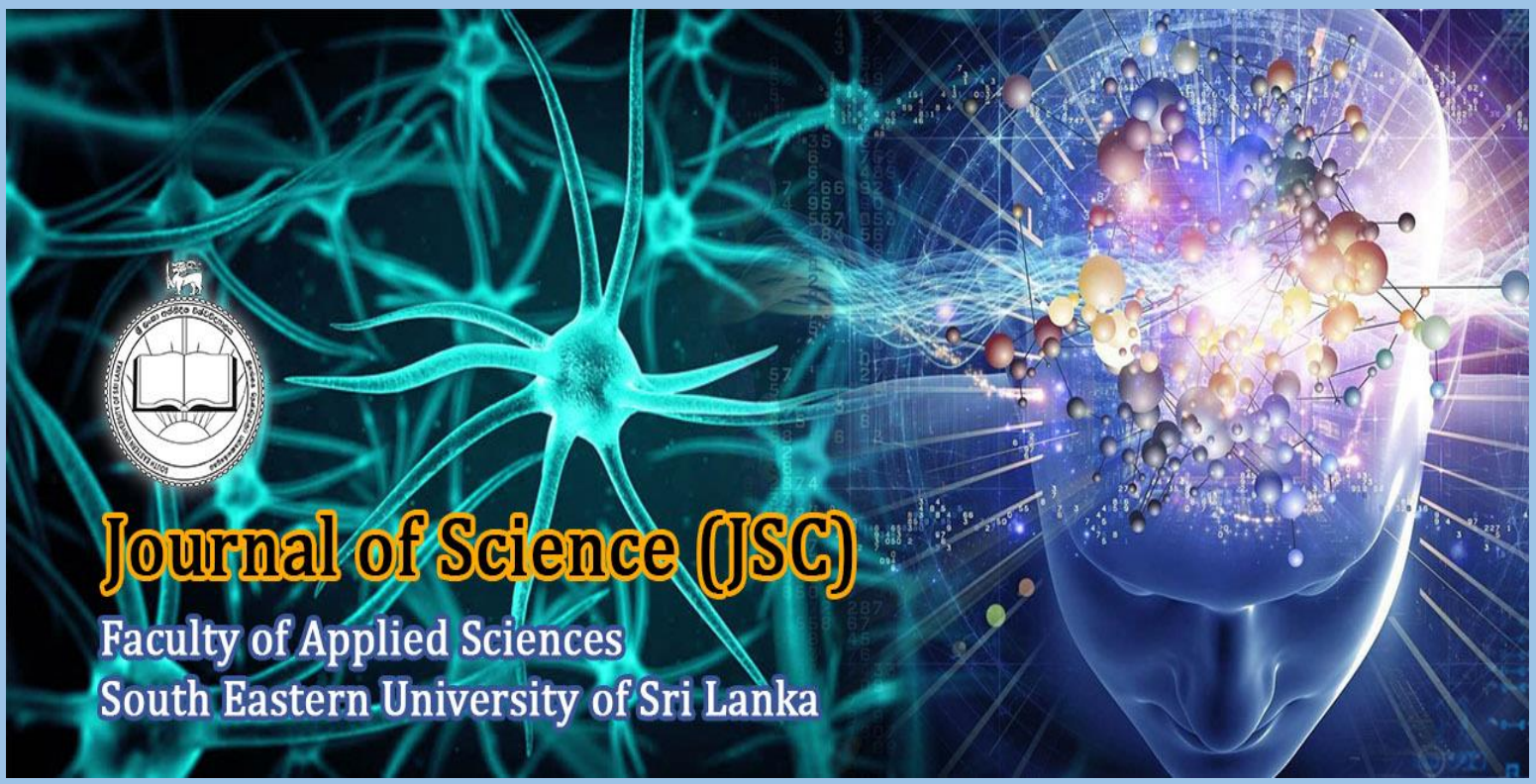

PUBLISHED BY FACULTY OF APPLIED SCIENCES

Journal of Science
Faculty of Applied Sciences

Volume 06 – Issue 02 (2025)

The Faculty of Applied Science is not answerable for the reports and opinions communicated by the authors of this Journal.

ISSN 2738-2184

Published by:
Faculty of Applied Sciences
South Eastern University of Sri Lanka
Sammanthurai 32200

JOURNAL OF SCIENCE
FACULTY OF APPLIED SCIENCES
SOUTH EASTREN UNIVERSITY OF SRI LANKA

ISSN: 2738-2184
@ https://www.seu.ac.lk/jsc

Journal of Science-FAS-SEUSL (2025) 06(02) 01-10
ISSN:2738-2184

Study on Semi-Analytical Solutions of Fractional Derivatives with Applications

M.M. Zathiha* and M.A.A.M. Faham

Department of Mathematical Sciences, Faculty of Applied Sciences, South Eastern University of Sri Lanka, Sammanthurai 32200

*zathiha@gmail.com

Abstract

Differential equations are very useful tools to formulate real-world phenomena into mathematical form. In recent years, fractional calculus has gained considerable attention in modeling diverse real-world phenomena in science and engineering fields due to its memory effects and hereditary properties. In this study, we aim to review the ideas of fractional derivatives and their applications in fluid dynamics studies. The Adomian's Decomposition Method (ADM) has used to semi-analytically solve the Riemann-Liouville non-linear fractional-order differential equations. The ADM has the iteration steps that lead to highly accurate results. The study can also be used for numerous model examples of fractional derivatives with initial and boundary conditions involve. Among the many interesting applications of fractional derivatives are complex viscoelastic media, electrical spectroscopy, porous media, cosmology, environmental science, medicine (the modeling of infectious diseases), and signal and image processing. When we consider the negative side of fractional-based models, they are computationally expensive, require enormous data storage requirements, and have a phenomenological description that does not necessarily reflect the physical mechanism behind the scenes.

Keywords: Adomian's Decomposition Method (ADM), Fractional derivatives, Semi-analytical solution techniques.

1. Introduction

Real-world problems can be formulated into mathematical form through the use of differential equations. The fractional calculus is getting considerable attention and has gained a special interest in modeling diverse real-world phenomena in science and engineering fields due to its memory effects and hereditary properties. A fractional derivative is the derivative of any arbitrary order, real or complex.

The memory means an existence of output (response, endogenous variable) at the present time that depends on the history of the change of the input (impact, exogenous variable) on a finite (or infinite) time interval. The memory can be described by the function that is called the memory function, which is a kernel of the integral-differential operator (Vasily E. Tarasova & Svetlana S. Tarasova, 2019). The hereditary property of the medium, i.e., the dependence of the current state of a dynamic system on its previous. Fractional operators used to illustrate better the reality of real-world phenomena with the hereditary property.

The ordinary classical models of integer-order derivatives are sometimes unable to model the proper complex dynamics applications. Since the integer-order differential operator is a local operator, whereas fractional-order derivatives involve non-local operator. This means that the next state of a system depends not only upon its current state but also upon all of its historical

Corresponding Author: zathiha@gmail.com

states. This is more realistic and it is one reason why fractional calculus has become more and more popular. This leads the fractional derivatives to be very convenient to describe such cases in chemistry, biology, mechanics, signal and image processing, and many more applications. Fractional operators used to illustrate better the reality of real-world phenomena with the hereditary property.

There is a huge range of fractional models in the literature, such as fractional Brownian motion, fractional neutron point kinetic model, power law, Riesz potential, dynamical systems, mechanical systems, computational fractional derivative equations, fractional filters, fractional transforms, fractional wavelets, geophysics, and fluid dynamics, etc.

The most widely accepted definition including the singular kernel was proposed by Riemann and Liouville–Caputo. The Caputo fractional derivative definition has appeared frequently in the porous media literature.

Furthermore, fractional-order boundary value problems of linear and nonlinear fractional differential equations have been extensively investigated by many authors. By applying various techniques, many researchers have studied the existence of solutions of linear and nonlinear fractional derivatives.

There are several different analytical and numerical methods have been proposed to solve fractional ordinary differential equations. Including, Linear fractional differential equations by Operational Methods, (Roberto Garra, 2012), Classical Laplace Transform, (Rogosin S. & Dubatovskaya M., 2018) and Adomian's Decomposition Method, (V. Daftardar-Geji and H. Jafari, 2005), Variation Iteration Method, and Adams-Bashforth-Moulton Method and many more.

The Adomian's Decomposition Method (ADM) has been shown to solve effectively, easily, and accurately a large class of linear and nonlinear problems, generally one or two iterations lead to high accurate solutions. This method provides the solution in a rapidly convergent series with components that are elegantly computed. The main advantage of the method is that it can be applied directly for all types of differential and integral equations, linear or nonlinear, homogeneous or inhomogeneous, with constant coefficients or with variable coefficients as the method does not need linearization, weak nonlinearity assumptions or perturbation theory. Another important advantage is that the method is capable of greatly reducing the size of computation work while still maintaining high accuracy of the numerical solution.

In this paper, we aim to analyze the study regarding the linear and nonlinear fractional derivatives and its application in real-world phenomena of science and engineering fields. Also, highlight their advantages over conventional continuum flow models toward reservoir simulation and management. Then, we tend to use the semi-analytic solving method of Adomian's Decomposition Method to derive the solutions for the test examples chosen. Also further establish and extend the usage of the fractional derivative applications using experimental studies.

2. Background of Study

The work of fractional calculus is carried out in a large number of articles. Including (Rogosin S. & Dubatovskaya M., 2018), present the essence of two important approaches in the fractional calculus, namely, those developed by Letnikov and Marchaud. The authors collect the most important results for the corresponding fractional derivatives, compare these constructions and its applications.

(Farnaz, Mubashir Qayyum, Syed Inayat Ali Shah, & Sha, 2021), analyzed in fractional space on Oldroyd-6 fluid in thin film flow context for both lifting and drainage scenarios. The posed highly nonlinear boundary value ordinary differential equations of the problem are converted into fractional differential equations.

(Anupama Choudhary, Devendra Kumar, & Jagdev Singh, 2016), discussed a fractional model arising in flow of two incompatible liquids through homogenous porous media with mean capillary pressure. The solution is derived by the application of the Sumudu transform and the Fourier sine transform.

(Umair Ali, 2012), suggested fractional functional for the Adomian's Decomposition Method (ADM) to solve the nonlinear fractional order partial differential equations with fractional order initial and boundary conditions by using the modified Riemann–Liouville fractional derivative proposed by G. Jumarie. The proposed modification in Adomian's Decomposition Method has made the results more powerful and efficient than before in finding analytical as well as numerical solutions for a wide class of linear and nonlinear fractional differential equations.

From among many advanced numerical methods applied to calculation, one of the widely applied techniques are perturbation methods. In 1999, Ji Huan, has proposed a new perturbation technique coupled with the Homotopy technique, which is called the Homotopy Perturbation Method (HPM), (He J.H, 1999). The HPM has attracted the attention of researchers in recent years with many advantages is the fact that it produces the approximate solution quite fast and results are more reliable comparing other numerical methods.

Furthermore, the Homotopy Perturbation Method (HPM), which gives the approximate solutions for nonlinear fractional differential equations and also used as numerical solution for multi-order fractional derivatives. This method, which is a coupling of the traditional perturbation method and homotopy in topology, deforms continuously to a simple problem which is easily solved. This method does not require a small parameter in an equation, has a significant advantage in that it provides an analytical approximate solution to a wide range of nonlinear problems in applied sciences.

(Z.Z. Ganji, 2008), applied the homotopy perturbation method (HPM) to fractional differential equations and revealed that the HPM is an alternative analytical method for fractional differential equations. (Odibat., 2007), presented the modified homotopy perturbation method for calculating approximate solutions for nonlinear partial differential equations of fractional order. The results obtained using this method gave very high accuracy comparing with the variation of iteration method. (Rizwan Ali , Muhammad Imran Asjad, & Ali Akgül , 2021) , have analyzed the mathematical fractional model of hybrid viscous nanofluids and its application in heat and mass transfer. Which explains the application of novel way of modeling of heat and mass transfer flow

of hybrid nanofluid (Aluminum and Copper) for different base fluid water and engine oil. The governing equations for energy and momentum equations are developed with Caputo fractional power law derivative through constitutive relations. The flow of nanofluids confined between the two parallel plates with distanced apart. This model can be solved by means of the Laplace transform technique. Statically analysis for Nusselt number and Sherwood number is also discussed.

The gas transport in heterogeneous media has been studied by (HongGuang Suna, Yong Zhang, Dumitru Baleanu, Wen Chen, & YangQuan Chen, 2018). The gas transport in heterogeneous media has an important influence on oil-gas exploitation and development. Therefore, injecting gas into oil or gas reservoirs can significantly reduce oil viscosity, mitigate atmospheric emissions and control climate change to enhance oil or gas recovery efficiency and protect the environment. However, it is well-known that the random motion in gas transport in natural reservoirs deviates from the normal Brownian motion whose scaling limit cannot be properly described by classical models (such as Darcy's law and the advection dispersion equation) due to heterogeneity and complexity of the medium structure.

Anomalous transport of gas exhibits obvious path and history dependent behaviors. Subsequently, the fractional derivative models have been applied to explain the time memory and space non-locality in gas transport. Applicability of the fractional derivative models have been efficiently verified by employing a set of experimental data in the literature which are compared well with the results of numerical simulation and analytical solution. (Ailian Chang, HongGuang Sun, Yong Zhang, & Chunmiao , 2018).

3. Application of Fractional derivatives in Fluid flow

Recently, great interest has been devoted to the application of fractional derivative modelling to different fields of science and engineering. Among the many interesting applications of fractional calculus to physical systems, complex viscoelastic media, electrical spectroscopy, porous media, cosmology, environmental science, signal and image processing, medicine (the modelling of infectious diseases), and materials, etc.

In fluid mechanics, fluid flow through porous media is the manner in which fluids behave when flowing through a porous media, for example sponge or wood, or when filtering water using sand or another porous material. Classical flow mechanics in porous media assumes that the medium is homogenous, isotropic, and has an intergranular pore structure.

Further, many research articles demonstrating the application of the fractional derivative concept in reservoir engineering discipline as well. For example, there are studies related to modelling the long-tailed non Fickian solute transport in fractured porous rock, fluid flow in naturally fractured nano-porous media, anomalous heat transport in heterogeneous media, modelling fluid flow in thermally altered zones in porous media and many more (Caputo, 1967). Accurate modelling of heat transport in fractured porous media is essential for the applications of geothermal reservoirs, thermal enhanced oil recovery and reservoir management, that is, detection of water influx in the wellbore.

Reservoir Engineering is a branch of petroleum engineering that applies scientific principles to the fluid flow through porous medium during the development and production of oil and gas

reservoirs so as to obtain a high economic recovery. The working tools of the reservoir engineer are subsurface geology, applied mathematics, and the basic laws of physics and chemistry governing the behavior of liquid and vapor phases of crude oil, natural gas, and water in reservoir rock.

A detailed description of the pore network and the adequate description of the rheological behavior of the complex reservoir fluid(s) are fundamental to the accuracy of any fluid flow model developed to describe flow through reservoir rocks. (Hossain et al, 2008) attempted to address the issue of incorporating the time dependency of rock and fluid properties explicitly into the existing fluid flow models. The authors introduced a memory model to capture the time evolution of rock and fluid properties with time employing the fractional derivative concept. Furthermore, the parameters of the resulting fractional derivative models have clear physical significance and must be obtained from a data fitting of experimental or field measurements.

Also, when we consider the negative side of the fractional-based models, which are computationally expensive and require enormous data storage requirement and are of a phenomenological description which does not necessarily reflect the physical mechanism behind the scenes.

4. Methodology

Fractional derivatives are a branch of mathematical analysis that studies the several different possibilities of defining real number or complex number orders of derivatives. Historically, the concept of fractional derivatives can be traced back to Leibniz's letter to L'Hopital in 1695, where the derivative of a non-integer order (1/2) was mentioned. It can also be applicable in the field of fluid dynamics, where fractional-order models are used to capture memory effects and anomalous transport phenomena. In methodology, fractional derivatives are introduced through definitions such as Riemann–Liouville, Caputo, or Grünwald–Letnikov, which provide the mathematical framework for applying these concepts to physical systems.

4.1 Basic definitions of the fractional derivatives:

4.1.1 The Riemann – Liouville derivative of fractional order *α* of function *x*(*t*):

$$ {}_aD_x^{\alpha} f(x) = \frac{d^n}{dx^n}\, {}_aI_x^{n-\alpha} f(x) = \frac{d^n}{dt^n}\, \frac{1}{\Gamma(\mathrm{n}-\alpha)} \int_a^x (x-t)^{n-\alpha-1} f(t)\, dt \ , \qquad ------ \ (1) $$

where the Riemann – Liouville operator is given by

$$ {}_aI_x^{\alpha} = \frac{1}{\Gamma(\alpha)} \int_a^x (x-t)^{\alpha-1} f(t)\, dt $$

and $n-1 \leq \alpha \leq n \in \mathbb{Z}^+$.

4.1.2 The Caputo derivative of fractional order α of function x(t):

$$ {}_aD_x^{\alpha} f(x) = D_x^{-(n-\alpha)} \frac{d^n}{dx^n} f(x) = \frac{1}{\Gamma(\mathrm{n}-\alpha)} \int_a^x (x-t)^{n-\alpha-1} f^m(t)\, dt \,, \quad ------ (2) $$

From this definition, one can see that ${}_aD_x^{\alpha} f^{(m)}(x) = {}_aD_x^{\alpha+m} f(x)$, and the gamma function

$$ \Gamma = \int_0^{\infty} t^{z-1} e^{-t}\, dx $$

.

4.2 Solutions Methods of the Fractional Derivatives: Adomian's Decomposition Method:

The Adomian's Decomposition Method (ADM) provides the solution in a rapidly convergent series with components that are elegantly computed. The main advantage of the method is that it can be applied directly for all types of differential and integral equations, linear or nonlinear, homogeneous or inhomogeneous, with constant coefficients or with variable coefficients as the method does not need linearization, weak nonlinearity assumptions or perturbation theory.
Another important advantage is that the method is capable of greatly reducing the size of computation work while still maintaining high accuracy of the numerical solution.

The basic idea of the Adomian's decomposition method is to decompose the unknown equation

$$ F(y) = g(t) \quad ------ (3) $$

First, the whole equation is decomposed into several parts as, $F = L + R + N$

Therefore, $F(y) = L(y) + R(y) + N(y) = g(t).$

That is, $L(y) = g(t) - R(y) - N(y)$.

Where L – Highest order derivative and easily invertible
R – Linear differential operator of order less than L
g – Source term
N – Nonlinear term satisfies Lipschitz condition.

The function $y(t)$ is assumed to be bounded for all $t \in I = [0,1]$. Choose suitable operator L such that L^{-1} exists, then operator L^{-1} is used to act on both sides of this equation, obtaining

$$ y = L^{-1} g - L^{-1} R(y) - L^{-1} N(y) + \Phi \quad , \quad -------- (4) $$

where, the term of Φ satisfies $L(\Phi) = 0$.

If we decompose the true solution y of the equation into the sum of infinity components of different degree solutions. That is,

$$ y = \sum_{n=0}^{\infty} y_n $$

The nonlinear term $N(y)$ is decomposed into the sum of infinite number Adomian's polynomials of $A_n(y_0, y_1, \ldots, y_n)$.

$$ A_n = \frac{1}{n!} \frac{d^n}{d\lambda^n} N\left(\sum_{i=0}^{n} \lambda^i y_i\right) \quad at\ \lambda = 0 \quad ------(5) $$

Then the equation (4) can be written as

$$\sum_{n=0}^{\infty} y_n = L^{-1}\, g - L^{-1}\, R\left(\sum_{n=0}^{\infty} y_n\right) - L^{-1}\left(\sum_{n=0}^{\infty} A_n\right) + \Phi \qquad ------(6)$$

Now the Adomian's decomposition satisfies the following recurrence relation:

$$\begin{aligned} y_0 &= L^{-1}\, g + \Phi \\ y_1 &= -L^{-1}\, R(y_0) - L^{-1}\, A_0 \\ y_2 &= -L^{-1}\, R(y_1) - L^{-1}\, A_1 \\ y_{m+1} &= -L^{-1}\, R(y_m) - L^{-1}\, A_m \qquad ------(7) \end{aligned}$$

5. Results and Discussion

This section presents an example of applying the Adomian's decomposition method to solve fractional non-linear ordinary differential equations.

5.1 Model Example of the non-linear Fractional Derivative:

1. $\dfrac{dy}{dt} + \dfrac{d^{\frac{1}{2}}y}{dt^{\frac{1}{2}}} - 2y^2 = 0 \qquad ------(i)$

Solution:

Consider the linear operator $L = \frac{d}{dx} \quad \Rightarrow \quad L^{-1} = \int .\, dt$

Non-linear term $N(y) = y^2$

Now the equation (i) can be written as $L(y) = -\dfrac{d^{\frac{1}{2}}y}{dt^{\frac{1}{2}}} + 2y^2$ which implies

$$L^{-1} \Rightarrow \quad y = C - L^{-1}\left(\frac{d^{\frac{1}{2}}y}{dt^{\frac{1}{2}}}\right) + 2\, L^{-1}(y^2) \qquad ------(ii)$$

where C is an arbitrary integral constant.

Since L is a linear operator, we get

$$\begin{aligned} y &= C - \frac{d^{-\frac{1}{2}}y}{dt^{-\frac{1}{2}}} + 2\, L^{-1}(y^2) \\ &= C - I^{\frac{1}{2}}(y) + 2\, L^{-1}(y^2) \qquad ------(ii) \end{aligned}$$

Where I is the Riemann-Liouville operator, and

$$I^{\alpha}(t^n) = \frac{\Gamma(n+1)}{\Gamma(n+\alpha+1)}\, t^{n+\alpha}\,.$$

Then the Adomian's decomposition solution is given by

$$y = \sum_{n=0}^{\infty} y_n = y_0 + y_1 + y_2 + \cdots$$

For the non-linear form is

$$N(y) = \sum_{n=0}^{\infty} A_n \quad ; \quad A_n = \frac{1}{n!}\frac{d^n}{d\lambda^n} N\left(\sum_{i=0}^{n} \lambda^i y_i\right) \quad at\ \lambda = 0\,. \quad ------(iii)$$

So, the equation (ii) is written as

$$\sum_{n=0}^{\infty} y_n = C - I^{\frac{1}{2}}\left(\sum_{n=0}^{\infty} y_n\right) + 2\,L^{-1}\left(\sum_{n=0}^{\infty} A_n\right) \qquad ----------(iv)$$

Equating both-sides in the equation (iv) we get

$$y_0 = C \quad ,$$

$$y_{n+1} = -I^{\frac{1}{2}}\left(\sum_{n=0}^{\infty} y_n\right) + 2\,L^{-1}\left(\sum_{n=0}^{\infty} A_n\right) \quad , \ for\ n \geq 0\,.$$

<u>For $n = 0$</u>: $\boldsymbol{y_1 = -I^{\frac{1}{2}}(y_0) + 2\,L^{-1}(A_0)}$ $\qquad ------(v)$

Using the equation (iii) we have $N(y) = y^2$, therefore

$$A_0 = N(y_0) = {y_0}^2 = C^2\,.$$

Then the equation (v) gives, when substituting $\alpha = \frac{1}{2}$

$$y_1 = -I^{\frac{1}{2}}(C) + 2\int C^2\,dt = -I^{\frac{1}{2}}(Ct^0) + 2\int C^2\,dt = C\left[\frac{\Gamma(1)}{\Gamma\left(\frac{3}{2}\right)}\,t^{\frac{1}{2}}\right] + 2\,C^2 t$$

$$= -2C\,\frac{\sqrt{t}}{\sqrt{\pi}} + 2\,C^2 t\,. \qquad \left(\because\ \Gamma(1) = 0! = 1 \ \ and\ \Gamma\left(\frac{3}{2}\right) = \frac{1}{2}\sqrt{\pi}\right)$$

Using the equation (iii) we have $N(y) = y^2$, therefore

$$A_0 = N(y_0) = {y_0}^2 = C^2\,.$$

Then the equation (v) gives, when substituting $\alpha = \frac{1}{2}$

$$y_1 = -I^{\frac{1}{2}}(C) + 2\int C^2\,dt = -I^{\frac{1}{2}}(Ct^0) + 2\int C^2\,dt = C\left[\frac{\Gamma(1)}{\Gamma\left(\frac{3}{2}\right)}\,t^{\frac{1}{2}}\right] + 2\,C^2 t$$

$$= -2C\,\frac{\sqrt{t}}{\sqrt{\pi}} + 2\,C^2 t\,. \qquad \left(\because\ \Gamma(1) = 0! = 1 \ \ and\ \Gamma\left(\frac{3}{2}\right) = \frac{1}{2}\sqrt{\pi}\right)$$

$$---(vi)$$

<u>For $n = 1$</u>: $\boldsymbol{y_2 = -I^{\frac{1}{2}}(y_1) + 2\,L^{-1}(A_1)}$ $\qquad ------(vii)$

Consider the Riemann-Liouville operator

$$I^{\frac{1}{2}}(y_1) = I^{\frac{1}{2}}\left(-2C\,\frac{\sqrt{t}}{\sqrt{\pi}} + 2\,C^2 t\right) = -\frac{2C}{\sqrt{\pi}} I^{\frac{1}{2}}\left(t^{\frac{1}{2}}\right) + 2\,C^2\,I^{\frac{1}{2}}(t)$$

Again substituting $\alpha = \frac{1}{2}$ and $n = \frac{1}{2}\,, 1$ we get

$$I^{\frac{1}{2}}(y_1) = -\frac{2C}{\sqrt{\pi}}\left[\frac{\Gamma\left(\frac{3}{2}\right)}{\Gamma(2)}\,t\right] + 2\,C^2\left[\frac{\Gamma(2)}{\Gamma\left(\frac{5}{2}\right)}\,t^{\frac{3}{2}}\right] = -Ct + \frac{8C^2}{3\sqrt{\pi}}\,t^{\frac{3}{2}}$$

Now, for the non-linear form, we get

$$A_1 = \frac{d}{d\lambda} N(y_0 + \lambda y_1) = N'(y_0 + \lambda y_1)\,.\,y_1 \quad at\ \lambda = 0$$

$$= N'(y_0)\,.\,y_1 = 2y_0y_1$$

$$L^{-1}(A_0) = L^{-1}(2y_0y_1) = \int 2C\left[-2C\,\frac{\sqrt{t}}{\sqrt{\pi}} + 2\,C^2t\right] dt = -\frac{8C^2}{3\sqrt{\pi}}\,t^{\frac{3}{2}} + 2C^3t^2\,.$$

So, substituting all these results in the equation (vii), we can get

$$y_2 = -\left[-Ct + \frac{8C^2}{3\sqrt{\pi}}\,t^{\frac{3}{2}}\right] + 2\left[-\frac{8C^2}{3\sqrt{\pi}}\,t^{\frac{3}{2}} + 2C^3t^2\right]$$

$$= Ct - \frac{8C^2}{3\sqrt{\pi}}\,t^{\frac{3}{2}} + 4C^3t^2 \qquad ------(viii)$$

Therefore, the Adomian's decomposition solution is given by

$$y = \sum_{n=0}^{\infty} y_n = y_0 + y_1 + y_2 + \cdots$$

$$= C + \left\{-2C\,\frac{\sqrt{t}}{\sqrt{\pi}} + 2\,C^2t\right\} + \left\{Ct - \frac{8C^2}{3\sqrt{\pi}}\,t^{\frac{3}{2}} + 4C^3t^2\right\} + \cdots$$

$$= C - 2C\,\frac{t^{\frac{1}{2}}}{\sqrt{\pi}} + (2\,C^2 + C)t - \frac{8C^2}{3\sqrt{\pi}}\,t^{\frac{3}{2}} + 4C^3t^2 + \cdots.$$

In a similar way, we can solve the linear non-linear ordinary and partial fractional differential equations and the system of fractional equations by Adomian's decomposition method.

6. Conclusion

In this research study, we have analyzed the ideas of fractional derivatives and their application in fluid dynamics studies. Furthermore, we have also derived the semi-analytical solution of the non-linear differential equations of fractional order using Adomian's decomposition method. The main finding of our study is that the method of Adomian's decomposition is very accurate, simple, and can be applied to solve linear and non-linear ordinary and partial differential equations of fractional order. It is also easier to determine the terms of the fractional differential equation approximation solution. When we consider the negative side of fractional-based models, they are computationally expensive, require enormous data storage requirements, and have a phenomenological description that does not necessarily reflect the physical mechanism behind the scenes.

Furthermore, the study can also use any simulation techniques of mathematical software to easily find the solutions and to represent them graphically, which is our future work.

Acknowledgment

The authors thank South Eastern University of Sri Lanka, for providing an environment and facilities to fulfill the research goal.

7. References

Abiola D, Obembe, Hasan Y. Al-Yousef, & M. Enamul Ho. (2017). Fractional derivatives and their applications in reservoir engineering problems: A review. *Journal of Petroleum Science and Engineering 157,*, 312–327.

Anupama Choudhary, Devendra Kumar, & Jagdev Singh. (2016). A fractional model of fluid flow through porous media with mean capillary pressure. *Journal of the Association of Arab Universities for Basic and Applied Sciences,21,*, 59–63.

Caputo, M. (1967). Linear models of Dissipation whose Q is almost frequency independent–ii. *Geophys J. Int. 13*, 529–539,.

Farnaz, Mubashir Qayyum, Syed Inayat Ali Shah, & Sha. (2021). Homotopic fractional analysis of thin film flow of Oldroyd 6-Constant fluid. *Alexandria Engineering Journal, 60,*, 5311–5322,.

He J.H. (1999). Homotopy Permutation technique.:. *Comput. methods Appl. Mech. Eng. 178(3/4)*, 257-262.

Hossain, M. M. (2008). A New Porous Media Diffusivity Equation with the Inclusion of Rock and Fluid Memories: SPE-114287-MS. *Society of Petroleum Engineers*.

Massoudi, M. (2021). Mathematical Modeling of Fluid Flow and Heat Transfer in Petroleum Industries and Geothermal Applications. *Energies, 14, 5104*.

Myint, T., & Lokenath Debnath . (2007). *Linear Partial Differential Equations for Scientists and Engineers.* Birkhäuser Bosten, 4th edition,.

Odibat., S. M. (2007). Homotopy perturbation method for nonlinear partial differential equations of fractional order. *Phys. Lett. A, 365*, 345–350.

Podlubny., I. (1999). *Fractional Differential Equations.* New York.

Roberto Garra, F. P. (2012). Analytic solutions of fractional differential equations by operational methods. *Applied Mathematics and Computation 218(21)*.

Rogosin S., & Dubatovskaya M. (2018). A Survey on Two Prominent Constructions of Fractional Derivatives,. *Mathematics, 6,* , Dubatovskaya, M.

Umair Ali, R. k.-D. (2012). On Nonlinear Fractional Differential Equations. *International Journal of Modern Mathematical Sciences, 3(3)*, 116-124.

V. Daftardar-Geji and H. Jafari. (2005). Adomian decomposition: a tool for solving a system of fractional differential equations. *J. Math. Anal. Appl., 301*, 508–518.

Z.Z. Ganji, D. G. (2008). Application of the homotopy perturbation method to coupled system of partial differential equations with time fractional derivatives. *Topol. Methods Nonlinear Anal. 31,*, p. 341.

Journal of Science-FAS-SEUSL (2025) 06(02) 11-15
ISSN:2738-2184

Compact Star Model Through Hypergeometric Differential Equation

M.I. Fathima Nusha* and K. Komathiraj

Department of Mathematical Sciences, Faculty of Applied Sciences, South Eastern University of Sri Lanka, Sammanthurai 32200

*nushaismail@seu.ac.lk

Abstract

In this analysis, for a static, spherically symmetric, anisotropic and charged distribution of matter, we present a new class of exact solutions to the Einstein-Maxwell system. This is obtained by assuming specific forms for one of the gravitational potentials, electric field intensity and measure of anisotropy. We modify the condition of pressure isotropy to a second order differential equation which is the master equation of the entire system by introducing new metric functions. This master equation of the Einstein-Maxwell system is reduced to a hypergeometric differential equation with the assistance of a transformation. It is then possible to find exact solutions which can be written explicitly in terms of elementary functions for specific values of model parameters involved. Under certain choices of the model parameters, the new class of solutions is shown to regain some of the previously reported realistic models of compact stars. We illustrate that it is possible to express our class of solutions in a simple closed form so as to examine its physical viability for the studies of relativistic compact stars.

Keywords: Einstein-Maxwell system, compact stars

2. Introduction

This analysis is to construct new physical solutions to the Einstein-Maxwell system which satisfy the physical criteria: the gravitational potentials, electric field intensity, charge distribution and matter distribution should be well-behaved and regular throughout the star. A number of general methods have been proposed to solve the Einstein-Maxwell system for static gravitational fields. Thirukkanesh and Maharaj derived a new class of solution in closed form using a symmetric series analysis. This approach produces a number of difference equation which must be solved explicitly from first principles. Solutions in terms of elementary functions can be retrieved by placing restriction on the parameters. In this analysis we reduce the solutions of the field equations to a hypergeometric equation. Our results show that particular solutions, both with charged and uncharged matter, may be extracted from the hypergeometric equation. Key advantages of our method compared to the series method are highlighted and we depict the restrictions on solutions allowed on physical grounds.

In order to integrate the field equations, several restrictions have been imposed by investigators on the geometry of space time and the matter content. Two key procedures have been adopted to solve these equations for spherically symmetric and static manifolds. At first, the coupled differential equations are solved by computation after choosing an equation of state. As the second point, the exact Einstein-Maxwell solutions can be derived by specifying the geometry and the forms for electric field and anisotropic factor. We adopt the latter technique in an attempt to find solutions in terms of hypergeometric functions that are suitable for the description of relativistic charged stars with anisotropic pressure.

Corresponding Author: nushaismail@seu.ac.lk

3. Methodology

3.1 Field Equations

The space-time is spherically symmetric and static which is consistent with the study of charged compact objects. Thus, there are coordinates (t, r, θ, ϕ) such that the line element is of the form

$$ds^2 = -e^{2(r)}\,dt^2 + e^{2\lambda(r)}\,dr^2 + r^2(d\theta^2 + sin^2\theta d\phi^2) \qquad (1)$$

Where (r) and (r) are arbitrary functions in the radial coordinate r. For an anisotropic perfect fluid, the Einstein-Maxwell field equation can be written in the form

$$\frac{1}{r^2}\,[(1 - e^{-2\lambda})]' = \rho + \frac{1}{2}E^2 \qquad (2a)$$

$$\frac{-1}{r^2}(1 - e^{-2\lambda}) + \frac{2\,\nu'}{r}e^{-2\lambda} = p_r - \frac{1}{2}\,E^2 \qquad (2b)$$

$$e^{-2\lambda}\,(\nu'' + \nu'^2 + \frac{\nu\prime}{r} - \nu'\lambda' - \frac{\lambda'}{r}) = p_t + \frac{1}{2}E^2 \qquad (2c)$$

$$\sigma = \frac{1}{r^2}e^{-}(r^2E\,)' \qquad (2d)$$

- For line element (1) where ρ, p_r, p_t, E and σ are energy density, radial pressure, tangential pressure, the electric field and proper charge density and primes denote the differentiation with respect to the variable *r*.

- A different but equivalent form of the Einstein-Maxwell field equations is obtained if we introduce the transformation:

  $$A^2y^2(x) = e^{2\nu(r)},\ Z(x) = e^{-2\lambda(r)},\ x = Cr^2 \qquad (3)$$

  where *A* and *C* are constants

Under the transformation (3), the system (2) becomes

$$\frac{1-Z}{x} - 2\dot{Z} = \frac{\rho}{c} + \frac{E^2}{2c} \qquad (4b)$$

$$4Z\,\frac{\dot{y}}{y} + \frac{Z-1}{x} = \frac{p_r}{c} - \frac{E^2}{2c} \qquad (4b)$$

$$4Zx^2\ddot{y} + 2\dot{Z}x^2\dot{y} + (\dot{Z}x - Z + 1 - \frac{\Delta x}{c} - \frac{E^2x}{c})y = 0 \qquad (4c)$$

$$\frac{\sigma^2}{c} = \frac{4Z}{x}\,(x\dot{E} + E)^2 \qquad (4d)$$

The quantity $\Delta = p_t - p_r$ is called the measure of anisotropy.

As derived above, we obtain a nonlinear system consists of four independent equations in the seven unknowns ρ, p_t, p_r, E, y, Z and σ. Thus we have the freedom to choose any three variables.

3.2 Choice of potential

We solve the Einstein-Maxwell system (4) by making explicit choice for Z

$$Z = \frac{1+kx}{1+x} \tag{5}$$

Where k is a real constant. In (5) we take k≠1 to avoid negative energy density. On substituting (5) into (4c) we obtain

$$4(1+kx)(1+x)\ddot{y} + 2(k-1)\dot{y} + \left(1-k-\frac{E^2(1+x)^2}{cx}-\frac{\Delta(1+x)^2}{cx}\right) y = 0 \tag{6}$$

It is convenient to introduce a new independent variable X and relevant transformation is given by

$$1+x = KX,\ K = \frac{k-1}{k} \text{ and } Y(x) = y(x)$$

Then equation (6) can be written as

$$X(1-X)\frac{d^2Y}{dX^2} - \frac{1}{2}\frac{dY}{dX} + \left(\frac{K}{4} + \frac{K^2(1-K)E^2X^2}{c(KX-1)} + \frac{K^2(1-K)\Delta X^2}{c(KX-1)}\right)Y=0 \tag{7}$$

We observe that (7) is simplified if we make the choice

$$E^2 = \frac{\propto}{4}\frac{c(KX-1)}{K^2(1-K)X^2} \quad \text{and} \quad \Delta = \frac{\beta}{4}\frac{c(KX-1)}{K^2(1-K)X^2}$$

Where α and β are constants.

The electric field intensity E and Δ vanishes at the center of the star, and remains continuous and bounded in the interior of the star for a wide range of values of the parameter K. Thus this choices of E and Δ are physically reasonable.

On substituting the above choices in (7), we obtain

$$X(1-X)\frac{d^2Y}{dX^2} - \frac{1}{2}\frac{dY}{dX} + \left(\frac{K}{4} + \frac{\propto}{4} + \frac{\beta}{4}\right)Y=0 \tag{8}$$

Note that (8) is a special case of the hypergeometric differential equation.

3.3 Known Cases

A variety of new solutions, in terms of elementary and special functions, can be obtained from (8) for particular values of α, β and K.

- As a first example we take $\alpha=0$, $\beta=0$ and K= -1 (k=½)

Then (8) admits the two linearly independent hypergeometric functions

$$Y_1 = F(-½,-½: -½:X) \quad Y_2 = X^{3/2} F(1,1:5/2:X)$$

It is possible to express these solutions in terms of elementary functions and we get

$y_1(x) = (2 + x)^{1/2}$ and $y_2(x) = (2 + x)^{1/2}\ln[(1 + x)^{1/2}+ (2 + x)^{1/2}]^2$-2 $(1 + x)^{1/2}$

Then the general solution is

$y(x) = C_1 (2 + x)^{1/2} + C_2 [(2 + x)^{1/2} \ln[(1 + x)^{1/2}+ (2 + x)^{1/2}]^2$-2 $(1 + x)^{1/2}]$

This solution was found previously by John Maharaj (2011).

- As a second example we take α=0, β=0 and K=3 (k=-½)

In this case the two linearly independent hypergeometric functions are

Y_1 =F (½, -3/2 : -½ :X) and $Y_2 = X^{3/2}$ F(2,0:5/2:X)

These quantities are equivalent to the elementary functions

$y_1(x) = (2 - x)^{1/2}$ (2x+5)

$y_2(x) = (1 + x)^{3/2}$

Then the general solution is

$y(x) = C_1(2 - x)^{1/2}$ (2x+5) $+C_2(1 + x)^{3/2}$

Which correspond to the neutron star model of Durgapal and Bannerji model (1983).

4. Results and Discussion

If we choose the parameter values α=⅓, β=⅔ and K=-2(k=⅓)

Then (8) admits the two linearly independent hypergeometric functions

Y_1 = F (-½,-½: -½:X) $Y_2= X^{-3/2}$ F(1,1:5/2:X)

These quantities are equivalent to the elementary functions

$y_1(x)= (2 + x)^{1/2}$

$y_2(x)= 2(2 + x)^{1/2} \ln [(1 + x)^{1/2}+ (2 + x)^{1/2}]$-2 $(1 + x)^{1/2}$

We can rewrite the general solution as

$Y(x) = (2 + x)^{1/2} (C_1 + 2C_2 \ln [(1 + x)^{1/2}+ (2 + x)^{1/2}])$- $2C_2 (1 + x)^{1/2}$

Then the complete solution to the Einstein-Maxwell system can be expressed as

$$e^{2\lambda} = \frac{3(1+x)}{3+x}$$

$$e^{2\nu} = A^2((2 + x)^{1/2}(C_1 + 2C_2 \ln [(1 + x)^{1/2}+ (2 + x)^{1/2}])\text{-}2C_2 (1 + x)^{1/2})^2$$

$$\frac{E^2}{c} = \frac{x}{36(1+x)^2}$$

$$\frac{\rho}{c} = \frac{(144+47x)}{72(1+x)^2}$$

.

$$\frac{\sigma^2}{c} = \frac{(x+3)^3}{108(1+x)^5}$$

$$\frac{p_r}{c} = -\frac{(47x+48)}{72(1+x)^2} + \frac{4}{3}\frac{(3+x)}{(1+x)} \times \frac{C_1+2C_2H}{2C_1(2+x)+4C_2((2+x)H-\sqrt{(1+x)(2+x)})}$$

$$\frac{p_t}{c} = -\frac{(43x+48)}{72(1+x)^2} + \frac{4}{3}\frac{(3+x)}{(1+x)} \times \frac{C_1+2C_2H}{2C_1(2+x)+4C_2((2+x)H-\sqrt{(1+x)(2+x)})}$$

$$\frac{\Delta}{c} = \frac{x}{18}(1+x)^2$$

Where H = $\ln(\sqrt{1+x}+\sqrt{2+x})$

The gravitational potentials v and λ are well behaved and continuous in the interior of the star. This is also true for the energy density ρ, the pressure p, the electric field intensity E and the charge density σ. These quantities remain finite and non-singular.

Therefore, this new solution to the Einstein-Maxwell systems presented are physically reasonable.

5. Conclusion

The aim of this analysis is to find new exact solutions to the Einstein-Maxwell systems with a barotropic equation of state for static spherically symmetric gravitational fields. Solutions of the field equation were obtained after specifying one of the potentials, electric field and the anisotropic factor. We regained models found previously. Also we have demonstrated an exact model which is physically reasonable.

6. References

1. Komathiraj K and Maharaj S D, Classes of exact Einstein-Maxwell solutions, Gen.Relativ.Gravit.39,2079 (2007).
2. Maharaj S D and Thirukkanesh S, Some new static charged spheres, Nonlinear Analysis: Real World Applications 10, 3396 (2009).
3. Thirukkanesh S and Maharaj S D, Charged anisotropic matter with a linear equation of state, Class.Quantum Grav. 25,235001 (2008).
4. Hansraj S and Maharaj S D, Charged analogue of Finch-Skea stars, Int. J.Mod.Phys. D 15, 1311 (2006).
5. Durgapal M C and Banerji R, New analytical stellar model in general relativity, Phys.Rev.27, 328 (1983).
6. John A H and Maharaj S D, Relativistic stellar models, prammana J. phys, 77,461(2011).

Journal of Science-FAS-SEUSL (2025) 06(02) 16-19
ISSN:2738-2184

Modeling Student Performance Metrics in a University Course using Lagrange's Interpolation: A Preliminary Investigation

A.N. Wazeetha Mazari*, M.A.A.M. Faham and U.L.M. Althaf

Department of Mathematical Sciences, Faculty of Applied Sciences, South Eastern University of Sri Lanka, Sammanthurai 32200

*mazari@seu.ac.lk

Abstract

This study investigates students' academic performance in the university-level course MTM11022: Vector Algebra and Geometry using Lagrange polynomial interpolation. This research was conducted in a controlled academic environment with fixed teaching and syllabus variables; the objective was to model and predict student performance based on historical data from 2015 to 2021. MATLAB software was used for computation and visualization. Data from 2015-2019 were used for interpolation; 2017 was tested for interpolation accuracy, while 2020 and 2021 served as extrapolation cases. Key performance indicators such as Average Marks, Maximum and Minimum Marks, and Pass Rates were evaluated. The results affirm that Lagrange's interpolation offers meaningful insights into students' outcomes when applied within the data range, with moderate limitations in extrapolation. The model showed high accuracy within known data ranges but reduced performance during extrapolation. This study highlights the usefulness of mathematical modeling for educational data analysis and forecasting.

Keywords: Academic Performance, Lagrange's Interpolation Polynomial, MATLAB software, Predictive Modeling, Educational Data Analysis.

1. Introduction

Mathematical modeling in education helps quantify trends in student learning outcomes. Some approaches in this regard can be found in [1] to [5] in the literature. This study investigates academic performance in MTM 11022 and MTM 11222 (Same course under revised curriculum), a Level I, Semester I course, using historical student marks. Factors such as stable curriculum, fixed lecturer, and consistent evaluation methods provide a controlled environment suitable for interpolation-based modeling. The main objective is to explore the effectiveness of Lagrange interpolation in estimating academic indicators such as Average Marks, Maximum Marks, Minimum Marks and Pass Rate and forecasting future performance trends.

2. Methodology

The Lagrange polynomial interpolation method was employed to model academic data. Student marks from the years 2015 to 2019 were used to construct interpolation polynomials. The year 2017 was selected to test interpolation accuracy. Extrapolation was performed for 2020 and 2021 using the same polynomial model. MATLAB software was used to implement the Lagrange interpolation formula and generate academic performance indicators such as Average Marks, Maximum and Minimum Marks, and Pass Rate. Error analysis was performed by comparing predicted values with actual recorded values using absolute percentage error.

Corresponding Author: mazari@seu.ac.lk

2.1 Data Collection

The sorted data, without the index number of candidates to make sure the confidentiality of marks, used for this study was collected from the Department of Mathematical Sciences, Faculty of Applied Sciences, South Eastern University of Sri Lanka, and covers the period from year 2015 to 2021. The data set contains marks obtained by students in the level I semester I course MTM 11022 and MTM 11222 Vector Algebra and Geometry.

2.2 Lagrange's Interpolation Polynomial Method

The Lagrange polynomial was used to construct an interpolation model and it is obvious that this procedure is quite laborious and Lagrange developed a direct way to find the polynomial

$$P_n(x) = f(x_0)\, L_0(x) + f(x_1)\, L_1(x) + \cdots + f(x_n)\, L_n(x)$$
$$= \sum_{i=0}^{n} fi\; Li(x)$$

where the Lagrange coefficient polynomials

$L_i(x); i = 1, 2, \cdots, n$ are defined by

$$L_i(x) = \frac{(x - x_0)(x - x_1)\cdots(x - x_p)\cdots(x - x_n)}{(x_i - x_0)(x_i - x_1)\cdots(x_i - x_p)\cdots(x_i - x_n)};\ \ p \neq i.$$

and obviously:

$$L_i(x_k) = \delta_{ik} = \begin{cases} 1 & \text{if} \quad i = k \\ 0 & \text{if} \quad i \neq k \end{cases}$$

Where δ_{ik} is Kronecker's symbol

3. Results and Discussion

Interpolation (2017):

Table 1: The interpolated values closely approximated actual 2017 results

Metric	Actual Value	Predicted Value	Error (%)
Average Marks	45.70	60.67	32.74
Maximum Marks	95.00	99.00	4.21
Minimum Marks	3.00	17.50	483.33
Pass Rate (%)	77.66	86.43	11.29

The Lagrange's model gave a reasonably accurate estimate for Average Marks, Maximum Marks and Pass Rate but less accurate predictions for minimum marks due to greater variance. The Figure 1 graphically interpret the results. It demonstrates good fits for interpolation.

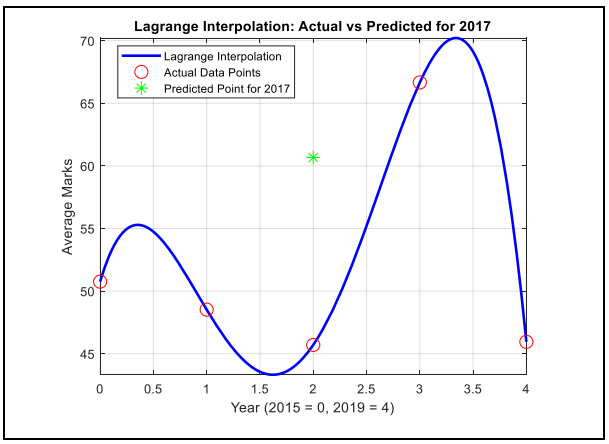

Figure 1: Interpolation curves for each factor.

Extrapolation (2020–2021):

Table 2: Extrapolated predictions showed increasing deviation due to high-order polynomial behaviour

Year	Metric	Actual Value	Predicted Value	Error (%)
2020	Average Marks	54	-171.70	417.9553>100
2020	Maximum Marks	96	-10	110.4167>100
2020	Minimum Marks	8	-126	1675>100
2020	Pass Rate (%)	80	-132.49	265.6155>100
2021	Average Marks	53.22	-831.36	1662.0763>100
2021	Maximum Marks	86	-241	380.2326>100
2021	Minimum Marks	13	-630	4946.1539>100
2021	Pass Rate (%)	92.62	-667.06	820.1912>100

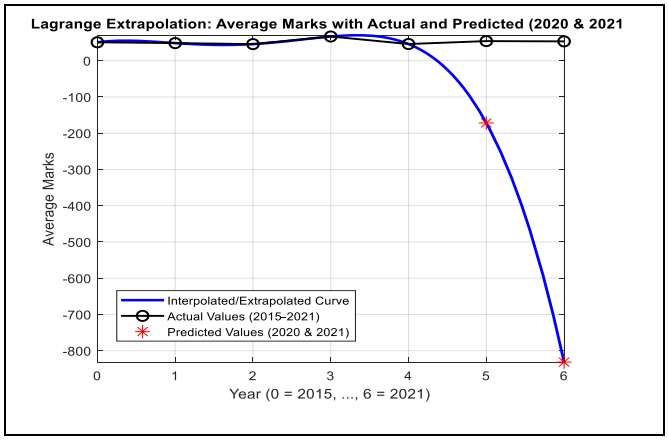

Figure 2: Extrapolation curves for each factor.

Actual vs predicted values (especially for minimum marks and pass rate) diverged significantly, confirming that extrapolation is less reliable.

Extrapolation curves in Figure 2 showed erratic behaviour outside known data boundaries, highlighting polynomial overfitting.

4. Conclusion

Lagrange interpolation is a valid tool for estimating academic performance within a historical dataset. While interpolation results were satisfactory, extrapolation proved less reliable. The study illustrates the potential of using simple mathematical models for academic forecasting, but recommends caution when predicting outside the training data range. Future work could explore spline methods or machine learning models for improved extrapolation accuracy.

5. References

1. Ke Yang (2024). Application of Artificial Neural Networks in Predicting Student Academic Performance.
2. Edric Beaulac & Jeffrey S. Rosenthal (2019). Predicting University Students' Academic Success.
3. Zafar Iqbal et al. (2017). Machine Learning Based Student Grade Prediction.
4. Chuang Liu et al. (2022). A Method for Predicting the Academic Performances Based on Education System Data.
5. Rolly T. Dagdagui (2022). Predicting Students' Academic Performance Using Regression.

Journal of Science-FAS-SEUSL (2025) 06(02) 20-34
ISSN:2738-2184

An Efficient Numerical Quadrature Scheme Based on Three-Point Chebyshev Nodes: An Analogy to Simpson's $\frac{1}{3}$ Rule

U.L.M. Althaf * and M.A.A.M. Faham

Department of Mathematical Sciences, Faculty of Applied Sciences, South Eastern University of Sri Lanka, Sammanthurai 32200

*mohammedalf@gmail.com

Abstract

This paper presents an efficient numerical quadrature rule derived using three-point Chebyshev nodes**,** offering an analogy to Simpson's $1/3$ rule. The proposed scheme combines computational simplicity with enhanced accuracy through the use of non-equidistant nodes, which effectively minimize the Runge phenomenon commonly encountered in polynomial interpolation with equally spaced nodes. The resulting integration formula achieves a convergence order of $O(h^4)$, comparable to Simpson's $1/3$ rule, but with better error control. This approach significantly improves both the stability and accuracy of numerical integration. The method is validated against exact analytical results and benchmarked with classical quadrature rules such as the trapezoidal rule**,** Simpson's $1/3$ rule, and Simpson's $3/8$ rule**.** A composite formulation is implemented to extend the method over larger intervals. Numerical experiments demonstrate that the proposed Chebyshev-based scheme achieves superior accuracy and efficiency even with a relatively low-order formulation, emphasizing its potential for a wide range of scientific and engineering applications.

Keywords: *Chebyshev nodes; numerical quadrature; trapezoidal rule; Simpson's rule; Runge phenomenon.*

1. Introduction

In many real-world problems, evaluating a definite integral is an essential step in understanding physical, biological, or economic systems. Examples include finding the area under a curve, calculating the total quantity from a varying rate (such as velocity or current), or determining probabilities in continuous distributions. However, most integrals cannot be solved exactly, especially when the function is complicated, discontinuous, or known only at specific points. In such cases, numerical integration becomes a practical and necessary approach.

Numerical integration, also known as quadrature, is the process of estimating the value of a definite integral using numerical techniques. Over time, many methods have been developed from simple one like the trapezoidal rule to more advanced approaches such as Gaussian quadrature and adaptive integration. However, these methods involve a trade-off between accuracy, simplicity, and computational cost.

Among these, methods based on orthogonal polynomials, especially Chebyshev polynomials have attracted significant attention. Chebyshev polynomials possess unique mathematical properties that make them highly effective for approximation. Their roots (called Chebyshev nodes) minimize interpolation errors and reduce the large oscillations that often occur with equally spaced points, a problem commonly referred to as the Runge phenomenon.

Corresponding Author: mohammedalf@gmail.com

In this study, we focus on developing a three-point Chebyshev nodes-based quadrature rule that provides an analogy to Simpson's **1/3** rule. Although much of the literature discusses higher-order or generalized Chebyshev quadrature methods, our aim is to show that even a low-order formulation can produce accurate and efficient results. The three-point formulation is analogous to Simpson's 1/3 rule and computationally efficient, making it ideal for making it ideal for practical computations and applications with limited computational resources.

Through theoretical derivation and numerical testing, we demonstrate that the proposed three-point Chebyshev nodes integration scheme provides a well-balanced combination of accuracy and efficiency. Finally, its performance is evaluated against classical quadrature methods and illustrated using a variety of test functions.

2. Literature Review

Numerical quadrature schemes have been extensively developed to approximate definite integrals when analytic evaluation is impractical. Classical Newton–Cotes formulas, including the trapezoidal rule, Simpson's 1/3 rule, and Simpson's 3/8 rule, rely on polynomial interpolation at uniformly spaced nodes. Although widely used due to their simplicity, these methods generally suffer from limited accuracy when the integrand exhibits rapid variation, endpoint singularities, or oscillatory behavior.

This challenge has driven the development of alternative quadrature schemes, including those based on Chebyshev nodes, which offer distinct advantages in certain scenarios (Gilboa & Peled, 2017). Chebyshev polynomials offer several advantages for numerical approximation due to their minimax property and optimal distribution of nodes, which significantly reduce interpolation error (Mason, 1993).

Several studies have explored Chebyshev or some other quadrature schemes to enhance error performance. Esclahchi et al. (2005) developed Chebyshev–Newton–Cotes rules, demonstrating notable improvements over traditional formulas. Kythe & Schäferkotter (2004) provide practical methods for various quadrature rules, including those based on Chebyshev polynomials. They discuss the balance between computational cost and accuracy, which is a central theme of the proposed work. Burg and Degny (2013) proposed a derivative-based midpoint quadrature rule with enhanced local precision. Peer (2015) introduced geometric insights into tangent-based approximations that indirectly contribute to improved integral estimation. Ullah (2015) proposed a generalized rule with better numerical efficiency in selected computational scenarios. Collectively, these studies indicate a consistent research trend toward formulating quadrature rules that achieve a higher balance between accuracy and computational simplicity.

However, many existing Chebyshev-based approaches either rely on higher-order constructions with increased computational cost or lack direct analogies to standard Newton–Cotes rules commonly used in practice. To bridge this gap, the present work proposes a three-point Chebyshev quadrature rule that is structurally analogous to Simpson's 1/3 rule but leverages non-equidistant Chebyshev nodes. This formulation aims to maintain the simplicity and familiarity of Simpson's method while achieving superior accuracy, stability, and convergence properties.

3. Theoretical Background and Notations

3.1 Numerical Integration and Quadrature Rules

Numerical integration, also known as numerical quadrature, involves approximating the integral of a function $f(x)$ over an interval $[a, b]$ using discrete evaluations of the function at selected points.

3.2 Some Classical Newton-Cotes Quadrature Rules

3.2.1 *Trapezoidal Rule*

The Trapezoidal rule is the simplest Newton-Cotes quadrature formula, which approximates the integrand by a linear polynomial passing through two equally spaced points. For a single interval $[a, b]$, the rule is given by:

$$\int_a^b f(x)dx \approx \frac{h}{2}[f(a) + f(b)],$$

where $h = b - a$ is the width of the single interval. This rule corresponds to the area under the straight line connecting $f(a)$ and $f(b)$, forming a trapezoid.

3.2.2 *Simpson's* $1/3$ *Rule*

The Simpson's $1/3$ rule approximates the integrand by fitting a second-degree polynomial (a parabola) through three equally spaced nodes. For a given interval $[a, b]$, the rule can be written as:

$$\int_a^b f(x)dx \approx \frac{h}{3}\left[f(a) + 4f\left(\frac{a+b}{2}\right) + f(b)\right],$$

where $h = \frac{b-a}{2}$.

This rule provides exact results for polynomials of degree three or less and is known for its higher accuracy compared to the trapezoidal rule.

3.2.3 *Simpson's* $3/8$ *Rule*

The Simpson's $3/8$ Rule uses a cubic polynomial to approximate the integrand over four equally spaced points. For a single application over the interval $[a, b]$, it is given by:

$$\int_a^b f(x)dx \approx \frac{3h}{8}[f(a) + 3f(a+h) + 3f(a+2h) + f(b)],$$

where $h = \frac{b-a}{3}$. The rule provides higher accuracy than Simpson's $1/3$ rule for certain smooth functions due to its use of a higher-degree interpolating polynomial.

3.3 Composite Rules

To improve the accuracy of numerical integration over a finite interval, composite quadrature rules are employed by subdividing the integration domain into smaller subintervals and applying the respective rule repeatedly.

Let the interval of integration $[a, b]$ be divided into n equal subintervals by defining a set of points $x_0, x_1, \dots, x_n$, where

$$x_i = a + ih, \quad i = 0, 1, \cdots n, \quad \text{and} \quad h = \frac{b-a}{n}$$

is the uniform step size.

3.3.1 *Composite Trapezoidal Rule*

In the composite trapezoidal rule, the function is evaluated at the endpoints of each subinterval to approximate the integral as sum of the Trapezoidal areas. For $n(\geq 1)$ subintervals, the composite trapezoidal rule is given by:

$$\int_a^b f(x)\,dx \approx \frac{h}{2}\left[f(x_0) + 2\sum_{i=1}^{n-1} f(x_i) + f(x_n)\right].$$

3.3.2 *Composite Simpson's 1/3 Rule*

This method applies Simpson's 1/3 rule over successive pairs of subintervals. Thus, n must be even. For n subintervals, the composite Simpson's 1/3 rule is:

$$\int_a^b f(x)\,dx \approx \frac{h}{3}\left[f(x_0) + 4\sum_{i=1}^{n/2} f(x_{2i-1}) + 2\sum_{i=1}^{(n-2)/2} f(x_{2i}) + f(x_n)\right].$$

3.3.3 *Composite Simpson's 3/8 Rule*

Simpson's 3/8 rule uses a cubic polynomial over three consecutive subintervals. Thus, n must be a multiple of 3. For n subintervals, the composite Simpson's 3/8 rule is:

$$\int_a^b \boldsymbol{f(x)\,dx} \approx \frac{\boldsymbol{3h}}{\boldsymbol{8}}\left[\boldsymbol{f(x_0) + 3\sum_{i=1}^{n/3}\left(f(x_{3i-2}) + f(x_{3i-1})\right) + 2\sum_{i=1}^{(n-3)/3} f(x_{3i}) + f(x_n)}\right].$$

3.4 Chebyshev Polynomials

3.4.1 *Chebyshev Polynomials of First Kind*

The Chebyshev polynomials of the first kind of degree n, denoted by $T_n(x)$, are defined on the interval $[-1, 1]$ as follows (Mason, J.C., 1993):

$$T_n(x) = \cos(n\theta),$$

where $\theta = \cos^{-1} x$, with $0 \leq \theta \leq \pi$ and $n = 0, 1, 2, \cdots$.

3.4.2 *Recurrence Relation of $T_n(x)$*

A three-term recurrence relation between consecutive Chebyshev polynomials of first kind in standard form is

$$T_0(x) = 1,$$

$$T_{n+1}(x) = 2x\,T_n(x) - T_{n-1}(x), \text{ for } n \geq 1.$$

3.4.3 *Nodes of $T_n(x)$*

The Chebyshev polynomial $T_n(x)$, for $n \geq 1$ has n simple, real nodes in the interval $(-1, 1)$ and they are given by

$$x_j = \cos\left(\frac{2j+1}{2n}\pi\right), \qquad j = 0,1, \ldots, n-1.$$

3.4.4 *Chebyshev Polynomials on* $[a, b]$ *and Shifted Chebyshev Polynomials*

The standard domain of the Chebyshev polynomials is $[-1, 1]$. However, it is possible to define Chebyshev polynomials over any generic interval $[a, b]$ using the technique of change of variable:

$$\bar{x} = \frac{x - \frac{1}{2}(a+b)}{\frac{1}{2}(b-a)}.$$

Thus, Chebyshev nodes $\bar{x}_j$ of the Chebyshev polynomial of the first kind of degree n on $[a, b]$ will be given by

$$\bar{x}_j = \frac{1}{2}\left[(b-a)\cos\left(\frac{2j+1}{2n}\pi\right) + a + b\right],\ j = 0,1,\dots,n-1.$$

The Chebyshev polynomials of the first kind on the interval $[0, 1]$ called Shifted Chebyshev polynomials, denoted by $T_n^*(x)$ and are defined as

$$T_n^*(x) = T_n(2x-1).$$

3.4.5 *Nodes of Third-Degree Chebyshev Polynomial and Their Properties*

The nodes of the third-degree Chebyshev polynomial $T_3(x)$ mapped onto the interval $[a, b]$ are given by:

$$z_k = \frac{1}{2}(a+b) - \frac{1}{2}(b-a)\cos\left(\frac{(2k+1)\pi}{6}\right), \quad k = 0, 1, 2.$$

Evaluating the cosine terms results in the following explicit expressions:

$$z_0 = \frac{1}{2}(a+b) - \frac{\sqrt{3}}{4}(b-a), \quad z_1 = \frac{1}{2}(a+b) \text{ and } z_2 = \frac{1}{2}(a+b) + \frac{\sqrt{3}}{4}(b-a).$$

It is worth to note that the mid-point of any interval is one of the nodes of third degree Chebyshev Polynomial in the respective interval.

3.4.5.1 *Spacing between Nodes of Third-Degree Chebyshev Polynomial*

Let $l = b - a$ denote the interval length. The distance between adjacent Chebyshev nodes is:

$$z_1 - z_0 = z_2 - z_1 = \frac{\sqrt{3}}{4}(b-a) = \mu l, \qquad \text{where } \mu = \frac{\sqrt{3}}{4}. \tag{1}$$

3.4.5.2 *Spacing from Endpoints*

The distance from the endpoints of the interval to the nearest Chebyshev nodes is:

$$z_0 - a = b - z_2 = \frac{(2-\sqrt{3})}{4}(b-a) = \lambda l, \qquad \text{where } \lambda = \frac{(2-\sqrt{3})}{4}. \tag{2}$$

From the above relationships, we observe that the nodes of the third-degree Chebyshev polynomials are symmetrically spaced about the midpoint of the interval, and the spacing depends solely on the interval length l.

4. Development of the Proposed Method

4.1 Objective

The primary objective of this study is to develop an efficient quadrature rule for approximating definite integrals of the form:

$$\int_a^b f(x)dx. \tag{3}$$

by constructing a quadratic polynomial interpolant based on the nodes of the third-degree Chebyshev polynomial.

4.2 Quadratic Interpolation using Three-Point Chebyshev Nodes

Let $P(x) = px^2 + qx + r$ be the quadratic polynomial interpolant to $f(x)$ at the nodes z_0, z_1, and z_2 of third-degree Chebyshev polynomial over the interval $[a, b]$. Then:

$$f(x) \approx P(x) = px^2 + qx + r; \quad x \in [a, b]. \tag{4}$$

Using the relationship between endpoints of the integral domain and the three-point Chebyshev nodes in the interval (see equation (2)), the definite integral of $f(x)$ over the interval $[a, b]$ can be approximated as:

$$\int_a^b f(x)\,dx \approx \int_a^b P(x)\,dx = \int_{z_0-\lambda l}^{z_2+\lambda l} (px^2 + qx + r)\,dx, \tag{5}$$

which evaluates to:

$$\int_a^b f(x)\,dx \approx \frac{p}{3}[(z_2 + \lambda l)^3 - (z_0 - \lambda l)^3] + \frac{q}{2}[(z_2 + \lambda l)^2 - (z_0 - \lambda l)^2] + r[(z_2 + \lambda l) - (z_0 - \lambda l)]. \tag{6}$$

By simplifying and regrouping the terms, the equation (6) can be expressed as:

$$\int_a^b f(x)\,dx \approx \frac{l}{6}\left[(pz_0{}^2 + qz_0 + q) + 4(pz_1{}^2 + qz_1 + r) + (pz_2{}^2 + qz_2 + r) + \frac{1}{8}pl^2\right]. \tag{7}$$

The interpolated function values at the Chebyshev nodes are:

$$\begin{aligned} f(z_0) &= pz_0{}^2 + qz_0 + r, \\ f(z_1) &= pz_1{}^2 + qz_1 + r, \\ f(z_2) &= pz_2{}^2 + qz_2 + r. \end{aligned} \tag{8}$$

Solving the system allows the coefficient p to be expressed in terms of function values at the nodes:

$$p = \frac{8}{3l^2}[f(z_0) - 2f(z_1) + f(z_2)]. \tag{9}$$

Substituting equations (8) and (9) into equation (7) gives the integral approximation entirely in terms of function values at the Chebyshev nodes:

$$\int_a^b f(x)\,dx \approx \frac{l}{9}[2f(z_0) + 5f(z_1) + 2f(z_2)]. \tag{10}$$

Expressing the Chebyshev nodes in terms of the interval endpoints using the parameter λ (equation (2)) formula (10) becomes:

$$\int_a^b f(x)\,dx \approx \frac{l}{9}\left[2f(a + \lambda l) + 5f\left(\frac{a+b}{2}\right) + 2f(b - \lambda l)\right], \tag{11}$$

where $l = b - a$ and $\lambda = \frac{(2-\sqrt{3})}{4}$.

To construct a quadrature method analogous to Simpson's 1/3 rule, we divide the integration interval into two equal subintervals, placing one Chebyshev node at the midpoint and the other two within each subinterval. Replacing l by $2h$ in equation (11), we obtain the three-point Chebyshev quadrature rule:

$$\int_a^b f(x)\,dx \approx \frac{2h}{9}[2f(z_0) + 5f(z_1) + 2f(z_2)], \tag{12}$$

or in terms of the endpoints of the integration interval

$$\int_a^b f(x)\,dx \approx \frac{2h}{9}\left[2f(a + 2\lambda h) + 5f\left(\frac{a+b}{2}\right) + 2f(b - 2\lambda h)\right], \tag{13}$$

where $h = \frac{b-a}{2}$ and $\lambda = \frac{(2-\sqrt{3})}{4}$.

4.3 The Composite Three-Point Chebyshev Quadrature Rule

The proposed method utilizes three Chebyshev nodes to approximate the integrand by fitting a quadratic polynomial over successive pairs of subintervals. Since the method spans two subintervals per application, the total number of subintervals n must be even.

Let the interval of integration $[a, b]$ be partitioned into n equal subintervals by introducing the grid points $x_0,\ x_1, \dots, x_n$, where

$$x_i = a + ih, \quad i = 0, 1, \cdots, n,$$

and

$$h = \frac{b-a}{n}$$

is the uniform step size.

Then, using equation (13), the composite quadrature formula for the proposed method over n equally subintervals in the interval $[a, b]$is given by:

$$\int_a^b f(x)\,dx \approx \frac{2h}{9}\left[2\sum_{i=0}^{(n-2)/2} f(x_{2i} + 2\lambda h) + 5\sum_{i=1}^{n/2} f(x_{2i-1}) + 2\sum_{i=1}^{n/2} f(x_{2i} - 2\lambda h)\right], \tag{14}$$

where $\lambda = \frac{(2-\sqrt{3})}{4}$.

4.4 Error Bound for Three-Point Chebyshev Quadrature Rule

Let integration interval $[a, b]$ be divided into n equal subintervals, with n even. Define the set of points $x_0, x_1, \dots, x_n$ as

$$x_i = a + ih, \qquad i = 0, 1, \cdots n, \qquad h = \frac{b-a}{n},$$

where h is the uniform step size.

Using the three-point Chebyshev quadrature rule (equation (12)), the approximate area $\tilde{A}$ under the parabola over the interval $[x_0, x_2]$ (the first two subintervals) is

$$\tilde{A} = \frac{2h}{9}[2f(z_0) + 5f(z_1) + 2f(z_2)], \tag{15}$$

where $h = \frac{x_2 - x_0}{2}$, and z_0, z_1, z_2 are nodes of the corresponding third-degree Chebyshev polynomial on $[x_0, x_2]$.

Consider the Taylor series expansion of $f(x)$ about $x = z_1$:

$$f(x) = f(z_1) + (x - z_1)f'(z_1) + \frac{1}{2!}(x - z_1)^2 f''(z_1) + \frac{1}{3!}(x - z_1)^3 f'''(z_1) + \cdots. \tag{16}$$

From equations (1) and (2), the Chebyshev nodes are

$$z_1 = x_1 = \frac{x_0 + x_2}{2},\ z_0 = x_0 + \lambda l = z_1 - 2\mu h,\ \ z_2 = x_2 - \lambda l = z_1 + 2\mu h,$$

where $\lambda = \frac{2 - \sqrt{3}}{4}$ and $\mu = \frac{\sqrt{3}}{4}$.

Substituting $x = z_0 = z_1 - 2\mu h$ and $x = z_2 = z_1 + 2\mu h$ into (16) we obtain

$$f(z_0) = f(z_1) - 2\mu h f'(z_1) + \frac{4}{2!}(\mu h)^2 f''(z_1) - \frac{8}{3!}(\mu h)^3 f'''(z_1) + \cdots, \tag{17}$$

and

$$f(z_2) = f(z_1) + 2\mu h f'(z_1) + \frac{4}{2!}(\mu h)^2 f''(z_1) + \frac{8}{3!}(\mu h)^3 f'''(z_1) + \cdots. \tag{18}$$

Substituting (17) and (18) into (15), $\tilde{A}$ can be written as

$$\tilde{A} = \frac{2h}{9}\left[9f(z_1) + 4\left(\frac{4}{2!}(\mu h)^2 f''(z_1) + \frac{16}{4!}(\mu h)^4 f^{(4)}(z_1) + \frac{64}{6!}(\mu h)^6 f^{(6)}(z_1) + \cdots\right)\right]. \tag{19}$$

Setting $\mu = \frac{\sqrt{3}}{4}$ and simplifying, we obtain

$$\tilde{A} = 2hf(z_1) + \frac{h^3}{3}f''(z_1) + \frac{h^5}{48}f^{(4)}(z_1) + \frac{h^7}{1920}f^{(6)}(z_1) + \cdots. \tag{20}$$

The exact area A, under $f(x)$ over $[x_0, x_2]$ is

$$A = \int_{x_0 = z_1 - h}^{x_2 = z_1 + h} \left[f(z_1) + (x - z_1)f'(z_1) + \frac{1}{2!}(x - z_1)^2 f''(z_1) + \frac{1}{3!}(x - z_1)^3 f'''(z_1) + \cdots\right] dx. \tag{21}$$

Evaluating the integral gives

$$A = 2hf(z_1) + \frac{h^3}{3}f''(z_1) + \frac{h^5}{60}f^{(4)}(z_1) + \frac{h^7}{2520}f^{(6)}(z_1) + \cdots. \tag{22}$$

Therefore, the error over $[x_0, x_2]$ is

$$\begin{aligned} A - \tilde{A} &= \left(\frac{1}{60} - \frac{1}{48}\right)h^5 f^{(4)}(z_1) + \left(\frac{1}{2520} - \frac{1}{1920}\right)h^5 f^{(6)}(z_1) + \cdots, \\ &\approx -\frac{h^5}{240}f^{(4)}(z_1) = -\frac{h^5}{240}f^{(4)}(x_1). \quad (\because z_1 \equiv x_1) \end{aligned} \tag{23}$$

Applying the same argument to each pair of subintervals, the total error E for the entire interval $[a, b]$ is

$$E = -\frac{h^5}{240}\left[f^{(4)}(x_1) + f^{(4)}(x_3) + \cdots + f^{(4)}(x_{n-1})\right].$$

Let $f^{(4)}(\xi) = \max\left\{f^{(4)}(x_1), f^{(4)}(x_3), \cdots, f^{(4)}(x_{n-1})\right\}$.

Then the maximum error $E_{max} \leq -\frac{nh^5}{480} f^{(4)}(\xi) \qquad \left(\because \text{number of interval is } \frac{n}{2}\right)$

$$= -\frac{nhh^4}{480} f^{(4)}(\xi) = -\frac{(b-a)h^4}{480} f^{(4)}(\xi) \qquad \left(\because h = \frac{b-a}{n}\right)$$

Hence the error in proposed three-point Chebyshev quadrature method is fourth order accurate, i.e., $O(h^4)$, where $h = \frac{b-a}{n}$ is the subinterval width.

5. Results and Discussion

For a fair comparison of the quadrature rules, it is essential to account for both their structural constraints such as the number of nodes (in other words number of subintervals) and their computational effort, typically measured in terms of number of function evaluations.

Accordingly, the performance of each quadrature rule is evaluated using the following two criteria:

(i) The total number of subintervals (n)

This refers to the partitioning of the integration domain into n subintervals. Each quadrature rule has condition on n, as summarized in the table below:

Table 01: Requirements on the Number of Subintervals for Different Quadrature Rules

Rule	Condition on n	Application of the Rule
Trapezoidal	Any integer	Applied over each subinterval
Simpson's 1/3	Must be even	Applied over 2 subintervals
Simpson's 3/8	Must be multiple of 3	Applied over 3 subintervals
Chebyshev	Must be even	Applied over 2 subintervals covering 3 Chebyshev nodes

Thus, for concurrent applicability of all rules, the number of subintervals n must be chosen as a common multiple of the constraints above. The least common multiple (LCM) of 2 and 3 is 6, hence suitable values include $n = 6, 12, 18, \cdots$.

(ii) Number of Panels (k)***:***

Alternatively, the integration domain can be partitioned into k panels, where each panel represents a subdomain over which a single, complete application of the respective

quadrature rule is executed. The number of discretization nodes per panel, as well as the total function evaluations, is summarized as follows:

Table 02: Comparison of Number of Function Evaluations in Different Quadrature Methods.

Rule	Nodes per Panel	Total Function Evaluations
Trapezoidal	2 (endpoints)	$k + 1$
Simpson's 1/3	3 (equally spaced)	$2k + 1$
Simpson's 3/8	4 (equally spaced)	$3k + 1$
Chebyshev	3 (Chebyshev nodes)	$3k$

Numerical Tests

In this section, we present three illustrative examples to evaluate the efficiency of the proposed Chebyshev nodes-based rule (*Cheb*) by comparing it with the trapezoidal rule (*Trap*), Simpson's 1/3 rule (*Simp13*), and Simpson's 3/8 rule (*Simp38*).

Example I: $\int_0^1 \sqrt{1-x^2}\,dx = \frac{\pi}{4} \approx 0.785398163397448.$

Table 03: Approximate Value (AV) and Absolute Approximation Error (AAE) for $\int_0^1 \sqrt{1-\mathrm{x}^2}\,\mathrm{dx}$ Using Various Quadrature Rules with Number of Subintervals $\mathrm{n} = 6, 12, 48, 96$.

	n − Number of Subintervals							
	$n = 6$		$n = 12$		$n = 48$		$n = 96$	
Rule	AV	AAE	AV	AAE	AV	AAE	AV	AAE
Trap	7.6550e-01	1.9902e-02	7.7834e-01	7.0544e-03	7.8451e-01	8.8349e-04	7.8509e-01	3.1246e-04
Simp13	7.7753e-01	7.8666e-03	7.8263e-01	2.7718e-03	7.8505e-01	3.4556e-04	7.8528e-01	1.2212e-04
Simp38	7.7581e-01	9.5920e-03	7.8202e-01	3.3774e-03	7.8498e-01	4.2081e-04	7.8525e-01	1.4870e-04
Cheb	7.8492e-01	4.7625e-04	7.8523e-01	1.6619e-04	7.8538e-01	2.0560e-05	7.8539e-01	7.2562e-06

Table 04: Approximate Value (AV) and Absolute Approximation Error (AAE) for $\int_0^1 \sqrt{1-\mathrm{x}^2}\,\mathrm{dx}$ Using Various Quadrature Rules with Number of Panels $\mathrm{k} = 1, 2, 6, 10$.

	k − Number of Panels (equivalent to number of applications of the rule)							
	$k = 1$		$k = 2$		$k = 6$		$k = 10$	
Rule	AV	AAE	AV	AAE	AV	AAE	AV	AAE
Trap	5.0000e-01	2.8540e-01	6.8301e-01	1.0239e-01	7.6550e-01	1.9902e-02	7.7613e-01	9.2686e-03
Simp13	7.4402e-01	4.1381e-02	7.7090e-01	1.4499e-02	7.8263e-01	2.7718e-03	7.8411e-01	1.2864e-03
Simp38	7.5806e-01	2.7336e-02	7.7581e-01	9.5920e-03	7.8356e-01	1.8358e-03	7.8455e-01	8.5222e-04
Cheb	7.8281e-01	2.5847e-03	7.8451e-01	8.8564e-04	7.8523e-01	1.6619e-04	7.8532e-01	7.6819e-05

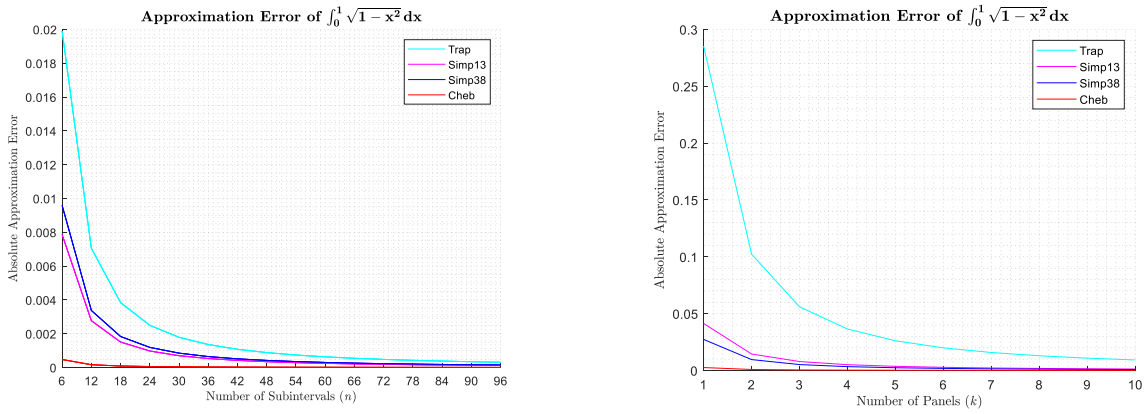

(a) ***(b)***

Figure 01: Graphs of the Absolute Approximation Error for $\int_0^1 \sqrt{1-x^2}\,dx$: (a) Error vs. Number of Subintervals, and (b) Error vs. Number of Panels, for Different Quadrature Rules.

The integrand $\sqrt{1-x^2}$ used in this example is a smooth and well-behaved function over the interval $[0,1]$. As observed in Table 03 and Figure 01(a), all quadrature schemes demonstrate a consistent decrease in error as the number of subintervals n increases. However, the proposed three-point Chebyshev quadrature rule delivers significantly superior performance across every tested discretization. Notably, even at a relatively small grid size of $n = 6$, the proposed method achieves an error nearly an order of magnitude smaller than both Simpson's 1/3 and 3/8 rules.

Furthermore, as illustrated in Table 04 and Figure 01(b), increasing the number of panels (i.e., repeated applications of the rule), Chebyshev rule continues to outperform, achieving errors below 10^{-5}, thereby confirming its high accuracy for smooth functions.

Example II: $\int_{0.1}^{2.5} (3\ln x + 2x^2)\,dx \approx 10.778956016954378.$

Table 05: Approximate Value (AV) and Absolute Approximation Error (AAE) for $\int_{0.1}^{2.5}(3\ln x + 2x^2)\,dx$ Using Various Quadrature Rules with Number of Subintervals $n = 6, 12, 48, 96$.

	n − Number of Subintervals							
	$\boldsymbol{n=6}$		$\boldsymbol{n=12}$		$\boldsymbol{n=48}$		$\boldsymbol{n=96}$	
Rule	AV	AAE	AV	AAE	Value	AV	AV	AAE
Trap	1.0596e+01	1.8303e-01	1.0723e+01	5.6057e-02	1.0775e+01	3.9511e-03	1.0778e+01	9.9680e-04
Simp13	1.0700e+01	7.9412e-02	1.0765e+01	1.3734e-02	1.0779e+01	1.6198e-04	1.0779e+01	1.2032e-05
Simp38	1.0668e+01	1.1068e-01	1.0758e+01	2.0933e-02	1.0779e+01	3.1307e-04	1.0779e+01	2.5421e-05
Cheb	1.0760e+01	1.8941e-02	1.0775e+01	4.0754e-03	1.0779e+01	5.8447e-05	1.0779e+01	4.4585e-06

Table 06: Approximate Value (AV) and Absolute Approximation Error (AAE) for $\int_{0.1}^{2.5}(3\ln x + 2x^2)\,dx$ Using Various Quadrature Rules with Number of Panels $k = 1, 2, 6, 10$.

	k − Number of Panels (equivalent to number of applications of the rule)							
	$\boldsymbol{k=1}$		$\boldsymbol{k=2}$		$\boldsymbol{k=6}$		$\boldsymbol{k=10}$	
Rule	AV	AAE	AV	AAE	AV	AAE	AV	AAE
Trap	1.0033e+01	7.4562e-01	1.0017e+01	7.6177e-01	1.0596e+01	1.8303e-01	1.0701e+01	7.7579e-02
Simp13	1.0012e+01	7.6716e-01	1.0583e+01	1.9547e-01	1.0765e+01	1.3734e-02	1.0776e+01	3.0902e-03
Simp38	1.0317e+01	4.6240e-01	1.0668e+01	1.1068e-01	1.0772e+01	6.9403e-03	1.0777e+01	1.4892e-03
Cheb	1.0675e+01	1.0437e-01	1.0740e+01	3.9124e-02	1.0775e+01	4.0754e-03	1.0778e+01	1.0167e-03

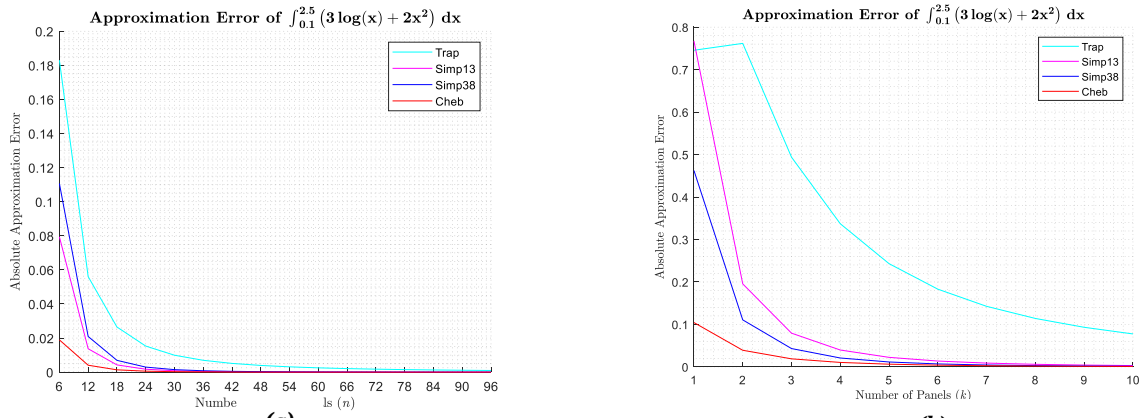

Figure 02: *Graphs of the Absolute Approximation Error for* $\int_{0.1}^{2.5}(3\ln x + 2x^2)\,dx$*: (a) Error vs. Number of Subintervals, and b) Error vs. Number of Panels, for Different Quadrature Rules.*

The integrand in this test problem, $3\ln(x) + 2x^2$ involves a logarithmic term that becomes steep near the lower limit $x = 0.1$, making the function less smooth than the one considered in Example I. As shown in Table 05, Table 06, and Figure 02(a–b), all quadrature methods initially produce relatively larger errors; however, the accuracy improves steadily as the number of subintervals increases. Among the methods considered, the proposed Chebyshev quadrature achieves the most rapid and consistent reduction in error, confirming that the proposed scheme remains robust even when the integrand exhibits mild singularity-like behavior near the boundary of the domain.

Example III: $\int_0^{\pi} e^{\cos x}\sin 4x\,dx = \frac{120}{e} - 16e \approx 0.6530236852283537.$

Table 07: Approximate Value (AV) and Absolute Approximation Error (AAE) for $\int_0^{\pi} e^{\cos x}\sin 4x\,dx$ Using Various Quadrature Rules with Number of Subintervals $n = 6, 12, 48, 96$.

	n − Number of Subintervals							
	$\boldsymbol{n = 6}$		$\boldsymbol{n = 12}$		$\boldsymbol{n = 48}$		$\boldsymbol{n = 96}$	
Rule	AV	AAE	AV	AAE	AV	AAE	AV	AAE
Trap	4.1474e-01	2.3828e-01	5.9805e-01	5.4972e-02	6.4966e-01	3.3609e-03	6.5218e-01	8.3933e-04
Simp13	8.6804e-01	2.1502e-01	6.5916e-01	6.1314e-03	6.5304e-01	1.9352e-05	6.5302e-01	1.1981e-06
Simp38	4.6658e-01	1.8644e-01	6.7281e-01	1.9784e-02	6.5307e-01	4.4102e-05	6.5303e-01	2.7043e-06
Cheb	7.4240e-01	8.9380e-02	6.5540e-01	2.3729e-03	6.5303e-01	7.2706e-06	6.5302e-01	4.4951e-07

Table 08: Approximate Value (AV) and Absolute Approximation Error (AAE) for $\int_0^{\pi} e^{\cos x}\sin 4x\,dx$ Using Various Quadrature Rules with Number of Panels $k = 1, 2, 6, 10$.

	k − Number of Panels (equivalent to number of applications of the rule)							
	$\boldsymbol{k = 1}$		$\boldsymbol{k = 2}$		$\boldsymbol{k = 6}$		$\boldsymbol{k = 10}$	
Rule	AV	AAE	AV	AAE	AV	AAE	AV	AAE
Trap	0	6.5302e-01	0	6.5302e-01	4.1474e-01	2.3828e-01	5.7301e-01	8.0018e-02
Simp13	0	6.5302e-01	0	6.5302e-01	6.5916e-01	6.1314e-03	6.5371e-01	6.8324e-04
Simp38	1.0633e+00	1.7163e+00	4.6658e-01	1.8644e-01	6.5568e-01	2.6598e-03	6.5332e-01	3.0118e-04
Cheb	1.1887e+00	5.3565e-01	3.0277e-01	3.5025e-01	6.5540e-01	2.3729e-03	6.5328e-01	2.5903e-04

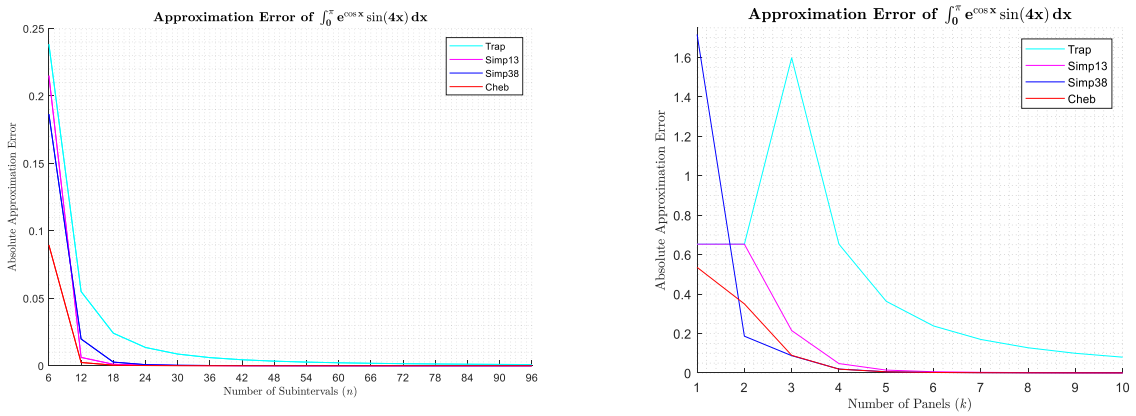

(a) ***(b)***

Figure 03: *Graphs of the Absolute Approximation Error for* $\int_0^\pi e^{\cos x}\sin 4x\,dx$*: (a) Error vs. Number of Subintervals, and (b) Error vs. Number of Panels, for Different Quadrature Rules.*

The function in Example III, $e^{\cos x}\sin 4x$, is highly oscillatory over the interval $[0,\pi]$. The results in Table 07, Table 08, and Figure 03(a–b) show that for a very small number of subintervals or panels, all quadrature rules produce noticeable errors. Interestingly, for $k=1$, Simpson's 1/3 rule outperforms even Simpson's 3/8 rule, and for $k=2$, Simpson's 3/8 rule performs better than the proposed Chebyshev-based rule. This behavior can be attributed to the rapid oscillations of the integrand, which reduces the effectiveness due to the inadequacy of low-resolution polynomial interpolation in representing oscillatory functions. However, as the number of panels increases, the Chebyshev quadrature stabilizes more quickly and achieves significantly smaller errors than both the trapezoidal and Simpson's rules. This demonstrates the advantage of using Chebyshev nodes, which more effectively capture oscillatory variations in the function and improve numerical stability.

6. Conclusion

In this study, we presented an efficient three-point Chebyshev nodes-based quadrature rule constructed as an analogy to Simpson's 1/3 rule. By employing non-equidistant Chebyshev nodes, the proposed method effectively captures the behavior of the integrand and achieves higher accuracy compared to classical Newton–Cotes rules, without a significant increase in computational cost. Numerical experiments involving three different types of integrands smooth, weakly singular and highly oscillatory, clearly demonstrate the accuracy, stability, and robustness of the proposed scheme. In all cases, the proposed Chebyshev quadrature rule demonstrated faster convergence and consistently smaller approximation errors compared to the trapezoidal rule, Simpson's 1/3 rule, and Simpson's 3/8 rule. Moreover, the accuracy improved progressively as the number of subintervals increased. These findings confirm that even a low-order Chebyshev formulation can achieve an excellent balance between computational simplicity and numerical precision, making it well-suited for a wide range of scientific and engineering applications. Future work may focus on examining its performance for strongly singular integrands and other challenging scenarios, as well as extending the approach to higher-order Chebyshev-based quadrature rules.

7. References

1. Gilboa, S., & Peled, R. (2017). Chebyshev-type Quadratures for Doubling Weights. Constructive Approximation, 45(2), 193–216. https://doi.org/10.1007/s00365-016-9360-4.
2. Mason, J. C. (1993). Chebyshev polynomials of the second, third and fourth kinds in approximation, indefinite integration, and integral transforms. Journal of Computational and Applied Mathematics, 49 (1-3), 169-178. https://doi.org/10.1016/0377-0427(93)90148-5
3. M. R. Esclahchi, M. Dehghan and M. Masjed-Jamei, "The First Kind Chebyshev-Newton-Cotes Quadrature Rules (Closed Type) and Its Numerical Improvement," Applied Mathematics and Computation, Vol. 168, No. 1, 2005, pp. 479-495. doi:10.1016/j.amc.2004.09.048
4. Kythe, P. K., & Schäferkotter, M. R. (2004). Handbook of Computational Methods for Integration (1st ed.). New York: Chapman and Hall/CRC. https://doi.org/10.1201/9780203490303
5. Burg, C. and Degny, E. (2013) Derivative-Based Midpoint Quadrature Rule. *Applied Mathematics*, **4**, 228-234. doi: 10.4236/am.2013.41A035.
6. Peer, M. (2015). Tangent Line and Tangent Plane Approximations of Definite Integral. *Rose-Hulman Undergraduate Mathematics Journal*: Vol. 16: Iss. 2, Article 8.
7. Ullah, M. A. (2015). Numerical Integration and a Proposed Rule. American Journal of Engineering Research, 4(9), 120-123.

Appendices:

A) MATLAB Code for the Proposed Three-Point Chebyshev Quadrature Rule

```
function I = chebyshev3_quad(f, a, b, n)
%CHEBYSHEV3 Composite three-point Chebyshev quadrature
%   I = chebyshev3(f, a, b, n) approximates the integral of f from a to b
%   using n subintervals (n must be even)
%
%   Inputs:
%       f : function handle (e.g., @(x) x.^2)
%       a : lower limit of integration
%       b : upper limit of integration
%       n : number of subintervals (must be even)
%
%   Output:
%       I : approximate integral of f from a to b
    format long

    if mod(n,2) ~= 0
        error('Number of subintervals n must be even.');
    end

    h = (b - a) / n;          % subinterval width
    lambda = (2 - sqrt(3)) / 4;  % Chebyshev node parameter
    I = 0;                     % initialize integral

    % Apply the 3-point Chebyshev quadrature on each pair of subintervals
    for i = 0:2:(n-2)
        x0 = a + i*h;
        x2 = a + (i+2)*h;
        z0 = x0 + 2*lambda*h;
        z1 = (x0 + x2)/2;
        z2 = x2 - 2*lambda*h;

        % Integral over this panel
        I_panel = (2*h/9) * (2*f(z0) + 5*f(z1) + 2*f(z2));
        I = I + I_panel;
    end
end
```

B) Example 1: $\int_{0.1}^{2.5}(3\ln x + 2x^2)\,dx$ with $n = 12$ (number of subinterval).

```
>> I = chebyshev3_quad(@(x) 3*log(x)+2*x^2, 0.1, 2.5, 12)

I =

  10.774880620574198
```

C) Example 2: $\int_0^1 \sqrt{1-x^2}\,dx$ with $k = 2$ (number of application of the rule).

```
>> I = chebyshev3_quad(@(x) sqrt(1-x^2), 0, 1, 4)

I =

   0.784512523002727
```

For k applications of the Chebyshev rule, the number of subintervals $n = 2k$.

Journal of Science-FAS-SEUSL (2025) 06(02) 35-47
ISSN:2738-2184

Exact Relativistic Charged Stellar Models with Anisotropic Stresss

K. Moulis* and K. Komathiraj

Department of Mathematical Sciences, Faculty of Applied Sciences, South Eastern University of Sri Lanka, Sammanthurai 32200

*moulisanis@gmail.com

Abstract

In this work, we introduce a formal framework to derive interior solutions for the Einstein-Maxwell system, describing the configuration of a relativistic charged fluid sphere within the context of spherically symmetric gravitational fields, which are matched to the exterior Reissner-Nordstrom space–time. Building upon previous methodologies, particularly the innovative approach by Komathiraj and Sharma (2018), we refine the process by reducing the system to a recurrence relation with variable rational coefficients. This enables us to obtain a solution in terms of an infinite series. We demonstrate that it is possible to closed-form solutions within a specific range of model parameters. By impressive constraints on these variables, we reduce the outcomes to denote them in component of standard functions, strengthening their availability and understandability. The streamlined framework requires computing results through series analysis and solving resulting difference equations, at last providing formulations in the form of polynomials and products consisting of algebraic relations. Our study presents an extensive set of general solutions, providing understanding into the nature of charged fluid spheres in relativistic astrophysical context.

Keywords*:* Einstein-Maxwell system, Exact solutions, Differential equation, closed-form solution, Frobenius method, Recurrence formula

1. Introduction

General relativity is amongst the best theories of modern physics, which originated from simple intuition and emerges as a physical theory of prediction. It plays an important role in understanding the gravitational behavior of massive bodies in relativistic astrophysics. It has revolutionized the understanding of spacetime and the gravitational field. The interpretation of general relativistic phenomena results in the manifestation of the curvature of the spacetime produced by the presence of massive bodies. General relativity can be summed up in two statements. Firstly, spacetime is a curved pseudo-Riemannian manifold with an indefinite metric tensor field. Secondly, the relationship between the matter content and the curvature of spacetime is contained in the Einstein field equations. Shapiro Saul A Teukolsky et al in 1983 pointed out that general relativity models could be utilized in the study of strong gravitational fields and black holes for which the Newtonian gravity models are not suitable. We utilize the Riemann tensor for defining the curvature of spacetime and the energy momentum tensor for matter distributions and the contribution of the electromagnetic field in the presence of charge. The Einstein field equations link the curvature to the total energy momentum. The Bianchy identity ensures conservation of energy momentum.

In relativistic astrophysics, we construct mathematical models which describe the behavior of highly dense objects. These include models of gravitational collapse leading to black holes, neutron stars, pulsars and magnetars, characterized by extremely powerful magnetic fields,

Corresponding Author: moulisanis@gmail.com

and extreme concentrations of energy such as gamma-ray bursts. Exact general relativistic models are relevant to study observed astrophysical processes. In this context spherically symmetric stellar models are important and they are extensively used in several applications. In astrophysics, the collapse of a stellar body can be accurately described by a spherically symmetric gravitational field as mentioned by Shapiro Saul A Teukolsky et al. Historically, the fundamental exact solutions found in relativistic astrophysics are listed as follows; The first exact solution to the Einstein field equations is the Schwarzchild exterior solution. The Schwarzchild interior solution describes the interior stellar gravitational field, with constant energy density. For small stars having low pressures, this approach gives an acceptable approximation. For a static spherically symmetric charged star, the Reissner-Nordstrom solution describes the exterior gravitational field. The Kerr solution is associated with the exterior of the body in rotating motion which is characterized by its mass and angular momentum. The Kerr-Newman solution is associated with the exterior of a charged rotating body. These exact solutions of the Einstein-Maxwell system are essential for describing astrophysical processes.

The Einstein-Maxwell system of equations is relevant in describing charged compact objects characterized by a strong gravitational field, such as neutron stars. The investigations of Ivanov, 2002 and Sharma et al, 2001demonstrate that the values of redshifts, luminosities and maximum mass of a compact relativistic star are affected by the presence of electromagnetic field and anisotropy. The works of Mak & Harko, 2004, Komathiraj & Maharaj, 2007a, Komathiraj & Maharaj, 2007b and Maharaj & Komathiraj, 2007 show the significant role of the electromagnetic field in describing the gravitational behavior of compact stars composed of quark matter. In the recent past, several scientists have tried to apply different approaches of finding solutions to the field equations. By a specific choice of the electric field, Hansraj & Maharaj, 2006 obtained solutions with isotropic pressures to the Einstein-Maxwell system. These solutions satisfy a barotropic equation of state and contain the Rej et al, 2021 model.

The Einstein–Maxwell equations are expressed in natural units where, and derivatives with respect to the radial coordinate are denoted by a prime (′). The energy density and pressure are defined relative to the comoving four-velocity of the fluid, while the electric field and charge density are incorporated using the electromagnetic energy–momentum tensor and the Maxwell equations. Overall, this study aims to derive and analyze new closed-form, physically meaningful solutions to the Einstein–Maxwell field equations. These models contribute to a deeper understanding of the role of charge and anisotropy in compact astrophysical bodies and help interpret the structure and stability of relativistic stellar configurations.

2. Methodology.

2.1 Einstein-Maxwell system

The line element for a static spherically symmetric spacetime, modelling the interior of the relativistic star, has the form,

$$ds^2 = -e^{-2v(r)}\,dt^2 + e^{-2\lambda(r)}\,dr^2 + r^2(d\theta^2 + sin^2\theta\,d\emptyset^2)\pi r^2 \quad (2.1)$$

where $v(r)$ and $\lambda(r)$ are arbitrary functions of the radial coordinate r. The Einstein–Maxwell field equations for the line element (2.1) are then obtained (in system of units having $8\pi G = c = 1$) as,

$$\frac{1}{r^2}\left(1 - e^{-2\lambda}\right) + \frac{2\lambda'}{r}\,e^{-2\lambda} = \rho + \frac{1}{2}E^2 \quad (2a)$$

$$\frac{-1}{r^2}\left(1 - e^{-2\lambda}\right) + \frac{2v'}{r}\,e^{-2\lambda} = p_r + \frac{1}{2} \quad (2b)$$

$$e^{-2\lambda}\left(v'' + v'^2 + \frac{v'}{r} - v'\lambda' - \frac{\lambda'}{r}\right) = p_t + \frac{1}{2}E^2 \quad (2c)$$

$$\frac{1}{r^2}e^{-\lambda}(r^2E)' = \rho + \frac{1}{2}E^2 \quad (2d)$$

The system incorporates the electric field intensity E and proper charge density σ through the energy-momentum tensor associated with the electromagnetic field and the Maxwell equations.

An alternative yet equivalent expression for the field equations can be formulated by introducing a new independent variable, denoted as x, and defining new functions y and Z as follows

$$x = Cr^2,\ A^2y^2(x) = e^{2v(r)},\ Z(x) = e^{2\lambda(r)} \quad (2.2)$$

Proposed by Durgapal & Bannerji, 1983where A and C are constants. Utilizing the transformation given in equation (2.2) the system (2) can be written in the following in the form as:

$$\frac{1-Z}{x} + \frac{2\lambda'}{r}\,e^{-2\lambda} = \frac{\rho}{C} + \frac{E^2}{2C} \quad (2.3a)$$

$$\frac{Z-1}{x} + 4Zx^2\ddot{y} = \frac{p_r}{C} - \frac{E^2}{2C} \quad (2.3b)$$

$$4Zx^2\ddot{y} + 2\dot{Z}x^2\dot{y} + (\dot{Z}x - Z + 1 - \frac{\Delta x}{C} - \frac{E^2x}{2C} = 0 \quad (2.3c)$$

$$\frac{4Z}{x}\left(x\dot{E} + E\right)^2 = \frac{\sigma^2}{C} \quad (2.3d)$$

Dots (·) in the equation (2.3) denote differentiation w.r.t the variable x. The system (2.3) establishes the gravitational characteristics of a charged perfect fluid with anisotropic pressure. Where $\Delta = p_t - p_r$ is the anisotropic factor or measure of anisotropy. As a result, we are presented with a linear system consisting of four independent equations involving seven unknown variables: ρ, p_r, p_t, E, σ, y and Z. The notable feature of this system is its capacity for obtaining a solution, achieved through appropriate substitutions of Z, E and Δ by integrating the second-order differential equation (2.3c), which happens to be linear in y.

2.2. Integration procedure

We study a particular form of the Einstein-Maxwell system (2.5.3) by making explicit choices for one of the gravitational potentials Z, electric field intensity E and the anisotropic factor Δ. For the metric function Z, we make the particular choice

$$Z = \frac{1+kx}{1+mx} \tag{2.2.1}$$

where k is a real constant. In (2.2.1) we take $k \neq 1$ to avoid negative energy densities which are unphysical for barotropic stars. The choice (2.2.1) was also made by Maharaj & Mkhwanazi, 1996 in their analysis of uncharged relativistic stars. Also observe that when $k = 0$ we regain the metric function considered by Hansraj & Maharaj, 2006 which generalizes the Finch and Skea neutron star model (1989). We have chosen the above form as it provides for a wider range of possibilities than the solutions of Hansraj & Maharaj, 2006, and it does produces charged and uncharged solutions which are necessary for a realistic model. Upon substituting (2.2.1) into (2.3c), the following is obtained

$$4(1+kx)(1+mx)\ddot{y} + 2(k-m)\dot{y} + \left[m(m-k) - \frac{(E^2+\Delta)(1+mx)^2}{Cx}\right] y = 0 \tag{2.2.2}$$

At this stage, we find it convenient to introduce the following transformation

$$z = 1 + mx \tag{2.2.3}$$

This transformation allows us to express the second-order differential equation (2.2.2) in a more straightforward and simplified manner.

$$4z(kz+m-k)\frac{d^2\tilde{y}}{dz^2} + 2(k-m)\frac{d\tilde{y}}{dz} + \left[(m-k) - \frac{\Delta}{C}\frac{Z^2}{Z-1}\frac{E^2z^2}{C(Z-1)}\right]\tilde{y} = 0 \tag{2.2.4}$$

Expressed in terms of the new dependent and independent variables, denoted as $\tilde{y} = y(z)$ and z respectively, integration of equation (2.2.4) requires the specification of the electric field intensity E and the anisotropic factor Δ. Although there exists a variety of choices for E and Δ, only a subset is deemed physically reasonable and capable of yielding closed-form solutions. To make (3.2.4) integrable, we choose the following particular forms for E and Δ,

$$\frac{E^2}{C} = \alpha\ \frac{(z-1)}{z^2} \quad \text{and} \quad \frac{\Delta}{C} = \beta\ \frac{(z-1)}{z^3} \tag{2.2.5}$$

Here, α and β are constants. The form of E^2 in equation (2.2.5) is considered physically acceptable as E remains regular and continuous throughout the sphere. It is important to note that $E = 0$ at $r = 0$. Various special cases of equation (2.2.5) have been previously examined by Takisa & Maharaj, 2013 and John & Maharaj, 2011, and they can also be reduced to the uncharged stellar model developed by Maharaj & Mkhwanazi, 1996. The form in (2.2.5) chosen for Δ ensures that anisotropy also vanishes at the center of the star (i.e. $p_r = p_t$ at the center). By substituting equation (2.2.5) into equation (2.2.4), we obtain

$$4z^2(kz+m-k)\frac{d^2\tilde{y}}{dz^2}+2z(k-m)\frac{d\tilde{y}}{dz}+\ [(m-k-\alpha)z-\ \beta\ ]\tilde{y}\ =0 \qquad (2.2.6)$$

This represents the master equation for the system of equations (2.5.3). When $\alpha = \beta = 0$, the differential equation (3.2.7) simplifies to:

$$4z\ \ (kz+m-k)\frac{d^2\tilde{y}}{dz^2}+2(k-m)\frac{d\tilde{y}}{dz}+\ [m-k]\tilde{y}\ =0 \qquad (2.2.7)$$

This represents the limiting condition and corresponds to an uncharged isotropic sphere.

2.3 General series solution

Obtaining a closed-form solution for the equation (2.2.6) proves challenging. However, it is possible to transform it into a differential equation suitable for integration using the Frobenius method. This transformation is carried out as follows, we introduce a new function u(z) such that

$$\tilde{y}\ =\ z^d u(z) \qquad (2.3.1)$$

Here, d represents a constant, and a similar type of transformation was previously employed by Komathiraj & Maharaj, 2007 in generating charged stellar models. With the aid of equation (2.3.1), the differential equation (2.2.6) can be reformulated as

$$4z(kz+m-k)\frac{d^2u}{dz^2}+2z[\ 4d(kz+m-k)+(k-m)\ ]\ \frac{du}{dz}-\{\ [k-m\ +\ \alpha-4kd(d-1)]z+2d(2d-3)(k-m)+\beta\ \}\ u\ =0 \qquad (2.3.2)$$

A significant simplification of the equation can be attained by setting

$$\beta\ =\ -[2d(2d-3)(k-m)] \qquad (2.3.3)$$

Consequently, Equation (2.3.2) transforms into

$$4z(z-c)\frac{d^2u}{dz^2}+2[\ 4d(z-c)+c\ ]\ \frac{du}{dz}-\ [c+\ \tilde{\alpha}-4d(d-1)]u\ =0 \qquad (2.3.4)$$

we have established

$$c=\frac{k-m}{k},\ k\tilde{\alpha}=\ \alpha \qquad (2.3.5)$$

Since the point $z = c$ is a special type of singular point known as a regular singular point for Equation (2.3.4), there are two solutions that can be expressed as power series centered around $z = c$. Consequently, we can represent the solution to the differential equation (3.3.4) using the Frobenius method.

$$u=\ \sum_{i=0}^{\infty} c_i(z-c)^{i+b}\ ,\ c_0\neq 0 \qquad (2.3.6)$$

where c_i represent the coefficients of the series and while b stands for a constant value.

To obtain a valid solution, it is essential to find both the coefficients c_i and the parameter b. By substituting expression (2.3.6) into the differential equation (2.3.4), we derive an equation known as the indicial equation,

$$2cc_0b(2b-1)=0$$

and the recurrence formula is

$$c_{i+1}=-\frac{\{4(i+b)(i+b-1+2d)-T\}}{2c(i+b+1)(2i+2b+1)}c_i \tag{2.3.7}$$

Considering $i \geq 0$ and $T = c+\tilde{\alpha}-4d(d-1)$, and given that $c_0 = 0$ and $c = k-m = 0$, we must choose $b=0 \; or \; b=\frac{1}{2}$. The coefficients $c_1, c_2, c_3....$ can be expressed in relation to the initial coefficient c_0. This expression is given by

$$c_{i+1}=\prod_{p=0}^{i}-\frac{\{4(p+b)(p+b-1+2d)-T\}}{2c(p+b+1)(2p+2b+1)}c_0 \tag{2.3.8}$$

The expression (2.3.8) can be rigorously derived using the principle of mathematical induction. By applying this method, we can create two solutions that are linearly independent for Equation (2.3.4), utilizing expressions (2.3.6) and (2.3.8). When $b = 0$, the first solution is obtained as follows,

$$u_1=c_0\left[1+\sum_{i=0}^{\infty}\prod_{p=0}^{i}-\frac{\psi}{\eta}(z-c)^{i+1}\right]$$

Where,

$$\psi = 4p(p-1+2d)-[c+\tilde{\alpha}-4d(d-1)] \; and \; \eta = 2c(p+b+1)(2p+2b+1)$$

When $b=\frac{1}{2}$, the second solution is obtained as follows,

$$u_2=c_0(z-c)^{\frac{1}{2}}\left[1+\sum_{i=0}^{\infty}\prod_{p=0}^{i}-\frac{\alpha}{\beta}(z-c)^{i+1}\right]$$

Where $\alpha=(2p+1)(2p-1+2d)-[c+\tilde{\alpha}-4d(d-1)] \; and \; \beta=c(2p+3)(2p+2)$

Thus, we achieve a comprehensive solution for Equation (3.3.4) since the functions u_1 and u_2 exhibit linear independence. Expressing these functions in the original variable $x = Cr^2$, we obtain

$$y_1=c_0(1+mx)^d\left[1+\sum_{i=0}^{\infty}\prod_{p=0}^{i}-\frac{\psi_1}{\eta_1}\left[\frac{m(1+kx)}{k}\right]^{i+1}\right] \tag{2.3.9}$$

$$y_2=c_0(1+mx)^d\left[\frac{m(1+kx)}{k}\right]^{1/2}\left[1+\sum_{i=0}^{\infty}\prod_{p=0}^{i}-\frac{\alpha_1}{\beta_1}\left[\frac{m(1+kx)}{k}\right]^{i+1}\right] \tag{2.3.10}$$

The solutions y_1 and y_2 given in equations (2.3.9) and (2.3.10) respectively, generate the two linearly independent solutions to the differential equation (2.2.2) in terms of infinite series for appropriate values of the parameters k, m, α, and β. Therefore, the general solution to the differential equation (2.2.2), considering the specified electric field and anisotropic factor from equation (2.2.5), can be expressed as

$$y(x) = A_1 y_1(x) + A_2 y_2(x) \tag{2.3.12}$$

Here, A_1 and A_2 represent arbitrary constants and y_1 and y_2 are given in equations (2.3.9) and (2.3.10) respectively. By utilizing equation (2.5.3) and combining it with equation (2.3.12), we formulate the precise solution for the Einstein–Maxwell system in the following manner

$$e^{2\lambda} = \frac{(1+mx)}{1+kx} \tag{2.3.13a}$$
$$e^{2\nu} = A^2 y^2 \tag{2.3.13b}$$
$$\frac{\rho}{C} = \frac{(m-k)(3+m\dot{x})}{(1+mx)^2} - \alpha \frac{mx}{2(1+mx)^2} \tag{2.3.13c}$$
$$\frac{p}{C} = \frac{4(1+kx)}{(1+mx)}\frac{\dot{y}}{y} + \frac{k-m}{(1+mx)} + \alpha \frac{mx}{2(1+mx)^2} \tag{2.3.13d}$$
$$\Delta = p_t - p_r$$
$$p_t = \Delta + p_r \tag{2.3.13e}$$
$$\frac{E^2}{C} = \alpha \frac{mx}{(1+mx)^2} \tag{2.3.13f}$$
$$\frac{\Delta}{C} = \beta \frac{mx}{(1+mx)^3} \tag{2.3.13g}$$

Since the combined consideration of the metric function from equation (2.2.1) along with the electric field intensity and the anisotropic factor specified in equation (2.2.5) has not been explored before, as far as our knowledge extends, the set of solutions given by equation (2.3.13) has not been documented or reported before. An interesting aspect of this new family of solutions is that, by choosing $\alpha = 0$ and $\beta = 0$ ($d = 0$ *or* $d = 3/2$), we switch off the anisotropic factor in (2.3.13), then we regain the solutions for an isotropic charged case directly. Additionally, the solution provided in equation (2.3.13) is expressed in terms of a series involving real arguments, as opposed to complex arguments that may arise when utilizing mathematical software packages.

2.4 Terminating series

An engaging observation is that the series presented in equations (2.3.9) and (2.3.10) concludes for certain values of the parameters *k*, *m*, *α*, and *d*. This implies the potential to derive solutions in terms of elementary functions by imposing particular constraints on these parameters. Consequently, solutions can be expressed using polynomials and algebraic functions. In our approach, we opt to utilize the recurrence relation (2.3.7) instead of the series expressions (2.3.9) and (2.3.10) to obtain these elementary solutions.

2.4.1 Elementary solutions

By setting $b = 0$ in equation (2.3.7) and establishing that $c + \tilde{\alpha} - 4d(d-1) = 4n(n-1+2d)$ for integer values of n, we arrive at the following result,

$$c_{i+1} = 4\frac{(n-i)(n+i-1+2d)}{c(2i+1)(2i+2)} c_i \quad i \geq 0, \tag{2.4.1}$$

where n is a fixed integer, it's Obviously $c_{n+1} = 0$. As a result, the remaining coefficients c_{n+2}, c_{n+3}, c_{n+4} .... vanish. Solving Equation (2.4.1) leads to the following outcome,

$$c_i = \left(\frac{4}{c}\right)^i \frac{4n!(n+i-2+2d)!}{(2i)!\,(n-i)!\,(n-2+2d)!} c_0, \qquad 0 \leq i \leq n. \tag{2.4.2}$$

Using (2.3.6) (when b=0) and (2.4.2), we arrive at the following result,

$$u(z) = \sum_{i=0}^{n} \left(\frac{4}{c}\right)^{i} \frac{n!(n+i-2+2d)!}{(2i)!\,(n-i)!\,(n-2+2d)!}(z-c)^{i}, \tag{2.4.3}$$

where $c + \tilde{\alpha} - 4d(d-1) = 4n(n-1+2d)$.

By inserting b = $\frac{1}{2}$ into equation (2.3.7) and establishing that $c + \tilde{\alpha} - 4d(d-1) = (2n+1)(2n-1+4d)$, we arrive at the following result,

$$c_{i+1} = 4\frac{(n-i)(n+i+2d)}{c(2i+3)(2i+2)}c_i,\ i \geq 0 \tag{2.4.4}$$

where n is a fixed integer, it's Obviously $c_{n+1} = 0$. Consequently, the subsequent coefficients $c_{n+2}, c_{n+3}, c_{n+4}, \ldots$ vanish. Solving Equation (2.4.4) results in,

$$c_i = \left(\frac{4}{c}\right)^{i} \frac{n!(n+i-1+2d)!}{(2i+1)!\,(n-i)!\,(n-1+2d)!}c_0, \quad 0 \leq i \leq n. \tag{2.4.5}$$

Using (2.3.6) (when b = $\frac{1}{2}$) and (2.4.5), we arrive at the following result,

$$u(z) = c_0(z-c)^{\frac{1}{2}} \sum_{i=0}^{n} \left(\frac{4}{c}\right)^{i} \frac{n!(n_1+1)!}{(2i+1)!\,(n-i)!n_1!}(z-c)^{i} \tag{2.4.6}$$

where $n_1 = (n-1+2d)$ and $c + \tilde{\alpha} - 4d\,(d-1) = (2n+1)\,(2n-1+4d)$.

The expression represented by polynomial (2.4.3) and the product involving the polynomial and algebraic function (2.4.6) collectively produce a first solution for the given differential equation (2.3.4), provided that the parameters c, $\tilde{\alpha}$, and d assume appropriate values.

2.4.2 General solutions

Solutions to equation (2.3.4) can be derived by constraining the values of c, $\tilde{\alpha}$, and d in a manner that allows only elementary functions to remain. These elementary functions can be represented as polynomials and products of polynomials with algebraic functions. Employing expression (2.4.3), we articulate the initial set of general solutions to the differential equation (3.3.4) in the following format

$$u(z) = \sum_{i=0}^{n} \left(\frac{4}{c}\right)^{i} \frac{n!(n+i-2+2d)!}{(2i)!\,(n-i)!\,(n-2+2d)!}(z-c)^{i} \times \left[B_1 + B_2 \int \frac{z^{\left(\frac{1}{2}\right)-2d}(z-c)^{-1/2}}{\left[\sum_{i=0}^{n}\left(\frac{4}{c}\right)^{i}\frac{n!(n_2+1)!}{(2i)!\,(n-i)!n_2!}(z-c)^{i}\right]^{2}}dz\right] \tag{2.4.7}$$

Utilizing expression (2.4.6), the second category of general solutions for equation (2.3.4) is acquired in the following manner,

$$\mathrm{u(z)} = (z-c)^{\frac{1}{2}} \sum_{i=0}^{n} \left(\frac{4}{c}\right)^{i} \frac{n!\,(n_1+1)!}{(2i+1)!\;(n-i)!\,n_1!}(z-c)^{i} \times \\ \times \left[B_1 + B_2 \int \frac{z^{\left(\frac{1}{2}\right)-2d}(z-c)^{-\frac{3}{2}}}{\left[\sum_{i=0}^{n}\left(\frac{4}{c}\right)^{i} \frac{n!\,(n_1+1)!}{(2i+1)!\;(n-i)!\,n_1!}(z-c)^{i}\right]^{2}} dz\right] \tag{2.4.8}$$

Where $c + \tilde{\alpha} - 4d\,(d-1) = (2n+1)(2n-1+4d)$.

In equations (2.4.7) and (2.4.8), B_1 and B_2 represent integration constants. When expressed in terms of the original variable $x = Cr^2$, equation (2.4.7) can be reformulated in the following manner,

$$\mathrm{y(x)} = (1+mx)^{d} \sum_{i=0}^{n} \left(\frac{4k}{k-m}\right)^{i} \frac{n!(n_2+i)!}{(2i)!\,(n-i)!n_2!} \times \left[C_1 + C_2 \int \frac{(1+mx)^{\left(\frac{1}{2}\right)-2d}(1+kx)^{-\frac{1}{2}}}{\left[\sum_{i=0}^{n}\left(\frac{4k}{k-m}\right)^{i} \frac{n!(n_2+i)!}{(2i)!\,(n-i)!n_2!}t^{i}\right]^{2}} dx\right], \tag{2.4.9}$$

where $4 - m + \alpha - 4kd(d-1) = 4kn(n-1+2d)$

Equation (2.4.8) in terms of $x = Cr^2$, adopts the following representation,

$$\mathrm{y(x)} = C_3 \sum_{i=0}^{n} \left(\frac{4k}{k-m}\right)^{i} \frac{n!(n_1+1)!}{(2i+1)!\,(n-i)!n_1!} \times \left[C_1 + C_2 \int \frac{(1+mx)^{\left(\frac{1}{2}\right)-2d}(1+kx)^{-\frac{3}{2}}}{\left[\sum_{i=0}^{n}\left(\frac{4k}{k-m}\right)^{i} \frac{n!(n_1+i)!}{(2i+1)!\,(n-i)!n_1!}t^{i}\right]^{2}} dx\right], \tag{2.4.10}$$

Consequently, we have formulated two categories of solutions, denoted as (2.4.9) and (2.4.10), addressing the differential equation (2.2.2) under the assumed electric field and anisotropic factor (2.2.5). It's important to emphasize that these classes of solutions are versatile and can be applied to investigate stellar characteristics both in the presence and absence of charge and anisotropic pressure. By setting $\alpha = 0$ within expressions (2.4.9) and (2.4.10), solutions for an uncharged anisotropic sphere are obtained. Also, when $\beta = 0$ (resulting in $d = 0$ or $\frac{3}{2}$) (2.4.9) and (2.4.10), become charged isotropic models.

The solution in (2.4.9) and (2.4.10) have a simple form, and they have been expressed completely as combinations of polynomials and algebraic functions. This has the advantage of simplifying the investigation into the physical properties of charged dense stars with pressure anisotropy. We are now prepared to perform the integration of equations (2.4.9) and (2.4.10) with respect to specific values assigned to the parameters k, m, α, d, and n. When $n = 0$, equation (2.4.9) becomes,

$$\mathrm{y(x)} = (1+mx)^{d} \left[C_1 C_2 \int \frac{1}{(1+mx)^{2d-\left(\frac{1}{2}\right)}[(1+kx)]^{\frac{1}{2}}} dx\right], \tag{2.4.11}$$

where $k - m + \alpha - 4kd\,(d - 1) = 0$.

Similarly, when $n = 0$, equation (2.4.10) takes the following form,

$$\mathrm{y(x)} = C_3 \left[C_1 + C_2 \int \frac{1}{(1+mx)^{2d-\left(\frac{1}{2}\right)}[(1+kx)]^{\frac{3}{2}}} dx\right], \tag{2.4.12}$$

where $2k - m + \alpha - 4kd^2 = 0$.

By choosing $k = -1/2$, $m = 1$, $\alpha = 0$ and $d = 3/2$ (or $\beta = 0$) within expression (3.4.11), we derive the following result,

$$y(x) = a_1(1+x)^{\frac{3}{2}} + a_2(2-x)^{\frac{1}{2}}(5+2x),$$

we make the assumptions $a_1 = C_1$ and $a_2 = -(2\ 2/27)C_2$. Consequently, we have successfully recovered the solution initially proposed by Durgapal & Bannerji, 1983. The were was Durgapal & Bannerji, 1983 model were Comprehensively studied and it was demonstrated that their Solutions produced a neutral be relativistic sphere that satisfied all physical criteria.

By choosing $k = 1/2$, $m = 1$, $\alpha = 0$ and $d = 0$ (or $\beta = 0$) within expression (2.4.12), we derive the following result,

$$y(x) = (2+x)^{\frac{1}{2}}\left(a_1 + a_2 \ln\left[(1+x)^{\frac{1}{2}} + (2+x)^{\frac{1}{2}}\right]\right) - a_2(1+x)^{1/2}$$

We make the assumptions $a_1 = C_1 / 2$ and $a_2 = 4C_2$. This particular set of solutions was previously identified by Maharaj & Mkhwanazi, 1996. The Maharaj & Mkhwanazi, 1996 model Satisfies all the physical conditions for an isolated spherically symmetric stellar source, and consequently has been utilized by many researchers to model neutral stars.

By choosing $k = 1/3$, $m = 1$, $\alpha = 1/3$ and $d = 0$ (or $\beta = 0$) within expression (2.4.12), we derive the following result,

$$y(x) = (3+x)^{\frac{1}{2}}\left(a_1 + a_2 \ln\left[(1+x)^{\frac{1}{2}} + (3+x)^{\frac{1}{2}}\right]\right) - a_2(1+x)^{1/2}$$

we make the assumptions $a_1 = C_1 / 3$ and $a_2 = 6C_2$ Notably, this specific solution aligns with the charged stellar model presented by John and Maharaj (2011). It's worth mentioning that a minor error identified in the John & Maharaj, 2011 has been rectified in this current work. The John & Maharaj, 2011 solution has been widely applied as a relativistic model for charged isotropic Stars with super dense matter.

3. Results and Discussion

Our aim in this thesis was to discover fresh exact solutions for the Einstein-Maxwell systems, specifically focusing on static spherically symmetric gravitational fields with a barotropic equation of state. We specifically opted for a linear equation of state linking energy density to radial pressure, with applications in modeling relativistic stars in astrophysical contexts. The solutions we've derived are believed to be physically plausible and could be instrumental in understanding dense stellar bodies within the framework of general relativity.

we make for physically sensible selections for the gravitational potential the intensity of the electric field and the anisotropic factor. These choices are made based on their respective form,

$$Z = \frac{1+kx}{1+mx}$$

$$\frac{E^2}{C} = \alpha \frac{mx}{(1+mx)^2}$$

$$\frac{\Delta}{C} = \beta \frac{mx}{(1+mx)^3}$$

We regain the findings of Komathiraj & Sharma, 2018and emphasize the presence of a singularity in the charge density at the center of the sphere. We observed that the condition of pressure isotropy can be written as,

$$4z^2(kz+m-k)\frac{d^2\tilde{y}}{dz^2} + 2z(k-m)\frac{d\tilde{y}}{dz} + [(m-k-\alpha)z - \beta\ ]\tilde{y} = 0$$

We've introduced a fresh method for generating a wide range of solutions to the Einstein-Maxwell system. This involves utilizing the transformation equations proposed by Durgapal & Bannerji, 1983 alongside a specific decay pattern for the electric field intensity. Many solutions obtained earlier are encompassed within our broader set of solutions. Additionally, we've illustrated that closed form solutions can be derived from the general series solution for specific model parameters. It's worth noting that the variety of solutions heavily relies on transformation: $\tilde{y} = z^d u(z)$. It's important to emphasize that while the integral forms represented by equations,

$$\mathrm{y(x)} = (1+mx)^d \sum_{i=0}^{n} \left(\frac{4k}{k-m}\right)^i \frac{n!\,(n_2+i)!}{(2i)!\ (n-i)!\ n_2!} \times \left[C_1 + C_2 \int \frac{(1+mx)^{\left(\frac{1}{2}\right)-2d}(1+kx)^{-\frac{1}{2}}}{\left[\sum_{i=0}^{n} \left(\frac{4k}{k-m}\right)^i \frac{n!\,(n_2+i)!}{(2i)!\ (n-i)!\ n_2!} \frac{m(1+kx)^i}{k}\right]^2} dx \right] \tag{4.0.2}$$

And

$$y(x) = C_3 \sum_{i=0}^{n} \left(\frac{4k}{k-m}\right)^i \frac{n!(n_1+1)!}{(2i+1)!\,(n-i)!n_1!} \times \left[C_1 + C_2 \int \frac{(1+mx)^{\left(\frac{1}{2}\right)-2d}(1+kx)^{-\frac{3}{2}}}{\left[\sum_{i=0}^{n}\left(\frac{4k}{k-m}\right)^i \frac{n!(n_1+i)!}{(2i+1)!\,(n-i)!n_1!}t^i\right]^2} dx \right] \quad (4.0.3)$$

parameterized by *d*, don't immediately allow for the recovery of previously obtained charge-independent solutions, this can be achieved at a later point.

Once the integrations outlined in equations (4.0.2) and (4.0.3) are conducted and yield closed-form results for particular model parameters, both the charged and uncharged solutions expressed in elementary functions can be independently derived.

This method has been applied to recover the stellar solutions proposed by Durgapal & Bannerji, 1983 and Maharaj & Mkhwanazi, 1996, as well as the charged fluid solution by John & Maharaj, 2011. In conclusion, we've introduced two distinct closed-form solutions for the Einstein-Maxwell system. The simplicity of these solutions aids in effectively analyzing the physical behavior of a charged fluid sphere. Notably, our solution also yields a barotropic equation of state. However, it's important to note that closed-form solutions have only been generated for specific values of the model parameters. These solutions are suitable for modeling a charged relativistic sphere with anisotropic pressures. Notably, we've identified models that exhibit regularity at the center for the charge density, representing an advancement over the outcomes of Thirukkanesh & Maharaj, 2008.

4. Conclusion

In this project, we successfully derived new exact solutions to the Einstein-Maxwell system for static, spherically symmetric charged fluid spheres with anisotropic pressures. By employing a barotropic equation of state and using a linear relationship between energy density and radial pressure, we explored models relevant to relativistic stars. Our method, built upon the transformation proposed by Durgapal and Bannerji, allowed for the recovery of previously known solutions while also generating novel solutions. These closed-form solutions provide valuable insights into the physical behavior of charged compact objects, particularly in terms of regularity at the center, offering significant improvements over earlier models.

References

[1] Durgapal, M. C., & Bannerji, R. (1983). New analytical stellar model in general relativity. In *PHYSICAL REVIEW D* (Vol. 27).

[2] Hansraj, S., & Maharaj, S. D. (2006). Charged analogue of Finch-Skea stars. *International Journal of Modern Physics D*, *15*(8), 1311–1327.

[3] Ivanov, B. V. (2002). Static charged perfect fluid spheres in general relativity. *Physical Review D*, *65*(10).

[4] John, A. J., & Maharaj, S. D. (2011). Relativistic stellar models. *Pramana - Journal of Physics*, *77*(3), 461–468.

[5] Komathiraj, K., & Maharaj, S. D. (2007a). Tikekar superdense stars in electric fields. *Journal of Mathematical Physics*, *48*(4).

[6] Komathiraj, K., & Maharaj, S. D. (2007b). *Tikekar superdense stars in electric fields*.

[7] Komathiraj, K., & Sharma, R. (2018). A family of solutions to the Einstein–Maxwell system of equations describing relativistic charged fluid spheres. *Pramana - Journal of Physics*, *90*(5).

[8] Maharaj, S. D., & Komathiraj, K. (2007). *Generalised compact spheres in electric fields*.

[9] Maharaj, S. D., & Mkhwanazi, W. T. (1996). Some static relativistic solutions. *Quaestiones Mathematicae*, *19*(1–2), 211–217.

[10] Mak, M. K., & Harko, T. (2004). *Quark stars admitting a one-parameter group of conformal motions*.

[11] Rej, P., Siddiqa, A., Abbas, G., & Bhar, P. (2021). 0:46 WSPC/INSTRUCTION FILE fs. *International Journal of Geometric Methods in Modern Physics*.

[12] Shapiro Saul A Teukolsky, S. L., LEY-VCH WILEY-VCH Verlag GmbH, W. I., & KGaA, C. (n.d.). *Black Holes, White Dwarfs, and Neutron Stars THE PHYSICS OF COMPACT OBJECTS*.

[14] Sharma, R., Mukherjee, S., & Maharaj, S. D. (2001). General Solution for a Class of Static Charged Spheres. In *General Relativity and Gravitation* (Vol. 33, Issue 6).

[15] Takisa, P. M., & Maharaj, S. D. (2013a). Some charged polytropic models. *General Relativity and Gravitation*, *45*(10), 1951–1969.

[16] Takisa, P. M., & Maharaj, S. D. (2013b). *Some charged polytropic models*.

[17] Thirukkanesh, S., & Maharaj, S. D. (2008). *Charged anisotropic matter with linear equation of state*.

[18] Thirukkanesh, S., & Maharaj, S. D. (2009). Charged relativistic spheres with generalized potentials. *Mathematical Methods in the Applied Sciences*, *32*(6), 684–701.

Journal of Science-FAS-SEUSL (2025) 06(02) 48-58
ISSN:2738-2184

Graph - Theoretical Analysis of Supramolecular Fuchsine Acid via Revan Topological Indices

D.C. Gunawardhana[a,d *], K. Moulis[b], K.K.K.R. Perera[c] and G.J. Lanel[d]

[a]Department of Mathematical Sciences, Faculty of Applied Sciences, South Eastern University of Sri Lanka, Sammanthurai 32200
[b]Department of Physical Sciences, Faculty of Applied Sciences, University of Vavuniya, Sri Lanka 43000
[c]Department of Mathematics, Faculty of Science, University of Kelaniya, Sri Lanka 11600
[d]Department of Mathematics, Faculty of Applied Sciences, University of Sri Jayewardenepura, Sri Lanka 10250

[*]rehan@seu.ac.lk

Abstract
Chemical graph theory provides a mathematical framework for modeling molecular structures by representing atoms as vertices and chemical bonds as edges. In Quantitative Structure–Property Relationship (QSPR) and Quantitative Structure–Activity Relationship (QSAR) analyses, degree-based topological indices serve as numerical descriptors that correlate structural features with physicochemical properties. Such indices play a vital role in drug discovery, and molecular modeling. In this work, we investigate the supramolecular sheet structure of fuchsine ($C_{20}H_{19}N_3HCl$), an important magenta dye widely used in microbiological and histological applications. The supramolecular architecture is constructed by arranging fuchsine molecules in an $m \times n$ array, denoted by $F[m,n]$. The associated chemical graph is simple, connected, and finite, comprising $38mn + m + n$ vertices and $42mn$ edges, formulated using Revan degrees of terminal vertices. We derive closed-form expressions for several Revan degree-based topological indices, including the first and second Revan indices (R_1 and R_2), Atomic Bond Connectivity Revan index ($ABCR$), Geometric–Arithmetic Revan index (GAR), first and second hyper Revan indices (HR_1 and HR_2), first and second modified Revan indices (${}^mR_1$ and ${}^mR_2$), and the Forgotten Revan index (FR). This study provides a comprehensive mathematical characterization of the supramolecular fuchsine sheet and enriches the theoretical foundation of Revan-based molecular descriptors.

Keywords: Chemical graph theory; Revan degree; Topological indices; Supramolecular fuchsine; QSPR/QSAR; Mathematical chemistry.

Introduction
Supramolecular chemistry examines the way of creating higher-order structures through molecular interactions. Molecular self-assembly, the primary concept of Supramolecular chemistry is broadly focused on constructing new chemical structures without external direction[1]. Supramolecular structures utilize reversible and fragile non-covalent intermolecular associations, which is a like the linkage of molecules with atoms. This studies the formation of a non-covalently bonded tiny molecule to an extensive molecule. Supramolecular chemistry is widely applied in drug design, biotic procedures, tissue engineering, and as a detector for specific analyses. For instance, Fuchsine $C_{20}H_{19}N_3HCl$ is a supramolecular dye which enhances the effectiveness of a treatment by helping to produce effective drug carriers with minimum side effects. Additionally, Fuchsine is an active agent utilizes for cloth dyeing, bacteria staining and sometimes as a disinfectant. In recent years, Graph Theory has emerged as a crucial mathematical discipline for studying chemical structures. Topological descriptors are employed

Corresponding Author: rehan@seu.ac.lk

to analyse hydrogen-suppressed molecular graphs, in which the edges represent the molecular bonds and the atoms are located at the vertices [1].

A topological index is a numerical value that characterizes the arrangement of connections in a network. Topological indices, which are important in Chemical Graph Theory, have a well-established significance in studying the chemical properties of medications. Pharmaceutical researchers utilize a wide range of topological descriptors. A topological index quantitatively characterizes the shape of a molecule and is employed in the development of qualitative structure-property relationships/qualitative structure-activity relationships (QSPRs/QSARs). Various graph indexes based on degrees have been documented in the literature [2] and have been applied in specific contexts [3, 4]. There exist three distinct categories of topological indices, as mentioned in [5]: degree-based, distance-based, and spectral-based indices. Degree-based indices are widely favoured among the several categories of indices. Topological indices are highly valuable in the process of chemical validation, as well as in QSAR/QSPR research and the development of pharmaceutical drugs. Extensive research has been conducted on degree-based indices, which are believed to be linked to various characteristics of the chemical compounds under investigation. This study aims to provide a more in-depth analysis of molecular descriptors based on degrees.

Harold Wiener introduced the notion of topological indices while studying paraffins, which are alkenes with a high boiling point [6]. The Wiener index, which is the earliest topological index, was introduced by him in 1947. He assigned it the designation of path number. As advancements were made in the field of chemical graph theory, the path number was officially designated as the Wiener index. The Wiener index is extensively studied in chemical graph theory due to its distinctive theoretical features and wide range of applications [5, 7].

In his seminal 1975 paper, Milan Randic [8] introduced the first realistic degree-based topological index. Originally, Randic referred to it as the branching index, but it was later renamed as the connectedness index. Currently, it is widely recognized and referred to as the Randic index, which is precisely defined as,

$R_{-\frac{1}{2}}(G) = \frac{1}{\sqrt{d_G(U)d_G(v)}}$ where $d_G(u)$ and $d_G(v)$ represents the degrees of vertices u and v.

In 1972, I. Gutman and N. Trinanjtic studied dependency of the total π-electron energy of a molecular on its structure [9]. The calculation can be determined by summing the squares of the degrees at each vertex. Subsequently, this total was named the first Zagreb index, and subsequent investigations have been conducted on it [10]. The first Zagreb index is defined as,

$$M_1(G) = \sum_{uv \in E(G)} (d_G(u) + d_G(v))$$

and the second Zagreb index as,

$$M_2(G) = \sum_{uv \in E(G)} (d_G(u) d_G(v))$$

Furthermore, the literature has almost 3000 topological indices. In our study, we focus on Reven degree based topological indices. Let us assume that *G* is a connected graph that is finite, simple, and possesses vertex and edge sets that are represented by the notations $V(G)$ and $E(G)$ respectively. The number of vertices that are next to a vertex u is what determines the degree of that vertex, which is denoted by the expression $d_G(u)$. In the context of the graph *G*, let $\Delta(G)$ represent the degree that is highest among the vertices of *G* while $\delta(G)$ denotes the lowest degree among the vertices of *G*. When considering the graph *G*, the Revan vertex degree of u is defined by the expression $r_G(u) = \Delta(G) + \delta(G) - d_G(u)$. In this particular setting, the symbol uv is used to represent the Revan edge that constitutes the connection between the Revan vertices u and v. In this work, we study on the degree-based Revan topological indices.

Kulli [11] introduced the first and second Revan indices based on the Zagreb indices as follows,

$$R_1(G) = \sum_{uv\in E(G)}(r_G(u) + r_G(v)) \text{ and } R_2(G) = \sum_{uv\in E(G)}(d_G(u)d_G(v)).$$

In [13], Kulli proposed the first and second hyper Revan indices and defined as,

$$HR_1(G) = \sum_{uv\in E(G)}(r_G(u) + r_G(v))^2 \quad HR_2(G) = \sum_{uv\in E(G)}(r_G(u)r_G(v))^2$$

In 2018, the Atomic Bond Connectivity Revan index and Geometric Arithmetic index of a molecular graph *G* [14] were introduced by Kulli and defined as,

$$ABCR(G) = \sum_{uv\in E(G)}\sqrt{\frac{r_G(u) + r_G(v) - 2}{r_G(u)r_G(v)}}$$

$$GAR(G) = \sum_{uv\in E(G)}\frac{2\sqrt{r_G(u)r_G(v)}}{r_G(u)+r_G(v)}$$

The first and second modified Revan indices of a molecular graph *G* were defined by Kulli in [16] as,

$$^{m}R_1(G) = \sum_{uv\in E(G)}\frac{1}{d_G(u)+d_G(v)}$$

$$^{m}R_2(G) = \sum_{uv\in E(G)}\frac{1}{d_G(u)d_G(v)}$$

In 2018, Kulli [15] proposed the forgotten Revan index (F-Revan index) of a molecular graph *G* and formulated as,

$$FR(G) = \sum_{uv\in E(G)}(r_G(u)^2 + r_G(v)^2)$$

Additional information and examples of how Revan indices can be applied can be found in [19-23].

In 2022, A. Ullah et al. conducted a study on the irregular topological indices of the supramolecular sheet of fuchsine acid [24]. In 2024, Kosar et al. [1] calculated and compared various indices, including the Atomic - bond connectivity index, *GA* index, General Randic index, first and second Zagreb index, first hyper Zagreb index, Harmonic index, and Forgotten index. These calculations were performed on the supramolecular structure of Fuchsine acid. This

work aims to examine the Revan topological indices of the supramolecular sheet of fuchsine acid.

Methodology

Within the scope of this study, we take into consideration a supramolecular fuchsine molecule that has the chemical formula $C_{20}H_{19}N_3HCl$. Subsequently, we construct a sheet structure by connecting $a \times b$ units using the unit cell of this compound. We have considered the atoms as vertices and bonds as the edges of this molecular graph. We take this sheet structure as $F[a,b]$. Then we have $38ab + a + b$ vertices and $42ab$ edges. For computing the topological indices, we need to find the edge partitions of $F[a,b]$. Based on Revan degree of Revan end vertices of each Revan edge of $F[a,b]$, three types of edge partitions of Revan edges can be identified.

$$RE_1 = \{uv \in E(F[a,b]) | r(u) = 1, r(v) = 1\}, \qquad |RE_1| = 24ab$$

$$RE_2 = \{uv \in E(F[a,b]) | r(u) = 1, r(v) = 3\}, \qquad |RE_2| = 14ab + 2a + 2b$$

$$RE_3 = \{uv \in E(F[a,b]) | r(u) = 2, r(v) = 1\}, \qquad |RE_3| = 4ab - 2a - 2b$$

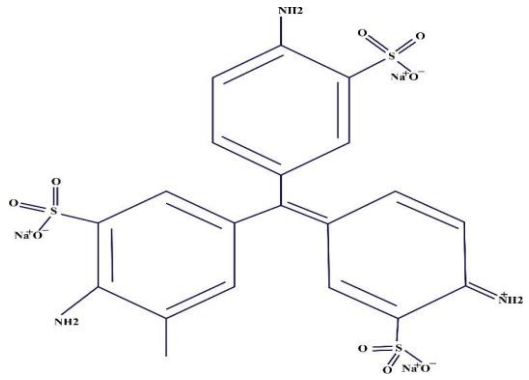

Figure 1: Chemical structure of fuchsine acid

Main Results

Using the edge classification according to the Revan degrees of the end vertices, we now compute the closed-form expressions of the Revan topological indices for the graph $F[a,b]$.

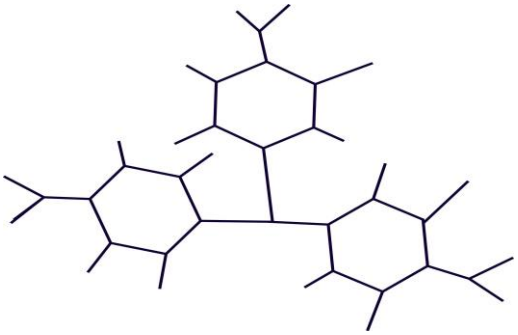

Figure 2: 2D structure of $F[1,1]$

Figure 2 illustrates the 2D structure of $F[1,1]$, which serves as the base unit for the general graph $F[a,b]$. This structure is used to identify the different types of vertices and to determine their corresponding Revan degrees. From this graphical representation, the edges are partitioned according to the Revan degrees of their end vertices. This edge classification enables the computation of the atomic bond connectivity Revan index by systematically counting the number of edges in each partition. The coefficients appearing in the final formula are obtained from this edge partitioning process.

Theorem 1.

The first and second Revan indices of $F[a,b], a,b \geq 1$ *are given by,*

$$R_1(F[a,b]) = 116ab + 2a + 2b$$
$$R_2(F[a,b]) = 74ab + 2a + 2b$$

Proof. The first Revan index is computed as follows.

$$\begin{aligned}
&R_1(F[a,b]) \\
&= \sum_{uv \in E(G)} (r_G(u) + r_G(v)) \\
&= \sum_{uv \in E_1(G)} (r_G(u) + r_G(v)) + \sum_{uv \in E_2(G)} (r_G(u) + r_G(v)) + \sum_{uv \in E_3(G)} (r_G(u) + r_G(v)) \\
&= (24ab)(1+1) + (14ab + 2(a+b))(1+3) + (b(2a-2) + 2a(b-1))(2+1) \\
&= 116ab + 2a + 2b
\end{aligned}$$

The second Revan index of $F[a,b]$ is computed as below.

$$\begin{aligned}
R_2(F[a,b]) &= \sum_{uv \in E(G)} (r_G(u) r_G(v)) \\
&= \sum_{uv \in E_1(G)} (r_G(u) r_G(v)) + \sum_{uv \in E_2(G)} (r_G(u) r_G(v)) + \sum_{uv \in E_3(G)} (r_G(u) r_G(v)) \\
&= (24ab)(1) + (14ab + 2a + 2b)(3) + (b(2a-2) + 2a(b-1))(2) \\
&= 74ab + 2a + 2b
\end{aligned}$$

This is end of the proof.

Theorem 2.

Let $a, b \geq 1$. *The atomic bond connectivity Revan index of* $F[a,b]$ *is given by,*

$$ABCR(F[a,b]) = (14ab + 2a + 2b)\sqrt{\frac{2}{3}} + (14ab - 2a - 2b)\sqrt{\frac{1}{2}}.$$

Proof. By the help of the edge partitions of Revan degree of Revan end vertices of each Revan edge, the atomic bond connectivity Revan index of $F[a,b]$ can be obtained as follows,

$$ABCR(F[a,b]) = \sum_{uv\in E(G)}\sqrt{\frac{r_G(u)+r_G(v)-2}{r_G(u)r_G(v)}}$$

$$= \sum_{uv\in E_1(G)}\sqrt{\frac{r_G(u)+r_G(v)-2}{r_G(u)r_G(v)}} + \sum_{uv\in E_2(G)}\sqrt{\frac{r_G(u)+r_G(v)-2}{r_G(u)r_G(v)}} + \sum_{uv\in E_3(G)}\sqrt{\frac{r_G(u)+r_G(v)-2}{r_G(u)r_G(v)}}$$

$$= (24ab)\sqrt{\frac{1+1-2}{1\times 1}} + \big(14ab+2(a+b)\big)\sqrt{\frac{1+3-2}{1\times 3}} + \big(b(2a-2) + 2a(b-1)\big)\sqrt{\frac{2+1-2}{2\times 1}}$$

$$= (14ab+2a+2b)\sqrt{\frac{2}{3}} + (14ab-2a-2b)\sqrt{\frac{1}{2}}$$

We complete the proof.

The Geometric-arithmetic Revan index of $F[a,b]$ is calculated in the next theorem.

Theorem 3.

Let a, b ≥ 1. *The geometric-arithmetic Revan index of* $F[a,b]$ *is given by,*

$$GAR(G) = 24ab + (14ab+2a+2b)\frac{\sqrt{3}}{2} + (4ab-2a-2b)\frac{2\sqrt{2}}{3}.$$

Proof. The geometric- arithmetic index of $F[a,b]$can be computed as follows,

$$GAR(F[a,b]) = \sum_{uv\in E(G)}\frac{2\sqrt{r_G(u)r_G(v)}}{r_G(u)+r_G(v)}$$

$$= \sum_{uv\in E_1(G)}\frac{2\sqrt{r_G(u)r_G(v)}}{r_G(u)+r_G(v)} + \sum_{uv\in E_2(G)}\frac{2\sqrt{r_G(u)r_G(v)}}{r_G(u)+r_G(v)} + \sum_{uv\in E_3(G)}\frac{2\sqrt{r_G(u)r_G(v)}}{r_G(u)+r_G(v)}$$

$$= (24ab)\frac{2\sqrt{1}}{1+1} + (14ab+2a+2b)\left(\frac{2\sqrt{1\times 3}}{1+3}\right) + 2b(a-1)\frac{2\sqrt{2\times 1}}{2+1}$$

$$= 24ab + (14ab+2a+2b)\frac{\sqrt{3}}{2} + (14ab-2a-2b)\frac{2\sqrt{2}}{3}$$

We complete the proof.

Theorem 4.

Let a, b ≥ 1. *The first and second hyper Revan indices are given by,*

$$HR_1(G) = 356ab + 14a + 14b \text{ and } HR_2(G) = 166ab + 10a + 10b.$$

Proof. Using the edge partitions of Reven degree of end Revan vertices of Revan edges of $F[a,b]$, the first hyper Revan index is can be obtained as follows,

$$HR_1(F[a,b]) = \sum_{uv\in E(G)}(r_G(u)+r_G(v))^2$$

$= \sum_{uv\in E_1(G)}\left(r_G(u)+r_G(v)\right)^2 + \sum_{uv\in E_2(G)}\left(r_G(u)+r_G(v)\right)^2 + \sum_{uv\in E_3(G)}(r_G(u)+r_G(v))^2$

$= \sum_{uv\in E_1(G)}(1)^2 + \sum_{uv\in E_2(G)}(3)^2 + \sum_{uv\in 3(G)}(2)^2$

$= (24ab)(1) + (14ab+2a+2b)(9) + (b(2a-2)+2a(b-1))(4)$

$= 166ab + 10a + 10b.$

Therefore, we complete the proof.

Theorem 5.

Let $a, b \geq 1$. The first and second modified Revan indices are given by,

$${}^{m}R_1(F[a,b]) = RHM_1 = \frac{101ab-a-b}{6}, \text{ and}$$

$${}^{m}R_2(F[a,b]) = RHM_2 = \frac{84ab-4a-4b}{3}.$$

Proof.

$${}^{m}R_1(F[a,b]) = \sum_{uv\in E(G)}\left(\frac{1}{r_G(u)+r_G(v)}\right)$$

$$= \sum_{uv\in E_1(G)}\left(\frac{1}{r_G(u)+r_G(v)}\right) + \sum_{uv\in E_2(G)}\left(\frac{1}{r_G(u)+r_G(v)}\right) + \sum_{uv\in E_3(G)}\left(\frac{1}{r_G(u)+r_G(v)}\right)$$

$$= (24ab)\times\frac{1}{1+1} + (14ab+2a+2b)\times\frac{1}{1+3} + \left(b(2a-2)+2a(b-1)\right)\times\frac{2}{2+1}$$

$$= \frac{101ab-a-b}{6}.$$

$${}^{m}R_2(F[a,b]) = \sum_{uv\in E(G)}\left(\frac{1}{r_G(u)r_G(v)}\right)$$

$$= \sum_{uv\in E_1(G)}\left(\frac{1}{r_G(u)r_G(v)}\right) + \sum_{uv\in E_2(G)}\left(\frac{1}{r_G(u)r_G(v)}\right) + \sum_{uv\in E_3(G)}\left(\frac{1}{r_G(u)r_G(v)}\right)$$

$$= (24ab)\times\frac{1}{1} + (14ab+2a+2b)\times\frac{1}{3} + \left(b(2a-2)+2a(b-1)\right)\times\frac{1}{4}$$

$$= \frac{92ab-a-b}{3}.$$

Theorem 6.

Let $a, b \geq 1$. *The F - Revan index of* $F[a,b]$ *is given by,*

$$FR(F[a,b]) = 208ab + 10a + 10b.$$

Proof.

$$FR(F[a,b]) = \sum_{uv\in E(G)}(r_G(u)^2 + r_G(v)^2)$$

$$= \sum_{uv\in E_1(G)}(r_G(u)^2 + r_G(v)^2) + \sum_{uv\in E_2(G)}(r_G(u)^2 + r_G(v)^2) + \sum_{uv\in E_3(G)}(r_G(u)^2 + r_G(v)^2)$$

$$= (24ab)(1+1) + \big(14ab + 2(a+b)\big)(1+9) + (b(2a-2) + 2a(b-1))(4+1)$$

$$= 208ab + 10a + 10b.$$

Table 1: Comparison of RL indices

G	R_1	R_2	$ABCR$	GAR	HR_1	HR_2	${}^mR_1$	${}^mR_2$	FR
$F[1,1]$	120	78	22	40	384	186	17	30	228
$F[2,2]$	472	304	86	159	1480	704	67	121	872
$F[3,3]$	1056	678	193	358	3288	1554	151	274	1932
$F[4,4]$	1872	1200	343	637	5808	2736	268	488	3408
$F[5,5]$	2920	1870	535	996	9040	4250	419	763	5300
$F[6,6]$	4200	2688	771	1434	12984	6096	604	1100	7608
$F[7,7]$	5712	3654	1048	1953	17640	8274	823	1498	10332
$F[8,8]$	7456	4768	1369	2551	23008	10784	1075	1957	13472
$F[9,9]$	9432	6030	1732	3229	29088	13626	1361	2478	17028
$F[10,10]$	11640	7440	2137	3986	35880	16800	1680	3060	21000

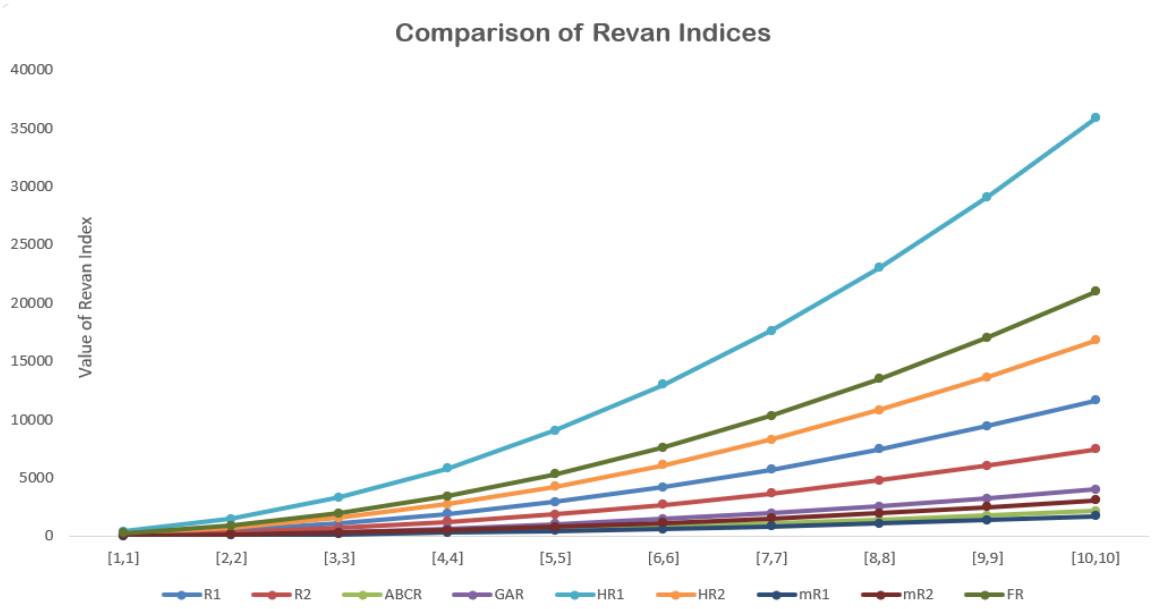

Figure 3: Comparison of Revan indices

Discussion

Table 1 presents a quantitative comparison of the chosen Revan indices for the supramolecular fuchsine acid. Additionally, Figure 3 illustrates a graphical comparison of the Revan indices values provided in Table 1. Furthermore, Figure 3 demonstrates that as the value of $a = b$ increases, the values of Revan topological indices also increase, as seen in Table 1.

Topological indicators are essential for predicting the physicochemical and biological characteristics of chemical compounds from a pharmaceutical and medical perspective. The calculated Revan indices may aid in comprehending molecular stability, reactivity, and structure–activity connections since fuchsine acid and its derivatives are often employed in biological stains and may have antibacterial and diagnostic uses. Without carrying out costly lab tests, these indices may be used in QSAR and QSPR modeling to assess characteristics including bioactivity, toxicity, solubility, and drug–receptor interactions.

Conclusion

This study presents the calculation of the Revan topological indices of the supramolecular graph of Fuchsine acid, which has practical applications in the field of computational chemistry. Furthermore, we have computed various Revan indices, including the first and second Revan indices (R_1 and R_2),the Atomic Bond Connectivity Revan index ($ABCR$), the Geometric-Arithmetic Revan index(GAR), the first and second hyper Revan indices (HR_1 and HR_2), the first and second modified Revan indices ($^mR_1$ and $^mR_2$), and the forgotten Revan index (FR). The numerical comparison of the above mentioned Revan indices is presented in Table 1, while the graphical comparison is provided in Figure 3. The calculated results can be used to determine the eccentricity and spectral based topological indices of supramolecular structures. In future study, we aim to examine the correlation between these Revan index values and the physio-chemical

properties of fuchsine acid. As well as to investigate the importance of these Revan indices compared to other topological indices.

Data availability

All data generated or analysed during this study are included in this manuscript.

Acknowledgements

The authors sincerely thank A. M. F. S. Sino for their dedicated assistance in the typesetting and formatting of this manuscript. Her support greatly contributed to the clarity and professional presentation of this work.

References

[1] Kosar, Z., Zaman, S., Ullah, A., Siddiqui, M. K., & Belay, M. B. (2024). Computation of molecular description of supramolecular Fuchsine model useful in medical data. *Scientific reports*, 14(1), 10933. https://doi.org/10.1038/s41598-024-60284-3

[2] Samanta, S., Pal, M., Pal, A. (2019), Handbook of Research on Advanced Applications of Graph Theory in Modern Society. *Engineering Science Reference (IGI Global)*

[3] Gutman, I. (2003) QSPR/QSAR Studies by Molecular Descriptors By Mircea V. Diudea, *J. Chem. Inf. Comput. Sci.* 43, 1720–1721, https://doi.org/10.1021/ci0104432.

[4] Gutman, I. & Polansky, O. E. (1986). Mathematical concepts in organic chemistry. *Berlin, Heidelberg: Springer Berlin Heidelberg.*

[5] Ahmad, I., Ahmad, M., Hussain, M. & Mahmood, T. (2021). Topological descriptors on some families of graphs. *J. Chem.* 2021(1), 6018893.

[6] Wiener, H. (1947) Structural determination of paraffin boiling points. *J. Am. Chem. Soc.* 69(1), 17–20.

[7] Nikolic´, S. & Trinajstic´, N. (1995). The wiener index: Development and applications. *Croat. Chem. Acta.* 68, 105–129.

[8] Randic, M. (1975) Characterization of molecular branching. *J. Am. Chem. Soc.* 97 (23), 6609-6615. DOI: 10.1021/ja00856a001

[9] Gutman, I. & Trinajstic, N. (1947) Graph theory and molecular orbitals. total ϕ-electron energy of alternant hydrocarbons. *Chem. Phys. Lett.* 17(4), 535–538.

[10] Gutman, I. (2013). Degree-Based Topological Indices. *Croatica Chemica Acta,* 86 (4), 351-361. https://doi.org/10.5562/cca2294

[11] Kulli, V. R. (2017). Revan indices of oxide and honeycomb networks. *Int. J. Math. its Appl.* 5(4E), 663–667

[12] Kulli, V. R. (2017). The Sum Connectivity Revan Index of Silicate and Hexagonal Networks. *Annals Pure Appl. Math.* 14(3), 401–406, DOI: 10.22457/apam. v14n3a6.

[13] Kulli, V. R. (2018). Hyper-Revan Indices and their Polynomials of Silicate Networks. *International Journal of Current Research in Science and Technology*, 4(3), 17–21.

[14] Kulli, V. R. (2018). Connectivity Revan Indices of Chemical Structures in Drugs. 7(5), 11–16, DOI: 10.5281/zenodo.1241360.

[15] Kulli, V. R. (2018) F- Revan Index and F- Revan Polynomial of Some Families of Benzenoid Systems, *Journal of Global Research in Mathematical Archives*. 5(11), 1–6.

[16] Kulli, V. R. (2018). Computing the F-Revan and modified Revan indices of certain nanostructures. *J. Comput. Math. Sci.* 9(10), 1326–1333.

[17] Kulli, V. R. & Gutman, I. (2022). Revan sombor index. *J. Math. Informatics.* 22, 23–27, DOI: 10.22457/jmi. v22a03205.

[18] Gunawardhana, D. C. & Lanel, G. H. J. (2024) Rehan-lanel indices of graphs. *arXiv preprint arXiv:2402.08248*.

[19] Baig, A. Q., Azhar, M. & Gao, W. (2018). Revan and Hyper-Revan indices of Octahedral and Icosahedral Networks. *Appl. Math. Nonlinear Sci.* 3, 33–40, https://doi.org/10.21042/amns.2018.1.00004.

[20] Kulli, V. R.(2022). Revan sombor indices and their exponentials for certain nanotubes. 11(5), 22–31, DOI: 10.5281/zenodo.6623554.

[21] Kulli, V. R. (2017). On the Product Connectivity Revan index of Certain Nanotubes. *J. Comput. Math. Sci.* 8(10), 562–567, DOI: 10.29055/jcms/694.

[22] Ashraf, R. & Akhter, S. (2019) Revan Indices and Revan Polynomials of Silicon Carbide Graphs. *Int. J. Eng. Res.* 8(9), DOI: 10.17577/IJERTV8IS090088.

[23] Kulli, V., Méndez-Bermúdez, J., Rodríguez García, J. M. & Sigarreta, J. M. (2023) Revan Sombor indices: Analytical and statistical study[J]. Mathematical Biosciences and Engineering, 20(2): 1801-1819. doi: 10.3934/mbe.2023082.

[24] Ullah, A., Shamsudin, Zaman, S., Hamraz, A. & Saeedi, G.(2022). Network-based modeling of the molecular topology of fuchsine acid dye with respect to some irregular molecular descriptors. *J. Chem.*, 2022 1–8, DOI: 10.1155/2022/8131276.

Journal of Science-FAS-SEUSL (2025) 06(02) 59-71
ISSN:2738-2184

Rehan-Lanel Indices for Evaluating the Pharmacological Properties of Anti-tuberculosis Drugs

D.C. Gunawardhana[a,d *], K. Moulis[b], K.K.K.R. Perera[c] and G.J. Lanel[d]

[a]Department of Mathematical Sciences, Faculty of Applied Sciences, South Eastern University of Sri Lanka, Sammanthurai 32200
[b]Department of Physical Sciences, Faculty of Applied Sciences, University of Vavuniya, Sri Lanka 43000
[c]Department of Mathematics, Faculty of Science, University of Kelaniya, Sri Lanka 11600
[d]Department of Mathematics, Faculty of Applied Sciences, University of Sri Jayewardenepura, Sri Lanka 10250

[*]rehan@seu.ac.lk

Abstract

Tuberculosis (TB) is still a major health concern across the world, mostly because Mycobacterium tuberculosis may change and become resistant to numerous medicines. Knowing how the molecular structure of anti-TB medications affects their physicochemical qualities might assist make better drugs. We examined twelve frequently utilized anti-tuberculosis medications, including amikacin, bedaquiline, clofazimine, delamanid, ethambutol, and others. We used ideas from chemical graph theory to characterize their molecular architectures. The first to fourth Rehan-Lanel (RL) and Revan Rehan-Lanel (RRL) topological indices were found using these structures. After we figured out these numbers, we looked at how they are connected to other physicochemical qualities, such as the boiling point, melting point, molar volume, molar refraction, polarizability, surface tension, and flash point. The results indicated that some indices are significantly correlated with these qualities. The RL_1 and RRL_1 indices exhibited more robust correlations with factors such as molar volume and boiling point. These findings indicate that RL-based indices may serve as effective descriptors for evaluating certain physicochemical properties of anti-tuberculosis medications and might facilitate early predictions without only depending on comprehensive laboratory data.

Keywords: Chemical graph theory, topological indices, quantitative structure–activity relationship (QSAR), anti-tuberculosis pharmaceuticals, molecular modelling.

Introduction

The presence of *Mycobacterium tuberculosis*, a bacterium that is acknowledged for its ability to affect a variety of organs, including the brain and spine, in addition to the lungs, is the primary reason why Tuberculosis (*TB*) remains a significant global health issue. This disease can lead to severe health consequences. The pathogen's adaptability and persistent nature require the development of innovative strategies in the areas of diagnosis, treatment, and prevention. "Cheminformatics is an interdisciplinary field that combines mathematics, computer science, and chemistry to better understand chemical compounds and their behaviour". It plays an important role in studies involving quantitative structure–activity relationships (*QSAR*) and quantitative structure–property relationships (*QSPR*), which help scientists predict the biological activities and properties of chemical substances. These methods are valuable because they speed up the discovery and development of new therapeutic drugs.

Corresponding Author: rehan@seu.ac.lk

This study explores how molecular graph theory and cheminformatics can be applied to better understand and predict the biological behaviour of compounds related to tuberculosis treatment. The main goal is to identify new compounds with promising anti-tuberculosis potential using *QSAR* and *QSPR* models, thereby contributing to global efforts to combat this persistent disease. "In chemical graph theory, topological indices are widely used because they convert molecular structural information into numerical values that can be analysed mathematically".

Specifically, these indices dive into molecular graphs, where they express topological structures of molecules by numerical descriptors. Topological indices are utilized to examine chemical properties of pharmaceuticals while boosting *QSAR/QSPR*s studies. "Degree-based topological indices, which have been investigated for their linkage between varieties of chemical compound attributes, show a significant demand over different ranges of topological indices" [6, 7, 9].

Harold Wiener came up with the idea of topological indices while investigating paraffins in 1947. This led to the creation of the Wiener index. This index, "which is often called the route number [1, 11], is one of the most researched molecular topological indices in chemical graph theory since it has unique theoretical features and may be used in a lot of different ways". Milan Randic [12] subsequently came up with the first real degree-based topological index. "It was first termed the branching index, then the connectedness index, and today most people call it the Randic index". The first and second Zagreb indices were introduced by I. Gutman and N. Trinajstic in 1972. They are found by adding up the squares of the degrees of the vertices in a graph. Since then, numerous scholars have examined and used these indexes a lot.

In 2009, Vukicevic and Furtula [20] proposed the geometrical-arithmetic index, "adding to the growing list of topological indices. This index provides further insight into the geometric and arithmetic properties of molecular graphs, expanding the toolkit available for analysing molecular structures". In 2015, Furtula and Gutman [4] restudied another index related to the total of the cubed degrees of the vertices of a network, calling it the "Forgotten topological index" or "F-index". In [5], Gunawardhana and Lanel introduced the Rehan-Lanel indices. In this study, we use the first, second, third and fourth Rehan Lanel indices and the first four Revan Rehan-Lanel indices for modelling physical properties of some tuberculosis drugs.

Definition 1.1. Let a graph G consists of a set of vertices $V(G)$ and a set of edges $E(G)$. "The first Rehan-Lanel index, the second Rehan-Lanel index, the third Rehan-Lanel index, and the fourth Rehan-Lanel index" [5] are defined as follows,

i. $RL_1(G) = \sum_{uv \in E(G)} (d_G^2(u) + d_G^2(v) + d_G(u)d_G(v))$
ii. $RL_2(G) = \sum_{uv \in E(G)} (d_G^2(u) + d_G^2(v) - d_G(u)d_G(v))$
iii. $RL_3(G) = \sum_{uv \in E(G)} (d_G(u) - d_G(v) + d_G(u)d_G(v))$
iv. $RL_4(G) = \sum_{uv \in E(G)} |d_G(u) - d_G(v)|\, d_G(u)d_G(v)$

Throughout the paper G is a connected graph that is finite, simple, and has vertex and edge sets denoted by $V(G)$ and $E(G)$. $d_G(u)$ is the degree of a vertex u, and it is determined by the

number of vertices that are adjacent to it. In the context of the graph G, let $\Delta(G)$ indicate the greatest (lowest) degree among the vertices of G correspondingly. In the graph G, the Revan vertex degree of u is defined as the expression $r_G(u) = \Delta(G) + \delta(G) - d_G(u)$. Within this context, the Revan edge that connects the Revan vertices u and v is denoted by the symbol uv.

Kulli introduced the first and second Revan indices based on the Zagreb indices in [14], "more details and applications of Revan indices can be found in [2, 3, 15, 16, 17, 18, 19]". In 2024, Gunawardhana and Lanel proposed the first, second, third and fourth Rehan-Lanel indices [5] of a graph G as follows.

Definition 1.2. The first, second, third, and fourth Revan Rehan-Lanel indices of a graph G are defined by,

i. $RRL_1(G) = \sum_{uv \in E(G)} (r_G^2(u) + r(v) + r(u) r_G(v))$
ii. $RRL_2(G) = \sum_{uv \in E(G)} (r_G^2(u) + r(v) - r(u) r_G(v))$
iii. $RRL_3(G) = \sum_{uv \in E(G)} (r_G(u) - r_G(v) + r_G(u) r_G(v))$
iv. $RRL_4(G) = \sum_{uv \in E(G)} (|r_G(u) - r(v)| \, r_G(u) r_G(v))$

This study investigates the quantitative relationships between the molecular structures of twelve anti-tuberculosis drugs and their physicochemical properties by using the above Rehan Lanel (RL) and Revan RL topological indices. Specifically, the study aims to compute these indices from chemical graphs and assess their effectiveness as descriptors for modelling key physical properties, such as boiling point, melting point, flash point, molar refraction, polarizability, surface tension, and molar volume. Also, we establish predictive models that can provide insights into the physicochemical behaviour of anti-tuberculosis drugs based on their molecular topology.

Methodology

This study utilized chemical graphs to illustrate the molecular structures of twelve anti-TB medications. A point is an atom, while a line is a link between atoms. The medicines were "amikacin, bedaquiline, clofazimine, delamanid, ethambutol, ethionamide, imipenem-cilastatin, isoniazid, levofloxacin, linezolid, moxifloxacin, and p-aminosalicylic acid". When counting the edges, double bonds were counted as two edges. We utilized these chemical graphs to find the first, second, third, and fourth Rehan Lanel (*RL*) indices and the first, second, third, and fourth Revan Rehan–Lanel indices for each medication in a systematic way. We used these eight topological indices as molecular descriptors to generate informed estimations about the compounds' boiling point (*BP*), melting point (*MP*), flash point (*FP*), molar refraction (*MR*), polarizability (*PL*), surface tension (*ST*), and molar volume (*MV*).

To explore the relationship between topological descriptors and physicochemical properties, statistical techniques such as correlation analysis and regression modelling were employed. Correlation coefficients were calculated for each pair of physicochemical property and topological index in order to evaluate the strength of their association. For the regression analysis, the following linear model was applied:

$$P = a + b[TI]$$

where P represents the physical property of the drug, a is a constant, b is the regression coefficient, and TI denotes the topological index. The parameters a and b were estimated using R software, based on seven physicochemical properties and eight degree-based topological indices derived from the molecular structures of twelve drugs. This method allowed the development of linear regression models that link degree-based topological indices with physicochemical properties, providing a quantitative framework for predicting and better understanding the behaviour of anti-tuberculosis drugs.

Results and Discussion

In this section, we present a quantitative framework for predicting physicochemical properties, namely, boiling point (BP), melting point (MP), flash point (FP), molar refraction (MR), polarizability (PL), surface tension (ST), and molar volume (MV). The values of physicochemical properties of twelve tuberculosis medicines are presented in Table 1. These values were extracted from ChemSpider.

Table1: Physical properties of various tuberculosis drugs

Name of medicine	*BP*	*MP*	*FP*	*MR*	*PL*	*ST*	*MV*
Amikacin	981.8	203.5	547.6	134.9	53.5	103.3	363.9
Bedaquiline	702.7	176	378.8	156.2	61.9	52.6	420.1
Clofazimine	566.9	210	296.7	136.2	54	47.1	366.1
Delamanid	653.7	193	349.1	127.7	50.6	50	368
Ethambutol	345.6	89	113.7	58.6	23.2	38.1	207
Ethionamide	247.9	163	103.7	49	19.4	39.8	142
Imipenem	530.2	190	274.5	72.7	28.8	71	183.9
Isoniazid	251.97	172	251	36.9	14.6	57.8	110.2
Levofloxacin	571.5	224	299.4	91.1	36.1	70.3	244
Linezolid	585.5	177	307.9	83	32.9	47.7	259
Moxifloxacin	636	270	338.7	101.8	40.4	60.7	285
p-Aminosalicylic	380.8	145	184.1	39.3	15.6	83.4	102.7

Resource: Physical properties are obtained from ChemSpider.

Regression models for the selected indices:

1. BP = 96.086+0.286 [$RL_1(G)$]
   MP =136.215+0.025 [$RL_1(G)$]
   FP = 39.99+0.1611 [$RL_1(G)$]
   MR = 4.547+0.059 [$RL_1(G)$]
   PL = 1.769+0.024 [$RL_1(G)$]
2. BP = 94.285+0.705 [$RL_2(G)$]
   MP =143.001+0.051 [$RL_2(G)$]
   FP = 77.882+0.338 [$RL_2(G)$]
   MR = 3.871+0.148 [$RL_2(G)$]
   PL = 1.678+0.356 [$RL_2(G)$]
4. BP = 71.035+0.4311 [$RL_4(G)$]
   MP = 346.450+0.425[$RL_4(G)$]
   FP = 59.990+0.461 [$RL_4(G)$]
   MR = 4.547+0.059 [$RL_4(G)$]
   PL = 1.769+0.024 [$RL_4(G)$]
5. BP = 101.699+0.663 [$RRL_1(G)$]
   MP = 148.589+0.054 [$RRL_1(G)$]
   FP = 61.516+0.342[RRL_1(G)]
   MR = 16.238 + 0.113[RRL_1(G)]
   PL = 6.414+0.045[RRL_1(G)]

3. BP = 84.285+0.405 [$RL_3(G)$]
   MP = 103.041+0.451 [$RL_3(G)$]
   FP = 67.852+0.438 [$RL_3(G)$]
   MP = 2.679+0.158 [$RL_3(G)$]
   PL = 1.238+0.460 [$RL_3(G)$]

6. BP = 192.593+0.911 [$RRL_2(G)$]
   MP = 161.817+0.059 [$RRL_2(G)$]
   FP =109.105+0.469 [$RRL_2(G)$]
   MR =19.383 +0.188 [$RRL_2(G)$]
   PL = 7.673+0.007 [$RRL_2(G)$]

7. BP = 123.575+1.782 [$RRL_3(G)$]
   MP =154.506+0.128 [$RRL_3(G)$
   FP = 70.661+0.929 [$RRL_3(G)$]
   MR = 18.725 + 0.309 [$RRL_3(G)$]
   PL = 7.404+0.122 [$RRL_3(G)$]

8. BP = 126.796+1.299 [$RRL_4(G)$]
   MP =155.580+0.091[$RRL_4(G)$]
   FP = 75.861+0.666 [$RRL_4(G)$]
   MR = 17.796 + 0.230 [$RRL_4(G)$]
   PL = 7.036+0.091 [$RRL_4(G)$]

The computed RL indices of each anti-tuberculosis drugs are presented in Table 2.

Table 2: Values of *RL* indices of each anti-tuberculosis medicine

Medicine	RL_1	RL_2	RL_3	RL_4	RRL_1	RRL_2	RRL_3	RRL_4
Amikacin	2294	802	518	716	1348	674	476	636
Bedaquiline	2335	971	579	482	835	771	363	474
Clofazimine	1517	647	357	390	703	342	208	300
Delamanid	2449	1017	603	604	859	478	290	414
Ethambutol	1000	468	192	336	625	345	215	316
Ethionamide	827	345	201	204	347	225	121	164
Imipenem	1276	536	302	384	586	306	208	274
Isoniazid	687	218	184	146	255	137	91	116
Levofloxacin	1752	736	462	462	662	366	232	312
Linezolid	1625	691	381	470	650	366	228	320
Moxifloxacin	2062	852	518	480	757	417	263	360
p-Aminosalicylic	732	280	202	128	282	130	100	118

In Table 3, we present the correlation coefficients between values of nine degree-based Rehan-Lanel topological indices and six physical properties of medicines. The main drawback of our study is the lack of satisfactory correlate findings among degree-based topological index, and the melting point and surface tension of anti-tuberculosis drug. But the correlations values between RL indices and MP are high compared to the correlations between other degree-based indices and MP of these anti-TB drugs. However, the theoretical analysis of our study could strengthen the prediction of anti-tuberculosis medicinal attributes with zero involvement of laboratory experimentation.

Table 3: Correlations of RL indices with physical properties

Topological Index	BP	MP	FP	MR	PL	ST	MV
RL_1	0.8865	0.5547	0.8160	0.8996	0.8997	0.1891	0.9054
RL_2	0.7702	0.4749	0.6735	0.8722	0.8723	-0.0042	0.9047
RL_3	0.8485	0.6106	0.8019	0.8780	0.8781	0.1915	0.8724
RL_4	0.9228	0.4612	0.8245	0.8136	0.8137	0.2787	0.8350
RRL_1	0.9418	0.3629	0.8433	0.8158	0.8160	0.3929	0.8264
RRL_2	0.8376	0.2555	0.7470	0.8771	0.8770	0.1778	0.8840
RRL_3	0.9360	0.3168	0.8464	0.8249	0.8250	0.3892	0.8301
RRL_4	0.9260	0.3040	0.8260	0.8996	0.8997	0.1891	0.9054

Table 4: Statistical parameters for the linear QSPR model for $RL_1(G)$

Physical Property	a	b	r	r^2	F	p	Indicator
BP	96.0863	0.2862	0.8865	0.7636	36.53	≤ 0.05	Significant
MP	125.5309	0.0381	0.5547	0.2423	4.518	≥ 0.05	Not significant
FP	52.3739	0.1518	0.8160	0.6325	19.93	≤ 0.05	Significant
MR	2.4210	0.0570	0.8996	0.7903	42.45	≤ 0.05	Significant
PL	0.9386	0.0226	0.8997	0.7905	42.5	≤ 0.05	Significant
ST	51.5033	0.0056	0.1891	0.0000	0.371	≥ 0.05	Not significant
MV	19.4	0.1519	0.9054	0.8018	45.49	≤ 0.05	Significant

Table 5: Statistical parameters for the linear QSPR model for $RL_2(G)$

Physical Property	a	b	r	r^2	F	p	Indicator
BP	133.6127	0.6427	0.7702	0.6274	19.52	≤ 0.05	Significant
MP	129.55808	0.08698	0.4749	0.1988	3.729	≥ 0.05	Not significant
FP	84.813	0.321	0.6735	0.4471	9.894	≥ 0.05	Significant
MR	3.7098	0.1379	0.8722	0.7693	37.68	≤ 0.05	Significant
PL	1.45323	0.05468	0.8723	0.7693	37.69	≤ 0.05	Significant
ST	58.2589	0.0030	-0.0042	-0.09812	0.01712	≥ 0.05	Not Significant
MV	19.8264	0.3721	0.9047	0.8036	46	≤ 0.05	Significant

Table 6: Statistical parameters for the linear QSPR model for $RL_3(G)$

Physical Property	a	b	r	r^2	F	p	Indicator
BP	120.321	1.123	0.8485	0.6907	25.57	≤ 0.05	Significant
MP	120.4017	0.1717	0.6106	0.3147	6.05	≥ 0.05	Significant
FP	59.2430	0.6116	0.8019	0.6074	18.02	≤ 0.05	Significant
MR	5.5945	0.2282	0.8780	0.7479	33.63	≤ 0.05	Significant
PL	2.19579	0.09051	0.8781	0.7481	33.68	≤ 0.05	Significant
ST	51.50008	0.02319	0.1915	-0.05965	0.3808	≥ 0.05	Not significant
MV	30.7206	0.6001	0.8724	0.7372	31.86	≤ 0.05	Significant

Table 7: Statistical parameters for the linear QSPR model for $RL_4(G)$

Physical Property	a	b	r	r^2	F	p	Indicator
BP	102.51	1.09	0.9228	0.8381	57.95	≤ 0.05	Significant
MP	138.2794	0.1152	0.4612	0.135	2.716	≥ 0.05	Not Significant
FP	62.8549	0.5604	0.8245	0.6478	21.23	≤ 0.05	Significant
MR	15.1976	0.1885	0.8136	0.6282	19.59	≤ 0.05	Significant
PL	6.00529	0.07475	0.8137	0.6284	19.6	≤ 0.05	Significant
ST	48.10429	0.03008	0.2787	-0.01454	0.8424	≥ 0.05	Not significant
MV	49.4826	0.5119	0.8350	0.6669	23.03	≤ 0.05	Significant

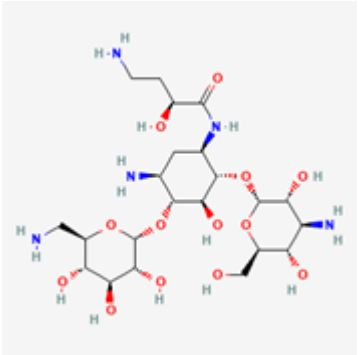

(a) Amikacin

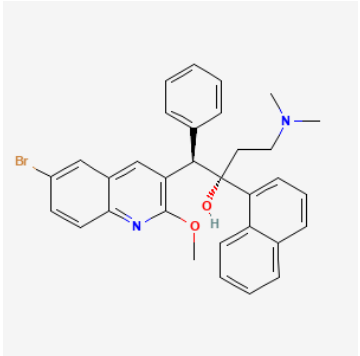

(b) Bedaquiline

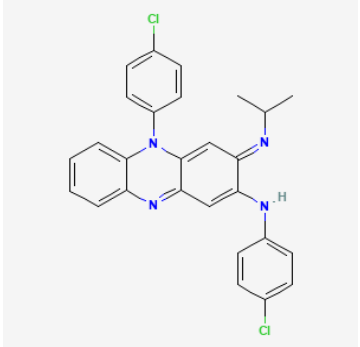

(c) Clofazimine

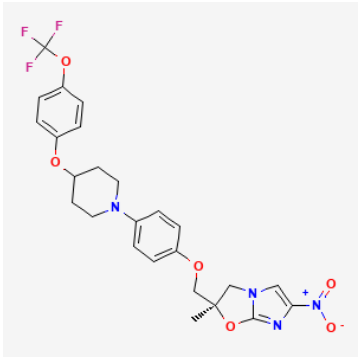

(d) Delamanid

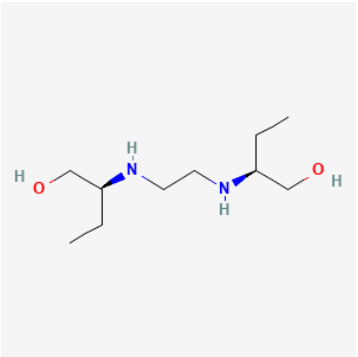

(e) Ethambutol

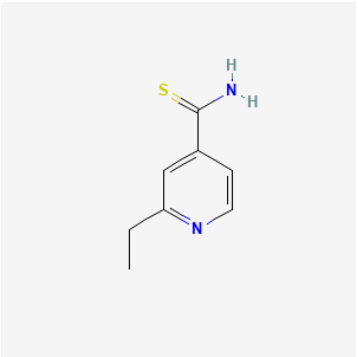

(f) Ethionamide

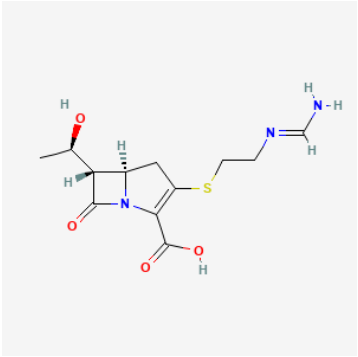

(g) Imipenem

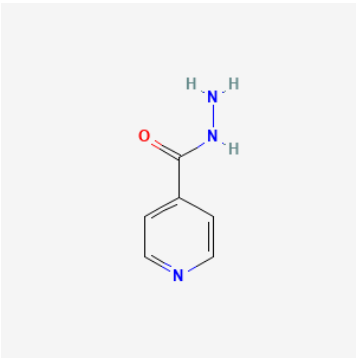

(h) Isoniazid

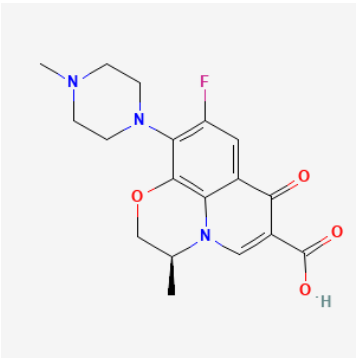

(i) Levofloxacin

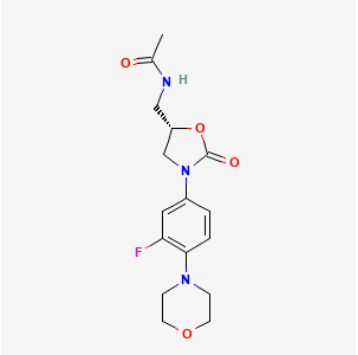

(j) Linezolid

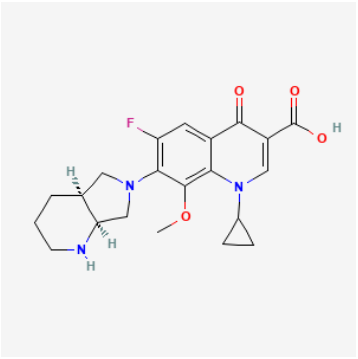

(k) Moxifloxacin

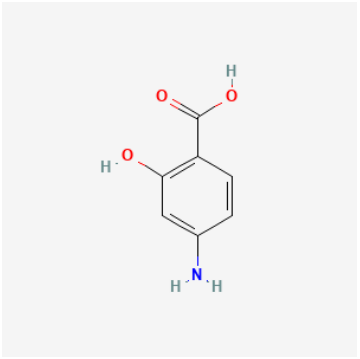

(l) P-Aminosalicyclic

Figure 1: Chemical Structures of Medicines
Resource: Chemical structures are taken from PubChem

Table 8: Statistical parameters for the linear QSPR model for $RRL_1(G)$

Physical Property	*a*	*b*	*r*	r^2	*F*	*p*	Indicator
BP	101.699	0.663	0.9418	0.8733	76.79	≤ 0.05	Significant
MP	148.5894	0.0543	0.3629	0.04638	1.535	≥ 0.05	Not significant
FP	61.5156	0.3423	0.8433	0.6822	24.61	≤ 0.05	Significant
MR	16.2382	0.1129	0.8158	0.6321	19.9	≤ 0.05	Significant
PL	6.41391	0.04476	0.8160	0.6324	19.93	≤ 0.05	Significant

ST	43.45153	0.02532	0.3929	0.06982	1.826	≥ 0.05	Not significant
MV	54.8992	0.3026	0.8264	0.6513	21.55	≤ 0.05	Significant

Table 9: Statistical parameters for the linear QSPR model for $RRL_2(G)$

Physical Property	a	b	r	r^2	F	p	Indicator
BP	192.5930	0.9114	0.8376	0.6694	23.28	≥ 0.05	Significant
MP	161.8171	0.0594	0.2555	-0.0267	0.714	≥ 0.05	Not significant
FP	109.1046	0.4687	0.7470	0.5138	12.62	≥ 0.05	Significant
MR	19.3832	0.1876	0.8771	0.7463	33.35	≥ 0.05	Significant
PL	7.6728	0.0074	0.8770	0.746	33.31	≥ 0.05	Significant
ST	53.4127	0.01772	0.1778	-0.0652	0.3266	≥ 0.05	Not significant
MV	64.3124	0.5004	0.8840	0.7597	35.77	≤ 0.05	significant

Table 10: Statistical parameters for the linear QSPR model for $RRL_3(G)$

Physical Property	a	b	r	r^2	F	p	Indicator
BP	123.575	1.782	0.9360	0.8611	69.21	≤ 0.05	Significant
MP	154.5057	0.1282	0.3168	0.0116	1.129	≥ 0.05	Not significant
FP	70.661	0.9293	0.8464	0.688	25.26	≤ 0.05	Significant
MR	18.7251	0.3087	0.8249	0.6485	21.29	≤ 0.05	Significant
PL	7.4038	0.1224	0.8250	0.6487	21.31	≤ 0.05	Significant
ST	44.3367	0.0679	0.3892	0.0667	1.786	≥ 0.05	Not significant
MV	62.8455	0.8221	0.8301	0.658	22.17	≤ 0.05	Significant

Table 11: Statistical parameters for the linear QSPR model for $RRL_4(G)$

Physical Property	a	b	r	r^2	F	p	Indicator
BP	126.796	1.299	0.9260	0.8407	59.07	≤ 0.05	Significant
MP	155.5807	0.0908	0.3040	0.0031	1.034	≥ 0.05	Not significant
FP	75.8613	0.6664	0.8260	0.6462	21.09	≤ 0.05	Significant
MR	17.7958	0.2297	0.8996	0.6634	22.68	≤ 0.05	Significant
PL	7.03622	0.0911	0.8997	0.6636	22.7	≤ 0.05	Significant
ST	46.7676	0.0422	0.1891	0.0186	1.209	≥ 0.05	Not significant
MV	57.6812	0.6203	0.9054	0.658	22.17	≤ 0.05	Significant

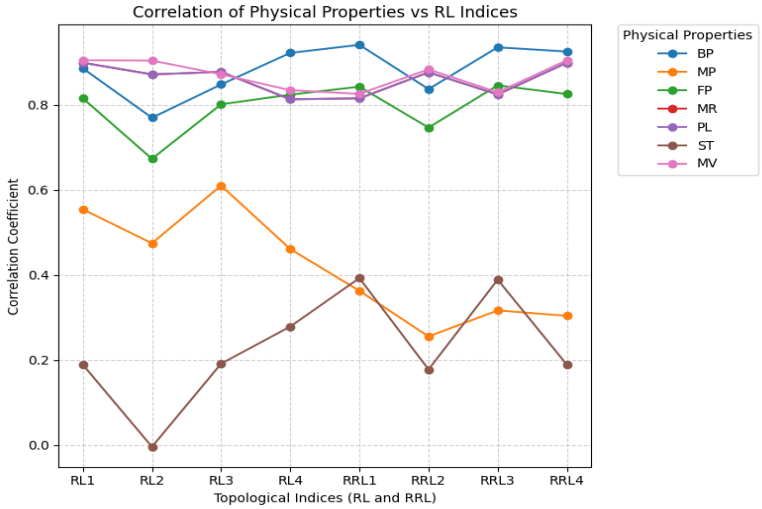

Figure 2: Correlation of Physical properties and topological indices

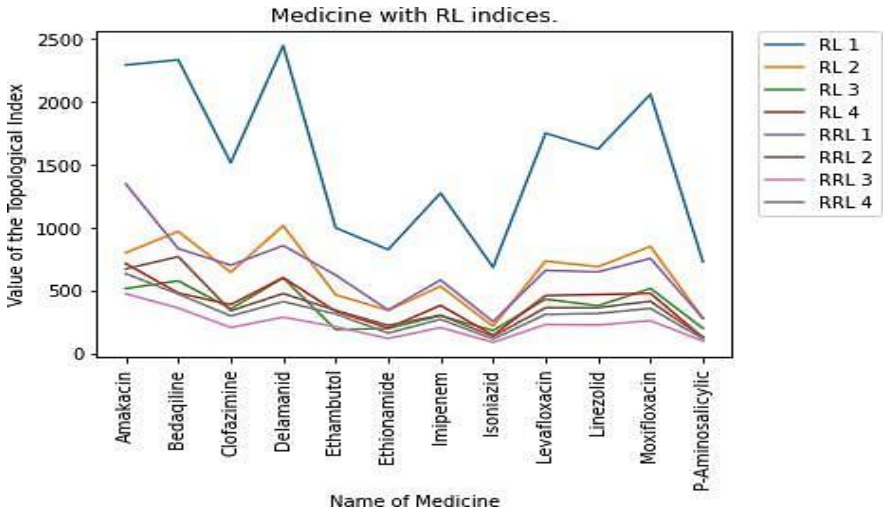

Figure 3: Comparison of topological indices with medicines

This part has been about figuring out the Regression parameters. $N, a, b, and\ r$ stand for the sample size, the constant or intercept of y, the slope, and the correlation coefficient, respectively. r^2 shows how much the response variable changes, as shown by the linear model. The $p-$value of each term tests the null hypothesis, which says that the coefficients are all zero. On the other hand, a larger (not important) p-value means that changes in the predictor are not connected to changes in the responder. Let's say we're running a test where the null hypothesis says that all the regression coefficients are equal to zero. This test first looks at the models without any explanatory variables. Then, it looks at how the model improves with additive coefficients by giving a F value as the result. Somehow, in this scenario, the model is unable to provide precise predictions. The Tables 4-11 shows the statistical parameters of linear QSPR models for a range of topological indices. Each model gives a significant result, where the p value is lower or equal to the significance level (0.05).

Conclusion

Tuberculosis (*TB*) is a bacterial disease caused by the Mycobacterium tuberculosis germs. This makes the lungs perform less properly and puts people's lives at danger by spreading to other parts of the body, such the brain and spine.

A molecular descriptor is a math formula that works on any graph that explains how a molecule is built. One number, in particular, stands for a chemical structure. Graph theory calls this number a topological descriptor, which may be linked to a molecular element to make a molecular index, notably a topological index (*TI).* The topology of the graph is used to make a topology index, which is what happens when a molecular graph is changed. We might be able to learn more about the physical and chemical characteristics of molecules by finding these indices. When you calculate these topological indices, you may see arithmetic numbers and learn more about some of the molecule's physical and chemical features. You transform a molecular graph into a number that shows how the graph is put up to generate a topological index. Topological indices are particularly significant in mathematical chemistry, especially when it comes to quantitative structure-activity relationships (*QSAR*) and quantitative structure-property relationships (*QSPR*).

Upon examining correlation coefficients horizontally for physical properties under consideration, we see that RL_1 (*G*) gives highest correlation coefficient for MV ($r = 0.9054$), MR ($r = 0.8996$) and polarizability ($r = 0.8997$). RL_2 (*G*) gives the highest correlation coefficient for MV ($r = 0.9054$). RL_3 (G) gives the highest correlation coefficient for the MR (r = 0.8780), polarizability ($r = 0.8781$). RL_4 (*G*) gives the highest correlation coefficient for BP ($r = 0.9228$). RRL_1 (*G)* gives the highest correlation coefficient for BP ($r = 0.9418$). RRL_2 (*G*) gives the highest correlation coefficient for MR ($r = 0.8771$) and polarizability ($r = 0.8770$). RRL_3 (*G*) gives the highest correlation coefficient for BP ($r = 0.9360$). RRL_4 (*G*) gives highest correlation coefficient for BP ($r = 0.9260$) and MV($r = 0.9054$). When we look vertically, BP has also good correlation with RRL_1 (G) i.e. $r = 0.9418$), and RRL_3 (*G*) ($r = 0.9360$) respectively. FP has good correlation with RRL_4 (*G*) i.e. $r = 0.8464$. MR has also good correlation with RL_1 (*G*) and RL_1 (*G*), i.e., $r = 0.8996$ both. Polarizability has also good correlation with $RL_1(G)$ and $RRL_4(G)$ i.e., ($r = 0.8997$) for both. MV has also good correlation with $RL_1(G)$, $RL_2(G)$ and RRL_4 (*G*), i.e., $r = 0.9054, 0.9047$ and $r = 0.9054$ respectively.

Research indicates that this theoretical approach may aid chemists and professionals in the pharmaceutical industry in forecasting the characteristics of anti-tuberculosis drugs without empirical testing. It is possible that different combinations of these drugs might be used to treat different diseases, depending on the range of the topological indices obtained in this study. We have calculated the correlation coefficient for several topological indicators in this study. This discovery will aid chemists in designing innovative pharmaceuticals by amalgamating substances that have a strong positive correlation.

More research into the link between the molecular structure of pharmaceuticals and their physical qualities might help us figure out how well new treatments will work and how safe they will be. Researchers may be able to learn more about how drugs could behave by looking at how new topological indices are connected to other physicochemical qualities including solubility, bioavailability, and stability. This can also assist find good drug candidates early on in development, which might save time and money in drug research. Also, numerical methods may be used to find the optimum link between a topological index and the physical characteristic it describes. These kinds of methods could assist make predictions about physicochemical characteristics better without having to depend just on experimental data.

Acknowledgements

The authors sincerely thank Ms. A. M. F. S. Sino for their dedicated assistance in the typesetting and formatting of this manuscript. Her support greatly contributed to the clarity and professional presentation of this work.

References

[1] Ahmad, I., Ahmad Chaudhry, M., Hussain, M., & Mahmood, T. (2021). Topological Descriptors on Some Families of Graphs. *Journal of Chemistry*, *2021*, 1–12. https://doi.org/10.1155/2021/6018893

[2] Ashraf, R. & Akhter, S. (2019), Revan Indices and Revan Polynomials of Silicon Carbide Graphs, *International Journal Of Engineering Research & Technology (IJERT)*, 08(09).

[3] Baig, A.Q., Naeem, M. & Gao, W.(2018) Revan and hyper-Revan indices of Octahedral and icosahedral networks. *Appl. Math. Nonlinear Sci.* 3, 33–40, https://doi.org/10.21042/amns.2018.1.00004.

[4] Furtula, B. & Gutman, I. (2015), A forgotten topological index, *Journal of Mathematical Chemistry*, 53, pp. 1184–1190.

[5] Gunawardhana, D.C. & Lanel, G.H.J., (2024), Rehan-Lanel Indices of Graphs, *arXiv* preprint arXiv:2402.08248.

[6] Gutman, I. & Polansky, O. (1986). *Mathematical Concepts in Organic Chemistry*. Berlin, Boston: De Gruyter. https://doi.org/10.1515/9783112570180

[7] Gutman, I., (2003), QSPR/QSAR Studies by Molecular Descriptors by Mircea V. Diudea, *Journal of Chemical Information and Computer Sciences*, **43**(5):1720-1721.

[8] Gutman, I., (2013), Degree-based topological indices, *Croatica Chemica Acta*, **86**(4), pp. 351-361.

[9] Pal, M., Samantha, S., & Pal, A. (2019), Handbook of Research on Advanced Applications of Graph Theory in Modern Society, *IGI Global*.

[10] Wiener, H., (1947), Structural determination of paraffin boiling points, *Journal of the American Chemical Society*, **69**(1), pp. 17-20.

[11] Nikoli´c, S. & Trinajsti´c, N., (1995), The Wiener index: Development and applications, *Croatica Chemica Acta*, **68**(1), pp. 105-129.

[12] Randic, M., (1975), Characterization of molecular branching, *Journal of the American Chemical Society*, **97**(23), pp. 6609-6615.

[13] Khalifeh, M.H., Yousefi-Azari, H. & Ashrafi, A.R., (2008), The hyper-Wiener index of graph operations. Comput. Math. Appl., **56**(5), pp. 0898-1221.

[14] Kulli, V. R. (2017). Revan Indices of Oxide and Honeycomb Networks. *International Journal of Mathematics And Its Applications*, *5*(4 - E), 663–667. Retrieved from https://ijmaa.in/index.php/ijmaa/article/view/1324

[15] Kulli, V.R., (2017), On the Product Connectivity Revan Index of Certain Nanotubes, *Journal of Computer and Mathematical Sciences*. 08. pp. 562-567

[16] Kulli, V.R., (2018), F-Revan Index and F-Revan Polynomial of Some Families of Benzenoid Systems, *Journal of Global Research in Mathematical Archives*, 5(11).

[17] Kulli, V.R. & Gutman, I., (2022), Revan Sombor Index, *Journal of Mathematics and Informatics*, 22, pp. 23-27.

[18] Kulli, V.R., (2022), Revan Sombor Indices and Their Exponentials For Certain Nanotubes, *International Journal of Engineering Sciences and Research Technology*., 11, pp. 22-31.

[19] Kulli, V. R., Méndez-Bermúdez, J. A., Rodríguez, J. M., & Sigarreta, J. M. (2023). Revan Sombor indices: Analytical and statistical study. *Mathematical biosciences and engineering : MBE*, *20*(2), 1801–1819. https://doi.org/10.3934/mbe.2023082

[20] Vukicevic, D. & Furtula, B. (2009) Topological Index Based on the Ratios of Geometrical and Arithmetical Means of End-Vertex Degrees of Edges. *Journal of Mathematical Chemistry*, **46**, 1369-1376. http://dx.doi.org/10.1007/s10910-009-9520-x

Journal of Science-FAS-SEUSL (2025) 06(02) 72-76
ISSN:2738-2184

A New Approach to Determine the Optimal Solution for Transportation Problems

M.B.F.I. Mushfiqa* and R. Yogeswary

Department of Mathematical Sciences, Faculty of Applied Sciences, South Eastern University of Sri Lanka, Sammanthurai 32200

*mushfybazeer48@gmail.com

Abstract

One particular kind of linear programming problem is the transportation problem. It aims to reduce the cost of transporting goods from many supply points to different demand areas. Optimal solutions are typically found using techniques like the Stepping Stone method and the Modified Distribution (MODI) method. However, before optimality is examined, both of these approaches require the identification of an initial basic feasible solution. Conventional approaches can be time-consuming because they require iterations for both the initial basic feasible solution and the optimality evaluation. This study presents a novel approach to the transportation problem that does not require an initial basic feasible solution in order to identify the optimal solution. Both balanced and unbalanced transportation problems can be solved using this technique. The proposed method is appropriate for large transportation systems since it lowers computational complexity and provides a few iterations to optimality. Using numerical examples, we tested the proposed approach and compared the outcomes with the optimal solution obtained using the Vogel Approximation Method (VAM) and the MODI method. We applied MODI for the optimality check and VAM for the initial basic feasible solution. The outcomes were also compared to the optimal solution determined with the "TORA" software. Every strategy produces the same ideal result, confirming the precision and effectiveness of the suggested approach. This approach requires a straightforward mathematical and logical computation that is simpler to learn and apply.

Keywords: MODI method, TORA software, Transportation Problem.

Introduction

One of the initial and most significant uses of linear programming problems is the transportation problem. It focuses on the most economical method of meeting supply and demand restrictions while distributing a product from several suppliers (sources) to multiple consumers (destinations). It is assumed that there are balanced and unbalanced states in transportation problems. The primary objective of the problem is to determine an optimal schedule for shipping the commodity while satisfying demand at each destination. The modified Distribution (MODI) and Stepping Stone methods are the well-known traditional methods for finding the optimal solution to a transportation problem. (Soomro et al.,(2015)).

However, both of these methods to find optimal solutions require the determination of an initial basic feasible solution by using any of the available methods, such as “Northwest Corner”, “Least cost method”, and “Vogel’s approximation method” before the optimality is checked. This two-step process demands a higher number of iterations. So, there is a need for a more direct approach that bypasses the IBFS step without compromising accuracy. This research aims

Corresponding Author: mushfybazeer48@gmail.com

to provide a new approach that directly finds the optimal solution for transportation problems without requiring the initial basic feasible solution and with fewer iterations. Additional objectives are: to introduce a simple method, to minimize time, computational complexity, and effort in solving problems, to handle large transportation networks effectively, and to ensure the applicability to real-world transportation problems.

This research is significant as it offers a novel approach to solving transportation problems that reduces the computational load and the number of iterations required to reach the optimal solution. The proposed method's ability to deliver results more easily makes it particularly relevant in today's fast-paced, data-driven decision-making environments. Through this research, a more streamlined solution to transportation problems is introduced, with the potential to be adopted in real-world applications, offering both time and cost savings.

Formulation of the Problem:

Assume that there are m sources and n destinations. Let cij be the cost of moving one unit of commodity from source i to destination j. Let ai be the number of supply units offered at source i and bj be the number of demand units needed at destination j. If xij ($x_{ij} \geq 0$) is the number of units transported from source i to destination j. (Shaikh et al., (2018)).

$\sum_{j=1}^{n} x_{ij} \leq a_i$, (i=1,2,……,m), (Supply Constraints).
$\sum_{i=1}^{m} x_{ij} \geq b_j$, (j=1,2,……,n), (Demand Constraints).
$x_{ij} \geq 0$, (i=1,2,……..,m; j=1,2,… n)

Minimize $Z=\sum_{i=1}^{m} \sum_{j=1}^{n} c_{ij} x_i$

Methodology

This method is applicable to both balanced and unbalanced transportation problems. Step

1: Construct the transportation table from the given transportation problem.

Step 2: Cross out the row minimum in each row. If there are multiple minimums in a row, cross out all of them.

Step 3: Check whether each column contains at least one of the crossed row minimums. If there are columns that do not contain any of the crossed row minimums, from the entries of such columns, subtract their corresponding crossed row minimum and cross out the column entry that has the minimum subtracted value. If some column entries have equal minimum subtracted values, cross out all of them.

Step 4: Select the first crossed entry (row-wise). Suppose $(i,j)^{th}$ crossed entry is selected, count the total number of crossed entries in the i^{th} row and j^{th} column excluding $(i,j)^{th}$ crossed entry. Continue it for all crossed entries.

Step 5: Choose a crossed entry with the minimum count from Step 4 and allocate as much as possible amount to that cell. If a tie occurs, choose a $(k,l)^{th}$ crossed entry breaking the tie such that the total sum of all the elements in k^{th} row and l^{th} column is maximum and allocate as much as possible amount.

Step 6: After performing step 5, delete the satisfied row or column and adjust the supply or demand.

Step 7: Check whether the resultant table contains at least one crossed entry in each row and each column. If not, repeat step 2 to step 7, Otherwise repeat step 4 to step 7 until all the supplies and demands are satisfied.

Results and Discussion

Numerical Example (Shenoy, G.V., 1998. Linear Programming Methods and Applications. Page no:155-156, Problem 17) (UNBALANCED)

	D1	D2	D3	Supply
S1	20	10	40	200
S2	10	20	30	300
S3	10	10	20	100
Demand	100	100	200	

By using Vogel Approximation and Modified Distribution Method to solve:

- Finding Initial Basic Feasible Solution by Using Vogel Approximation

Method After 4 iterations, the Initial Basic Feasible Solution is

	D1	D2	D3	D4	Supply
S1	20	[100] 10	[100] 40	0	200
S2	[100] 10	20	30	[200] 0	300
S3	10	10	[100] 20	0	100
Demand	100	100	200	200	

TotalTransportation Cost=100*10+100*40+100*10+200*0+100*20=8000

- Optimality Check by using the Modified Distribution

  Method After 3 iterations, the Optimal solution is

	D1	D2	D3	D4	Supply
S1	20	[100] 10	40	[100] 0	200
S2	[100] 10	20	[100] 30	[100] 0	300
S3	10	10	[100] 20	0	100
Demand	100	100	200	200	

Total Transportation Cost= 100*10+100*0+100*10+100*30+100*0+100*20=7000

By using TORA Software to solve:

TRANSPORTATION MODEL OUTPUT SUMMARY

Title: Numerical Example 02
Final Iteration No.: 3
Objective Value (minimum cost) =7000.00

From	To	Amt Shipped	Obj Coeff	Obj Contrib
S1: S1	D2: D2	100	10.00	1000.00
S1: S1	D4: DummyD	100	0.00	0.00
S2: S2	D1: D1	100	10.00	1000.00
S2: S2	D3: D3	100	30.00	3000.00
S2: S2	D4: DummyD	100	0.00	0.00
S3: S3	D3: D3	100	20.00	2000.00

By using Proposed Method to solve:

	D1	D2	D3	D4	Supply
S1	20	100	10	40	0 200 100
S2	10		20	30	0 300
S3	10		10	20	0 100
Demand	100	1	0	200	200

Repeat from Step 4

	D1	D3	D4	Supply
S1	20	40	0	100
S2	10	30	0	300
S3	10	100 20	0	100
Demand	100	200 100	200	

Repeat from Step 2

	D1	D3	D4	Supply
S1	20	40	100 0	100
S2	100 10	100 30	100 0	300
Demand	100	100	200 100	

Total transportation cost= 100*10+100*20+100*0+100*10+100*30+100*0= 7000

The optimal solutions are calculated by using the Vogel and Modi method, TORA software and the proposed method. In the above results, we can observe all the solutions from different methods are same for problems but when solving by using proposed approach, the optimal solution is obtained directly without finding initial basic feasible solution in 3 iterations, while in the conventional method, firstly, there are 4 iterations for finding an initial basic feasible solution and 3 iterations for optimality check. The proposed approach has simple calculations and easier to get the optimal solution.

Also, we need only one algorithm that gives a direct optimal solution when using the proposed method.

Conclusion

In this study, we have presented an innovative approach for finding an optimal solution, and we conclude that this approach provides an optimal solution directly without finding the initial basic feasible solution. By eliminating the step of obtaining an initial basic feasible solution, the proposed method reduces the number of iterations required, making it more efficient and effective than the traditional methods. Also, we claim that the proposed approach reduces iterations even when the initial basic feasible solution is obtained by the most accurate method known as the Vogel approximation method and optimality check is done by the well-known Modi method. One of the attractive features of this proposed method is that it has only very simple arithmetical calculations like addition and subtraction, so that everyone can easily understand and use and that is very helpful for decision-makers who are involved with logistic and supply chain problems in the real world. Also, this approach reduces computational complexity, effort, time to solve problems and is suitable to handle large-scale problems easily. In addition, the ability of the new method to handle both balanced and unbalanced transportation problems without defects in accuracy demonstrates its practical potential in various industries.

Acknowledgment

I would like to express my sincere gratitude to my supervisor, Mrs. Yogeswary Raviraj, Senior Lecturer in Mathematics, Department of Mathematical Sciences, Faculty of Applied Sciences, South Eastern University of Sri Lanka, for providing me full support and invaluable guidance for this research.

I extend my gratitude to Dr. M.H. Haroon, Dean of the Faculty of Applied Sciences and for all the lectures of Faculty of Applied Sciences, South Eastern University of Sri Lanka for their guidance.

I convey my deepest gratitude to my parents and family members for their unwavering support, guidance, love, and understanding throughout my academic journey.

References

Shaikh, M., Shah, S. & Memon, Z., (2018). An improved algorithm to solve transportation problems for optimal solution. *International Journal of Scientific & Engineering Research*, 8(8), pp.1-8.

Shenoy, G.V., (1998). *Linear Programming Methods and Application*. 2nd ed. New Delhi: New Age International (P) Limited, Publishers.

Soomro, S., Junaid, M. & Tularam, G., (2015). Modified Vogel's Approximation Method for Solving. *International Journal of Applied Mathematics*, 5(4), pp.32-42.

Charnes, A. & Cooper, W.W., (1954). The stepping stone method of explaining linear programming calculations in transportation problems. *Management Science*, 1(1), pp.49-69.

Hitchcock, F.L., (1941). The distribution of a product from several sources to numerous localities. *Journal of Mathematics and Physics*, 20, pp.224-230. doi:10.1002/sapm1941201224

Journal of Science-FAS-SEUSL (2025) 06(02) 77-81
ISSN:2738-2184

Approximation for Definite Integrals of Bivariate Functions through Second-Degree Taylor Polynomials

M.S.M. Hisam* and M.A.A.M. Faham

Department of Mathematical Sciences, Faculty of Applied Sciences, South Eastern University of Sri Lanka, Sammanthurai 32200

*mohamedhisam93@gmail.com

Abstract:

In practical applications of Mathematics, numerical methods are extensively utilized across various domains. Numerical integration, a vital component of numerical analysis, involves approximating definite integrals. Obtaining exact results for definite integrals of functions with two variables is often challenging in real-world scenarios. Consequently, computational scientists focus on approximation techniques to mitigate this complexity. Numerous studies exist in the literature addressing this issue. This paper proposes an approach for approximating definite integrals of functions with two variables using second-degree Taylor polynomials to minimize errors. We developed and applied this approximation method to selected known functions and compare the approximated values with exact values of the integrals. Finally, we compared the outcomes of our approach with well-known numerical techniques like tangent plane approximation and Simpson's 1/3 rule. Our findings indicate that proposed method yields superior results compared to the other two approaches considered.

Keywords: definite integrals, numerical integration, functions of two variables, Taylor polynomial approximation

1. Introduction

Numerical integration is a branch of study concerned with determining the approximate numerical value of a definite integral and crucial for computing specified integrals in numerical analysis. The fundamental objective of numerical integration is to compute an approximate solution to a defined integral. This process differs from analytical integration in two key ways: it involves error analysis since numerical integration provides an approximation that may not yield precise results, and it focuses solely on generating a numerical result that approximates the area under a curve. Numerical integration is pivotal across various domains such as mathematics, engineering, physical science, and computer science.

Previous studies have explored various approaches to numerical integration. One of the earliest and most widely used numerical integration techniques is Simpson's rule [1]. Introduced by Thomas Simpson in the 18th century, this method approximates the integral of a function by fitting parabolic arcs to small intervals. However, numerical integration remains a vibrant area of research, with a rich history of development and ongoing innovation. By leveraging a diverse array of methods and techniques, researchers continue to push the boundaries of accuracy, efficiency, and applicability in numerical integration. Recently, Peer [2] delved into tangent plane approximation of definite integrals, while Hisam and Faham [3] derived a formula for line integrals using the second-degree Taylor polynomial. Building upon these foundations, this research extends these methodologies to evaluate definite integrals of functions of two variables.

Corresponding Author: rehan@seu.ac.lk

Consider a surface S represented by the equation $z = f(x, y)$, as illustrated in Figure 1 below. The region R corresponds to the projection of this surface onto the xy-plane. Our objective is to determine the volume of the surface S, which lies above R and below the graph of the positive function f [4].

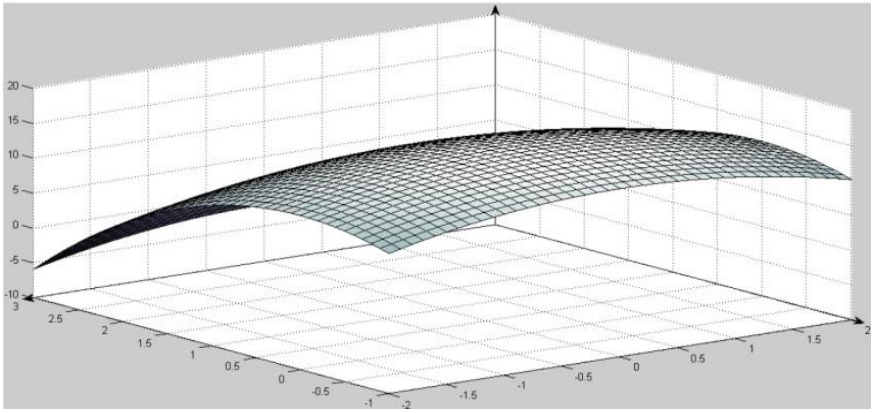

Figure 1: Three-dimensional graph of a surface $f(x, y)$

To compute this volume, we partition the rectangle R into sub-rectangles. We divide the interval $[a, b]$ into m sub-rectangles$[x_i,\ x_{i+1}]; i = 1, 2, \cdots, m$ of equal width $\Delta x = \frac{b-a}{m}$ and divide $[c, d]$ into n sub-rectangles $[y_j,\ y_{j+1}]; j = 1, 2, \cdots, n$ of equal width $\Delta y = \frac{d-c}{n}$.

Then, we compute the volume beneath f by double integrating over the region R as follows: for sample points (x_{ij}^*, y_{ij}^*) in$[x_i,\ x_{i+1}] \times [y_j,\ y_{j+1}]$ and $\Delta A = \Delta x \Delta y$,

$$\iint_R f(x, y)dA = \lim_{m,n\to\infty} \sum_{i=1}^{m} \sum_{j=1}^{n} f(x_{ij}^*, y_{ij}^*)\Delta A \qquad (1)$$

2. Methodology

In this approach, we employ the Taylor polynomial of degree two to approximate the given function $f(x, y)$ of two variables across each sub-rectangle. The crux of this method involves selecting the midpoint of each rectangle as the center for our approximation. By leveraging the second-degree Taylor polynomial, we aim to capture the local behavior of the function $f(x, y)$ within each sub-region, thereby facilitating a more accurate approximation across the entire domain. This strategy enables us to intricately dissect the function's behavior within each sub-rectangle, allowing for a finer-grained approximation that better aligns with the function's curvature and variation. Ultimately, by judiciously choosing the midpoint of each rectangle as the focal point for our approximation, we endeavor to enhance the precision and fidelity of our numerical integration technique.

Now we define an approximation function $P_2(x, y)$ for $f(x, y)$ on the sub-rectangle $[x_i, x_{i+1}] \times [y_j, y_{j+1}]$, by taking $\bar{x}_i = x_0 + \frac{(2i-1)\Delta x}{2}$, $\bar{y}_j = y_0 + \frac{(2j-1)\Delta y}{2}$ as midpoints of $[x_i, x_{i+1}], [y_j, y_{j+1}]$ respctively, as

$$P_2(x,y) = f(\bar{x}_i,\bar{y}_j) + f_x(\bar{x}_i,\bar{y}_j)(x - \bar{x}_i) + f_y(\bar{x}_i,\bar{y}_j)(y - \bar{y}_j) + \frac{f_{xx}(\bar{x}_i,\bar{y}_j)(x - \bar{x}_i)^2}{2} + f_{xy}(\bar{x}_i,\bar{y}_j)(x - \bar{x}_i)(y - \bar{y}_j) + \frac{f_{yy}(\bar{x}_i,\bar{y}_j)(y - \bar{y}_j)^2}{2}. \quad (2)$$

Then, the surface integral of a particular sub-rectangle $[x_i, x_{i+1}] \times [y_j, y_{j+1}]$ is given by,

$$\int_{y_j}^{y_{j+1}} \int_{x_i}^{x_{i+1}} P_2(x,y)\, dxdy. \quad (3)$$

To evaluate the double integral over the region *R*, we sum up all sub-rectangles in *R* and then substituting $\bar{x}_i = \frac{1}{2}(x_{i+1} + x_i)$, $\bar{y}_i = \frac{1}{2}(y_{j+1} + y_j)$, $x_{i+1} - x_i = \Delta x$ and $y_{j+1} - y_j = \Delta y$, in (2), we get equation (3) in the form,

$$\sum_{i=1}^{m}\sum_{j=1}^{n} \int_{y_j}^{y_{j+1}} \int_{x_i}^{x_{i+1}} P_2(x,y)\, dxdy = \sum_{i=1}^{m}\sum_{j=1}^{n} \Delta x \Delta y \left[f(\bar{x}_i,\bar{y}_j) + \frac{1}{24} f_{xx}(\bar{x}_i,\bar{y}_j)(\Delta x)^2 + \frac{1}{24} f_{yy}(\bar{x}_i,\bar{y}_j)(\Delta y)^2 \right].$$

Thus,

$$\int_c^d \int_a^b f(x,y)\, dxdy \approx \sum_{i=1}^{m}\sum_{j=1}^{n} \Delta x \Delta y \left[f(\bar{x}_i,\bar{y}_j) + \frac{1}{24} f_{xx}(\bar{x}_i,\bar{y}_j)(\Delta x)^2 + \frac{1}{24} f_{yy}(\bar{x}_i,\bar{y}_j)(\Delta y)^2 \right] \quad (4)$$

3. Results and Discussion

In this section, we intend to present the outcomes of our novel approach utilizing second-degree Taylor polynomial approximation in comparison to the traditional tangent plane approximation (T.P.A) and Simpson's 1/3 rule. We conduct our analysis by progressively increasing the values of m and n, the number of sub-rectangles, to observe the corresponding improvements in accuracy.

The computations were efficiently carried out using the mathematical software MATLAB, facilitating rapid execution and analysis of our proposed method alongside the established techniques. As m and n increase, each approximation exhibits enhanced accuracy, reflecting the intrinsic relationship between finer partitioning and improved precision in numerical integration. Notably, our proposed second-degree Taylor polynomial approximation showcases a marked reduction in error with increasing numbers of sub-rectangles. This phenomenon indicates the

superior performance of our method, particularly evident when dealing with a smaller number of sub-rectangles. The efficacy of our approach lies in its ability to capture the local behavior of the function more accurately, leading to more precise integral approximations. See table 1 and Table 2 for further details.

Furthermore, our analysis reveals a noteworthy observation regarding Simpson's 1/3 rule: when m and n are chosen as even numbers, this method exhibits diminished performance. This phenomenon underscores the sensitivity of Simpson's 1/3 rule to the choice of intervals, highlighting the importance of considering the parity of m and n for optimal performance.

4. Conslusion

This paper introduces a novel formula for obtaining numerical approximations of definite surface integrals of the form $\iint_R f(x,y)\,dxdy$, where R is a region in the xy-plane bounded by the intervals $[a,b]$ and $[c,d]$. Our proposed approach, imposing the second-degree Taylor polynomial approximation, demonstrates notable advantages over existing methods, particularly in terms of efficiency and accuracy. In the realm of computational scientists, where efficiency is a critical criterion, our proposed formula emerges as a valuable tool. Its ability to deliver more accurate results, especially when compared to certain existing methods. As we continue to advance computational techniques, our proposed formula contributes to the ongoing efforts to refine and optimize numerical integration methodologies, providing a valuable resource for researchers and practitioners across various domains.

5. References

[1] Simpson, T. An Attempt to Determine the Law of Bifacial Inelastic Extension, Philosophical Transactions of the Royal Society, 1748.

[2] Peer, M. (2015). Tangent Line and Tangent Plane Approximations of Definite Integral. Rose-Hulman Undergraduate Mathematics Journal, 16(2), 8.

[3] Hisam, M. S. M, Faham, M. A. A. M. (2019) An approximation technique of definite integral using second order Taylor polynomial. 9th International Symposium (IntSym 2019), South Eastern University of Sri Lanka, Oluvil, 128 – 134.

[4] Stewart, J. (2011). Calculus, Brooks. Cole Publishing Company, 6, 378.

Integral	Exact Value	Rule	For m = n = 2		For m = n = 5		For m = n = 8		For m = n = 11	
			Value	Error	Value	Error	Value	Error	Value	Error
$\int_1^2 \int_0^1 (x^2y + xy^2)\, dydx$	1.6667	T.P.A	1.3125	0.3542	1.6040	0.0627	1.6416	0.0251	1.6533	0.0134
		Simpson	1.6667	3.3333e-05	1.3056	0.3611	1.6667	3.3333e-05	1.4852	0.1815
		Proposed	1.6667	3.3333e-05	1.6667	3.3333e-05	1.6667	3.3333e-05	1.6667	3.3333e-05
$\int_1^{\frac{\pi}{2}} \int_0^{\frac{\pi}{2}} \sin(x+y)\, dydx$	2.0000	T.P.A	2.6588	0.6588	2.1136	0.1136	2.0447	0.0447	2.0237	0.0237
		Simpson	2.0091	0.0091	1.7611	0.2389	2.0000	3.3182e-05	1.8983	0.1017
		Proposed	1.9978	0.0022	1.9999	5.4467e-05	2.0000	8.2784e-06	2.0000	2.3132e-06
$\int_0^1 \int_0^1 e^{(x+y)}\, dydx$	2.9525	T.P.A	2.6309	0.3216	2.8911	0.0614	2.9274	0.0251	2.9390	0.0135
		Simpson	2.9545	0.0020	2.4185	0.5340	2.9525	4.3629e-07	2.6885	0.2640
		Proposed	2.9520	5.1184e-04	2.9525	2.0646e-05	2.9525	9.5582e-06	2.9525	8.1178e-06

Table 1 comparison of tangent plane approximation, Simpson's $\frac{1}{3}$ rule and proposed rule for m = n = 2, m = n = 5, m = n = 8 and m = n = 11.

Integral	Exact Value	Rule	Error			
			For m = n = 25	For m = n = 50	For m = n = 125	For m = n = 200
$\int_1^2 \int_0^1 (x^2y + xy^2)\, dydx$	1.6667	T.P.A	0.0027	6.9600e-04	1.3974e-04	7.4938e-05
		Simpson	0.0836	3.3333e-05	0.0172	3.3333e-05
		Proposed	3.3333e-05	3.3333e-05	3.3333e-05	3.3333e-05
$\int_1^{\frac{\pi}{2}} \int_0^{\frac{\pi}{2}} \sin(x+y)\, dydx$	2.0000	T.P.A	0.0046	0.0012	1.8423e-04	7.1965e-05
		Simpson	0.0432	2.1649e-08	0.0084	8.4659e-11
		Proposed	8.6608e-08	5.4120e-09	1.3871e-10	2.1077e-11
$\int_0^1 \int_0^1 e^{(x+y)}\, dydx$	2.9525	T.P.A	0.0027	6.8864e-04	1.1728e-04	5.0492e-05
		Simpson	0.1208	7.5527e-06	0.0248	7.5580e-06
		Proposed	7.5790e-06	7.5593e-06	7.5580e-06	7.5580e-06

Table 2 comparison of tangent plane approximation, Simpson's $\frac{1}{3}$ rule and proposed rule for m = n = 25, m = n = 50, m = n = 125 and m = n = 20

Journal of Science-FAS-SEUSL (2025) 06(02) 82-96
ISSN:2738-2184

Modeling Sri lanka's Population Growth using Vital Demographic Indicators: A Comparative Analysis of Lagrange Polynomial and Cubic Spline Interpolation Methods

A.N. Wazeetha Mazari[1*], U.L.M. Althaf[l], M.S.M. Farhan[2] and M.A.A.M. Faham[1]

[1]Department of Mathematical Sciences, Faculty of Applied Sciences, South Eastern University of Sri Lanka 32200

[2]Department of Physical Science, Trincomalee Campus, Eastern University, Sri Lanka 31000

[*]mazari@seu.ac.lk

Abstract

This study models and analyzes Sri Lanka's population growth trends using key Demographic Indicators such as Mid-Year Population, Crude Birth Rate, and Crude Death Rate through Lagrange Polynomial Interpolation and Cubic Spline Interpolation techniques. Demographic data spanning the period from 2015 to 2023 were collected from Official National Demographic Statistics. The years were transformed into numerical time indices by assigning 2015 as Year 0. The year 2019 (Year 4) was selected as the interpolation testing year and the year 2024 (Year 9) was used for extrapolation testing year. Predicted values obtained from both interpolation and extrapolation methods were compared with actual recorded data, and accuracy was evaluated using the Absolute Percentage Error measure. The results indicate that cubic spline interpolation provides slightly more accurate estimates than Lagrange polynomial interpolation, primarily due to its piecewise smooth structure and reduced oscillatory behavior. Although both methods performed satisfactorily within the data range, cubic spline interpolation demonstrated greater stability and reliability for extrapolation, whereas Lagrange interpolation showed significant divergence. This study highlights the usefulness of interpolation based mathematical modeling techniques in demographic trend analysis.

Keywords: Demographic Indicators, Lagrange Polynomial, Cubic Spline Interpolation, Population Modeling, MATLAB, Predictive Modeling.

1. Introduction

Analyzing and understanding population growth patterns is crucial for national planning, policy formulation, and forecasting vital demographic trends. Mathematical modeling provides systematic tools for analyzing historical population behavior and estimate missing or future values. Several studies have employed Machine Learning, Predictive Modeling, and Statistical Techniques to analyze demographic and social datasets [1-5].

Focusing on Sri Lanka's population dynamics from the period 2015 to 2023, this study evaluates three key demographic indicators: Mid-Year Population, Crude Birth Rate, and Crude Death Rate using two classical interpolation techniques:

1. Lagrange Polynomial Interpolation
2. Cubic Spline Interpolation

Corresponding Author: mazari@seu.ac.lk

The primary objective is to compare the performance of these techniques in terms of interpolation accuracy within the data range and extrapolation behavior beyond the available data. Since Demographic indicators typically evolve gradually over time, spline-based interpolation is expected to perform well, while Lagrange interpolation might suffer from oscillation behavior as the degree of the polynomial increases. Predictive accuracy is measured using the Absolute Percentage Error formula.

2. Methodology

Lagrange polynomial interpolation and Cubic Spline interpolation were utilized to model Sri Lanka's population growth using selected vital demographic indicators. Annual demographic data for Sri Lanka over a selected historical period were used to construct interpolation models. An intermediate year within the data range was selected to validate interpolation accuracy. Extrapolation was subsequently performed for future years beyond the available data using the same mathematical models.

MATLAB software was used to implement both interpolation methods and to compute predicted population forecasts based on the selected demographic indicators. Error analysis was carried out by comparing the predicted values with actual recorded data using the Absolute Percentage Error Metric.

2.1 Lagrange's' Interpolation Polynomial Method

The Lagrange interpolation polynomial provides a direct method for constructing a single polynomial that passes through all given data points. The polynomial of degree n is defined as

$$P_n(x) = \sum_{i=0}^{n} f(x_i)\, L_i(x)$$

where the Lagrange basis polynomials $L_i(x)$ are given by

$$L_i(x) = \prod_{\substack{j=0 \\ j \neq i}}^{n} \left(\frac{x - x_j}{x_i - x_j} \right), \quad i = 0, 1, 2, \cdots, n.$$

These basis polynomials satisfy the property

$$L_i(x_k) = \delta_{ik} = \begin{cases} 1 & \text{if} \quad i = k \\ 0 & \text{if} \quad i \neq k \end{cases}$$

where δ_{ik} denotes the Kronecker delta.

Although this method ensures exact interpolation at the given data points, it may suffer from oscillatory behavior, particularly when applied to large datasets or used for extrapolation and is quite laborious.

2.2 Cubic Spline Interpolation

Given a set of $n+1$ data points (x_0, y_0), (x_1, y_1),……., (x_n, y_n), cubic spline interpolation constructs a set of piecewise cubic polynomials $S_i(x)$ defined on each subinterval $|x_i, x_i + 1|$ defined by

$$S_i(x) = a_i + b_i(x - x_i) + c_i(x - x_i)^2 + d_i(x - x_i)^3, \;\; i = 0,1,2, \ldots . n - 1.$$

Each spline segment satisfies the interpolation conditions

$$S_i(x_i) = y_i, \qquad S_i(x_i + 1) = y_i + 1,$$

Along with continuity of the first and second derivatives at interior points:

$$S_i'(x_i + 1) = S_{i+1}'(x_i + 1), \quad S_i''(x_i + 1) = S_{i+1}''(x_i + 1).$$

For a natural cubic spline, the second derivatives at the endpoints are set to zero:

$$S_0''(x_0) = 0, \quad S_{n-1}''(x_n) = 0.$$

The coefficients a_i, b_i, c_i and d_i can be efficiently determined by solving a tridiagonal matrix derived from the above continuity conditions:

1. Continuity of Values
2. Continuity of First Derivatives
3. Continuity of Second Derivatives

MATLAB's built-in spline functions were used for implementation. This method reduces oscillatory behavior and preserves local smoothness, making it particularly suitable for demographic data.

2.3 Data Collection

Demographic data for Sri Lanka from 2015-2023 were obtained from publicly available official statistics (Source: Department of Census and Statistics/ Registrar General's Department). The three variables considered were:

1. Mid-Year Population (Millions)
2. Crude Birth Rate (Per 1,000 Population)
3. Crude Death Rate (Per 1,000 Population)

3. Results and Discussion

Figure 1 illustrates Cubic Spline appears smoother and more realistic between data points. It avoids large oscillations and better reflects natural population changes. Lagrange Polynomial shows slight irregularities, especially near the boundaries; a common issue due to Runge's phenomenon in high-degree polynomials. Near the end (last few data points), Lagrange interpolation diverges more, while Cubic Spline stays closer to actual trends.

Table1: Interpolation Results (Testing Year: 2019)

Indicator	Actual value	Predicted value (Lagrange)	Predicted value (Cubic Spline)	Error % (Lagrange)	Error % (Cubic Spline)
Population (Millions)	21.803	21.7757	21.7832	0.125	0.091
Crude birth rate	15.11	14.8781	14.8896	1.535	1.459
Crude death rate	6.48	6.3430	6.3882	2.114	1.417

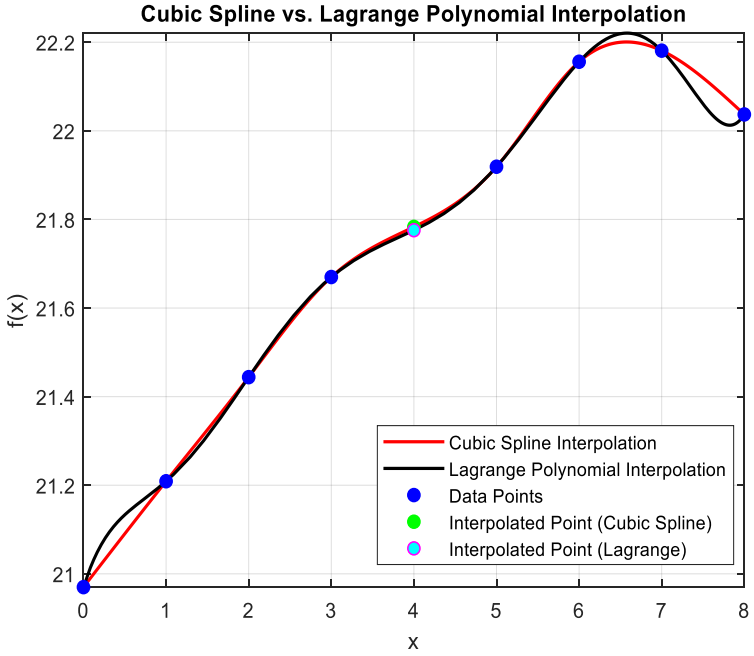

Figure 1: Mid-Year Population

Figure 2 explains how both methods follow a decreasing trend in Birth Rate over time. The Cubic Spline (red) provides a smooth and natural curve with no sharp deviations. The Lagrange Polynomial fits well overall but shows a slight deviation at the start, where it overshoots slightly. The difference between the two interpolations is small here due to the smoother, monotonic nature of the data.

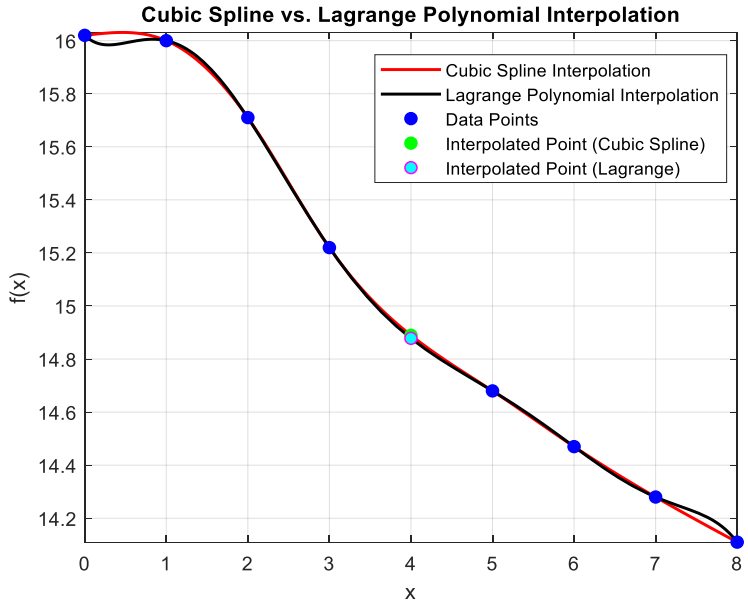

Figure 2: Crude Birth Rate

Figure 3 interprets that Cubic Spline Interpolation is clearly superior for modeling Crude Death Rate, as it avoids the large oscillations seen in the Lagrange method. The Lagrange polynomial is unsuitable here due to its instability over wider intervals with more data points.

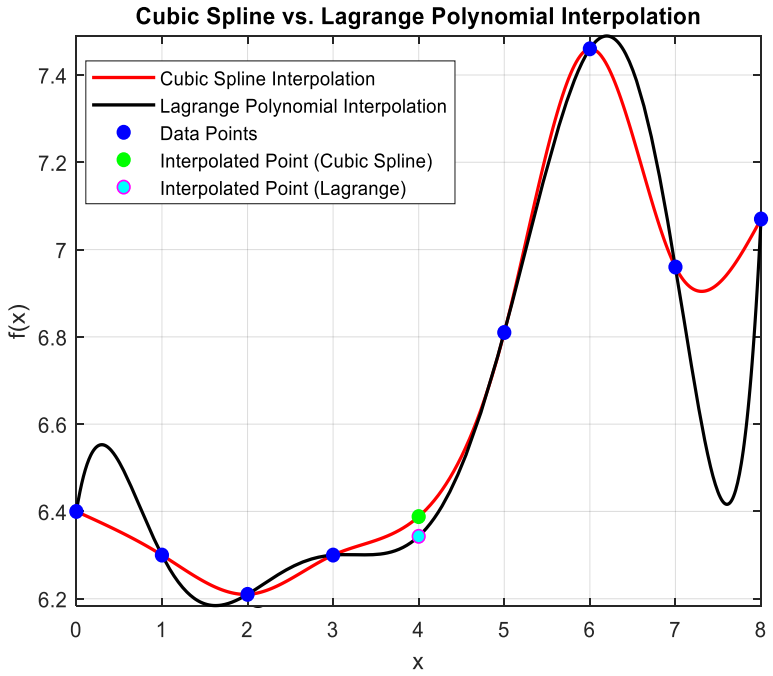

Figure 3: Crude Death Rate

Table 2: Extrapolation Results (Testing Year: 2024)

Indicator	Actual value	Predicted value (Lagrange)	Predicted value (Cubic Spline)	Error % (Lagrange)	Error % (Cubic Spline)
Population (Millions)	21.916	28.098	21.9018	28.208	0.065
Crude Birth Rate	10.1	41.67	14.0978	312.574	39.582
Crude Death Rate	7.8	42.19	10.5342	440.897	35.054

Figure 4-6 demonstrates that Cubic spline interpolation significantly outperforms Lagrange interpolation in extrapolation accuracy. Lagrange interpolation produces extreme overestimations due to polynomial oscillations, rendering it unsuitable for long-term extrapolation. While Population size follows a relatively smooth trend and is well captured by cubic splines rate-based indicators such as Birth and Death Rates exhibit higher variability resulting in larger extrapolation errors for both methods.

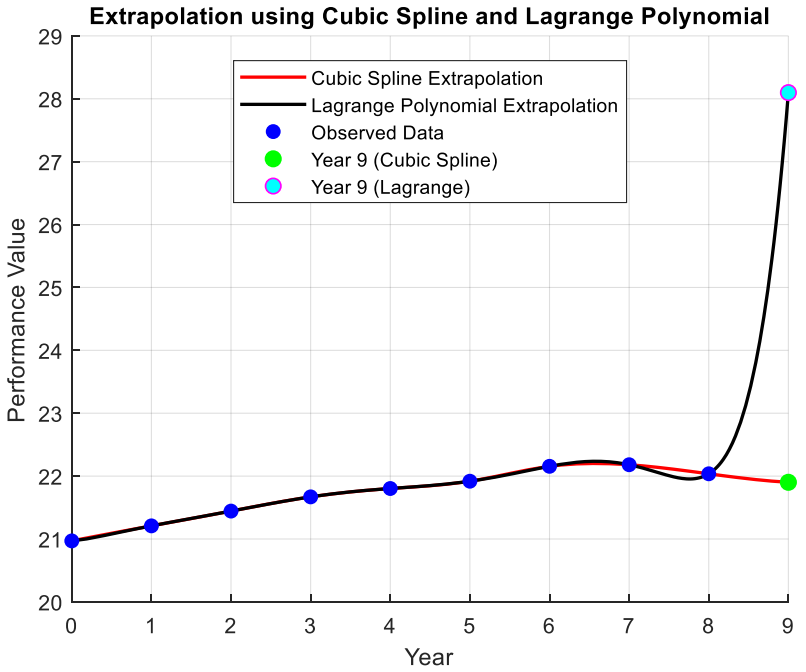

Figure 4: Mid-Year Population

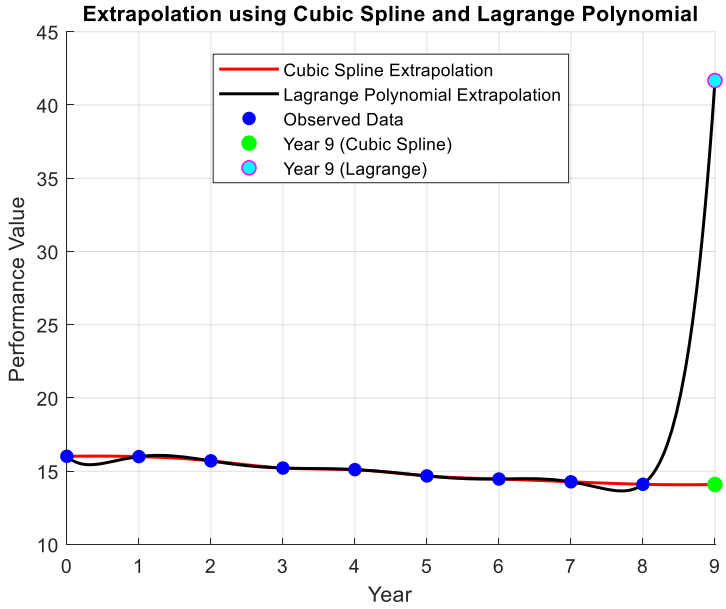

Figure 5: Crude Birth Rate

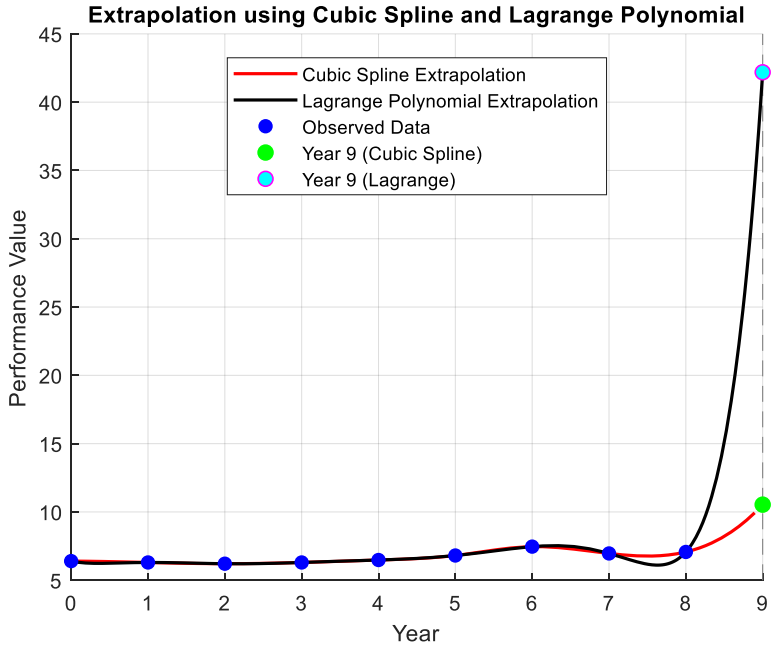

Figure 6: Crude Death Rate

4. Conclusion

This study analyzed and examined Sri Lanka's population growth using Lagrange polynomial and cubic spline interpolation methods applied to demographic data from 2015 to 2023. The results for the testing year 2019 indicate that cubic spline interpolation provides more accurate predictions with lower error percentages compared to the Lagrange method. Although Lagrange interpolation performs reasonably well within the data range, it suffers from inherent limitations due to oscillations issues associated with high-degree polynomials. Both techniques remain stable within the selected interval; however, extrapolation to the year 2024 indicates that cubic spline interpolation is more robust and reliable for demographic forecasting.

Nevertheless, caution is required when extrapolating rate-based indicators, as their natural variability can diminish prediction accuracy. Overall, the findings suggest that cubic spline interpolation is better suited for demographic modeling where population changes occur gradually over time. Future research may enhance predictive accuracy and robustness by incorporating smoothing splines, regression based models, machine learning techniques, and hybrid interpolation forecasting approaches.

5. References

1. de Boor, C (1978). *A practical guide to splines*. Applied Mathematical Sciences, 27, Springer, New York.
2. Preston S.H., Heuveline, P & Guillot, m (2001). *Demography: Measuring and modeling population processes*. Population and Development Review, Blackwell Publishers, Oxford 27(2), 365-367.
3. Logan, J. R., Xu, Z. & Stults, B. (2014). Interpolating population census data. *The Professional Geographer,* 66(3), 412-422.
4. Ibrahim, A. & Adeyemi, O. (2013). Comparative study of polynomial and spline interpolation methods. *International Journal of Mathematical Analysis,* 7(27), 1329–1338.
5. Lee, R. & Carter, L. (1992). Modeling and forecasting population growth. *Journal of the American Statistical Association,* 87(419), 659–671.

6. Appendices

Appendix A: MATLAB Program for Lagrange's Interpolation Method

```
syms x
P = 0;
u=x_nodes;
v=y_nodes;
n = length(u);

if length(x_nodes) ~= length(y_nodes)
   error('ERROR: Length of input vectors u and v must be equal.');
end

% Construct Lagrange polynomial
for i = 1:n
   N = 1; D = 1;
   for j = 1:n
      if j ~= i
```

```
            N = N*(x - x_nodes(j));
            D = D*(x_nodes(i) - x_nodes(j));
        end
    end
    P = P + (N/D)*y_nodes(i);
end

f(x) = simplify(P);

% Display polynomial
disp('Symbolic Lagrange Polynomial f(x):');
pretty(f(x))

% Evaluate at x_eval (if provided) and mark on the plot

 y_eval_lag = double(subs(f, x, x_interp));

 fprintf('\nInterpolated value at x = %.4f uisng Lagrange method is S(x) = %.4f\n', x_interp,
y_eval_lag);
```

Appendix B: MATLAB Program for Cubic Spline Interpolation Method

```
clc; close all;
syms x

% Step sizes
h = diff(x_nodes);

% --- Construct coefficient matrix for second derivatives M ---
A = sym(zeros(n));
rhs = sym(zeros(n,1));

% Natural boundary conditions: M1 = Mn = 0
A(1,1) = 1;
```

```
A(n,n) = 1;
rhs(1) = 0;
rhs(n) = 0;

% Internal equations
for i = 2:n-1
   A(i,i-1) = h(i-1);
   A(i,i)   = 2*(h(i-1) + h(i));
   A(i,i+1) = h(i);
   rhs(i)   = 6*((y_nodes(i+1) - y_nodes(i))/h(i) - (y_nodes(i) - y_nodes(i-1))/h(i-1));
end

% Solve for M (second derivatives)
M = A\rhs;

% --- Construct spline polynomials symbolically ---
S = sym(zeros(1, n-1)); % store spline for each interval

for i = 1:n-1
   xi  = x_nodes(i);
   xi1 = x_nodes(i+1);
   hi  = h(i);

   % Cubic spline formula in [xi, xi+1]
   S(i) = simplify( M(i)*(xi1 - x)^3/(6*hi) + M(i+1)*(x - xi)^3/(6*hi) + ...
                (y_nodes(i) - M(i)*hi^2/6)*(xi1 - x)/hi + ...
                (y_nodes(i+1) - M(i+1)*hi^2/6)*(x - xi)/hi );
end

% --- Display symbolic spline pieces ---
disp('Symbolic Cubic Spline Functions:')
for i = 1:n-1
   fprintf('\nInterval [%g, %g]:\n', x_nodes(i), x_nodes(i+1));
   pretty(S(i));
```

```
end

% Find which interval x_interp belongs to
interval = find(x_interp >= x_nodes(1:end-1) & x_interp <= x_nodes(2:end), 1);

if isempty(interval)
   error('The given x-value %.4f is outside the interpolation range [%g, %g].', ...
         x_interp, x_nodes(1), x_nodes(end));
end

% Evaluate the spline value at x_interp
y_interp_CS = double(subs(S(interval), x, x_interp));
fprintf('\nInterpolated value at x = %.4f uisng cubic spline method is S(x) = %.4f\n', x_interp,
y_interp_CS);
```

Appendix C: MATLAB Program for Comparison of Lagrange's Interpolation and Cubic Spline Interpolation Method

```
x_nodes = [0 1 2 3 4 5 6 7];     % Example x-values (change as needed)
y_nodes = [0 1 4 5 7 8 10 15];     % Example y-values (change as needed)
n = length(x_nodes);
% --- Input interpolation value ---
x_interp = input('\nEnter the x-value to interpolate: ');

%running cubic spline interpolation
cubic_spline

%running lagrange interpolation
lagrange

% Plot piece wise cubic splines
for i = 1:n-1
   h1 = fplot(S(i), [x_nodes(i), x_nodes(i+1)], 'r', 'LineWidth', 1.5);
   hold on
```

```
end

% --- Plot Lagrange polynomial ---
h2 = fplot(f, [min(u), max(u)], 'k', 'LineWidth', 1.5);
hold on

% --- Plot given data points ---
h3 = plot(x_nodes, y_nodes, 'bo', 'MarkerFaceColor', 'b');

% --- Mark interpolated points ---
h4 = plot(x_interp, y_interp_CS, 'go', 'MarkerSize', 6, 'MarkerFaceColor', 'g');
h5 = plot(x_interp, y_eval_lag, 'mo', 'MarkerSize', 6, 'MarkerFaceColor', 'c');

% --- Add one dummy (invisible) plot to represent all spline segments ---
hSpline = plot(NaN, NaN, 'r', 'LineWidth', 1.5);
hLag    = plot(NaN, NaN, 'k', 'LineWidth', 1.5);

% --- Set labels, title, and grid ---
xlabel('x');
ylabel('f(x)');
title('Cubic Spline vs. Lagrange Polynomial Interpolation');
grid on;

% --- Final clean legend (no repetition) ---
legend([hSpline, hLag, h3, h4, h5], ...
       {'Cubic Spline Interpolation', ...
        'Lagrange Polynomial Interpolation', ...
        'Data Points', ...
        'Interpolated Point (Cubic Spline)', ...
        'Interpolated Point (Lagrange)'}, ...
        'Location', 'best');
```

Journal of Science-FAS-SEUSL (2025) 06(02) 97-114
ISSN:2738-2184

The Novel Group Chain Acceptance Sampling Plan Using Minimum Angle Method for Non-Symmetrical Data Using Quartiles

Haalisha Aboobucker* and Dingiri Appulage Tharanga Madumali Kumari

Department of Mathematical Sciences, Faculty of Applied Sciences, South Eastern University of Sri Lanka 32200

*haalisha90@seu.ac.lk

Abstract

This paper suggests a Group Chain Acceptance Sampling Plan (GChSP-1) for non-symmetrical data under truncated life testing. Two types of risks arise in statistical quality control: producer's risk and consumer's risk. The Minimum Angle Method (MAM) is applied when designing the sampling plan to control and reduce these risks in a balanced manner. The original GChSP-1, developed in 2015, primarily addressed the producer's risk. Later, in 2022, MAM was incorporated using the mean as the quality parameter, which is more appropriate for symmetrical data, and in 2023, GChSP-1 for non-symmetrical data was extended with the median. As a further extension, this study proposes a GChSP-1 with MAM incorporated with the 3rd quartile. The performance of the 3rd quartile is compared with that of the median. All results were obtained using Sci-Lab programming software, and the results align with the previous studies**.** The optimal number of groups increases when the shape parameter and quartile ratio increase. Even though specified constant, number of preceding lots, and number of items per group increase, the optimal number of groups decreases. Notably, the 3rd quartile yields the smallest optimal number of groups, suggesting that it serves as a more effective quality parameter for GChSP-1 than the median. The suggested plan offers a valuable alternative for industrial inspection processes, allowing practitioners to select the most suitable plan based on specific requirements.

Keywords: Consumer's Risk, Group Chain Sampling Plan, Minimum Angle Method, Producer's Risk

1. Introduction

Acceptance Sampling is a statistical method used to evaluate the quality of products by inspecting a randomly selected sample rather than examining each individual items in a large batch. One significant classification of acceptance sampling is variables and attributes (Montgomery, 2009). The first acceptance sampling plan was developed by Epstein in 1954, which was known as the single sampling plan (SSP). This sampling strategy has two drawbacks: (1) when the acceptance number is set to be zero or one, the probability of accepting the lot decreases rapidly, and (2) the SSP does not indicate multiple inspections. To overcome these limitations, in 1955, the ChSP-1 was developed by Dodge as an alternative to SSP. Neither the SSP nor the ChSP-1 are not capable of multiple inspections. Multiple inspection is an effective approach in acceptance sampling because it groups sampling units, which helps reduce both inspection time and cost. Therefore, to address the gap of multiple inspections, the group sampling plan (GSP) was constructed by Aslam and Jun in 2009. Later, Mughal (2015) extended the idea by integrating the group concept with the ChSP-1, leading to the development of the Group Chain Sampling Plan (GChSP-1). Among the different attribute acceptance

Corresponding Author: haalisha90@seu.ac.lk

sampling plans, GChSP-1 is considered an efficient alternative to the earlier acceptance sampling methods.

There are two risks associated with acceptance sampling, namely, the producer's risk, α and the consumer's risk, β (Montgomery, 2009). Most researchers, when creating sampling plans, tend to focus more on minimizing the consumer's risk, while paying less attention to minimizing the producer's risk. This approach was common until 1997 when Soundararajan and Christina introduced the Minimum Angle Method (MAM), a method that aims to minimize the both risks (Soundararajan & Christina, 1997), (Teh, Aziz, & Zain, 2021). However, it's crucial in quality control and product development to consider and minimize both consumer's and producer's risks. This ensures a well-rounded approach that protects against the negative outcomes of both types of risks.

In truncated life testing, acceptance sampling plans are used to determine whether the lifetime or the durability of a product is equal to or greater than a pre-defined (hypothesized) value of time. When developing these plans, the average life of devices is often considered by assuming that data follow symmetrical distributions. However, in situations where the data doesn't follow a symmetrical pattern, other quality parameters, like median, quartiles, or percentiles, should be considered to address the non-symmetrical nature of the data (Gupta, 1962).

2. Literature Review

Acceptance Sampling plays an important role in quality control by determining whether a production lot should be accepted or rejected based on the inspection of a sample. Epstein (1954) is recognized as the first researcher to introduce the Single Acceptance Sampling Plan (SSP) for lifetime testing of attributes. However, the SSP has two major limitations. First, when the acceptance number is set to be zero or one, the probability of accepting the lot drops rapidly. Second, the SSP does not support multiple inspections. Dodge (1955) proposed the Chain Sampling Plan (ChSP-1) as an alternative to the traditional Single Acceptance Sampling Plan (SSP), which has zero acceptance numbers. Besides that, Mughal et al. (2015b) proposed ChSP-1 for the Pareto distribution of the 2nd kind. In traditional sampling plans like SSP and ChSP, only a single item is tested at a time. However, to address this limitation, Aslam and Jun (2009) introduced the Group Sampling Plan (GSP), which allows for testing multiple items as a group simultaneously. This approach improves efficiency in the inspection process. Building on this concept, Mughal et al. (2015) introduced a novel sampling approach known as Group Chain Sampling Plan (GChSP), which combines the principles of ChSP-1 and GSP for the Pareto Distribution of the 2nd kind. Teh et al. (2018) proposed the GChSP for the Exponential Distribution and conducted a comparison of the performance of GSP and GChSP for the Exponential Distribution by minimizing the consumer's risk.

Most of these earlier studies primarily focused on minimizing the consumer's risk while giving limited attention to the producer's risk. Soundararajan and Christina (1997) designed a variable single sampling plan for specified values of the sample size n, the acceptable quality level, and the limiting quality level using the Minimum Angle Method (MAM). Their approach aimed to minimize both consumer's and producer's risks. This provides an alternative to Epstein's (1954) Single Sampling Plan (SSP), which focused solely on minimizing the consumer's risk. Recently,

Teh et al. (2021) developed GChSP-1 for the Generalized Exponential Distribution using MAM which was identified as a better acceptance sampling procedure.

Another key factor in designing acceptance sampling plans is the selection of an appropriate quality parameter that reflects the nature of the data. Commonly, the mean is taken as the quality parameter for the life testing by assuming that the data have symmetrical behavior. Practically, the data does not always hold the symmetrical property. Recognizing this issue, Gupta (1962) developed a life testing plan for normal and log-normal distributions based on the mean and median to obtain the minimum sample size when the data exhibit non-symmetrical behavior. Rao et al. (2012) focused on percentiles and developed a time-truncated test plan based on the Inverse Rayleigh Distribution to minimize the specified consumer's risk. A TSGChSP has been developed by Zain and Aziz (2019) to address the non-symmetrical property of the Pareto Distribution of 2nd Kind by satisfying the consumer's risk at several values of the median ratio.

More recently, Teh et al. (2022) focused on a novel family of GChSP, which comprised six different GChSP using MAM, but this study was still based on the mean rather than considering other possible measures. Thus, Aboobucker (2023) wanted to address this issue by minimizing both the risks and handling the median as the quality parameter for the non-symmetrical data. She introduced a novel family of GChSP-1 designed for life testing when assessing the specified median life and compared the performance of the median with the findings of Teh (2022). She discovered that the median, which is the 2nd quartile, performs better than the mean for Generalized Exponential Distribution under different operating characteristic values (Aboobucker, 2023). Even though the most important gap has been satisfied by Aboobucker (2023), the comparison between the median and other quartiles was not done in her study. Thus, this study focuses on choosing the most effective quality parameter in both the median and the 3rd quartile using MAM for non-symmetrical data with the generated Sci-Lab coding.

The Minimum Angle Method

Soundararajan and Christina (1997) are referred to as the first researchers who applied MAM. They developed a variable acceptance sampling plan based on MAM. This method involves considering both producer's and consumer's risks in the development of an acceptance sampling plan. Simply, MAM considers the tangent angle between lines AB and AC in the OC curve, where A≡ $(p_1, 1-\alpha)$ and B ≡ (p_2, β) as shown in Figure 1. Further, $p_1$and p_2 represent the lot fraction defectives at AQL and LQL, respectively.

Using Figure 1, the tangent angle can be obtained by;

$$\tan\theta = \frac{p_2 - p_1}{L(p_1) - L(p_2)}$$

Therefore, the angle is;

$$\theta = \tan^{-1}\left|\frac{p_2 - p_1}{L(p_1) - L(p_2)}\right| \qquad (1)$$

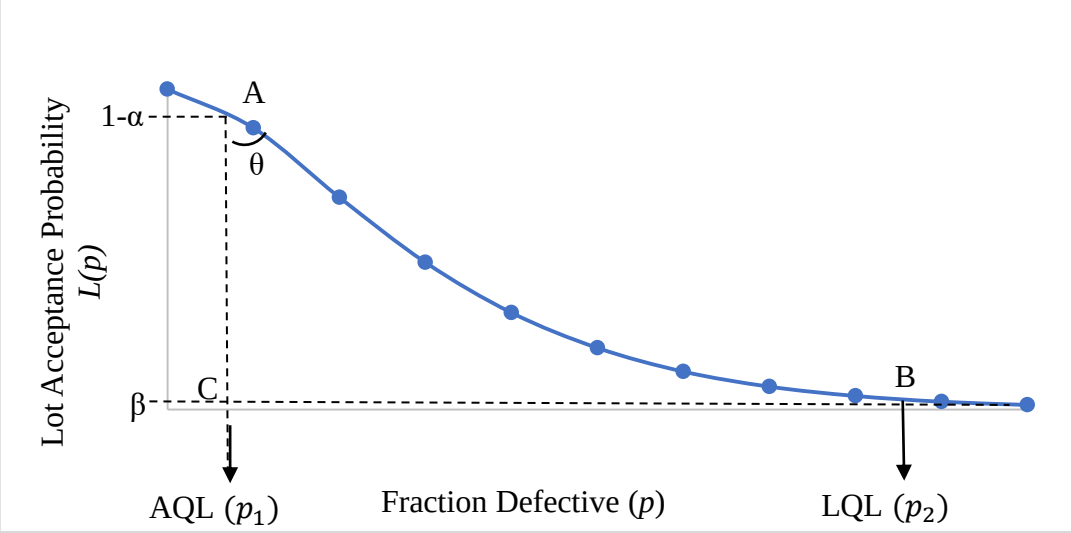

Figure 1: The Minimum Angle Method. Extracted From "New Family of Group Chain Acceptance Sampling Plans (GChSP) Using Minimum Angle Method (MAM) for Non-symmetrical Data. (Unpublished Master dissertation.) by H. M. Aboobucker, Z. Zain and N. Aziz, 2023, Universiti Utara Malaysia, Sintok, Kedah, Malaysia.

3. Methodology

The methodology and the design for GChSP-1 involve six steps, and it is summarized in Table 1 (Aboobucker, 2023).

Table 1: Steps in designing the GChSP-1

Phase I	Identification of design parameters
Phase II	Implementing the operating procedure
Phase III	Determining the probability of lot acceptance
Phase IV	Determining the probabilities for zero and one Defectives
Phase V	Determining the fraction defective for Generalized Exponential Distribution
Phase VI	Measuring the performance

Phase I: Identification of Design Parameters

The design parameters for GChSP are: producer's risk (α), consumer's risk (β), specified constant (a), number of preceding lots (i), number of items (r), and the 3rd quartile ratio $\left(\frac{Q}{Q_0}\right)$. These design parameters in Table 2 are used to determine whether the true 3rd quartile life of the item (Q) is greater than the specified 3rd quartile life of the item (Q_0).

Table 2: Pre-specified Values for the design parameters for GChSP-1

Design Parameters								
Producer's risk, α	0.10							
Consumer's risk, β	0.10							
Specified constant, a	0.25	0.50	0.75	1.00	1.25	1.50	1.75	2.00
Number of preceding lots, i	1	2	3	4				
Number of items,r	2	3	4	5				
3rd Quartile ratio at the AQL	2	4	6	8	10	12		
3rd Quartile ratio at the LQL	1							

Phase II: Implementing the operating procedure

The operating procedure is the most important component in the acceptance sampling plan. The sampling plan is designed step by step in this phase. Table 3 contains the operating procedure for the proposed sampling plan.

Table 3: The operating procedure for GChSP-1

Step 1	Finding the optimal number of groups (g) using MAM.
Step 2	Allocating the r number of items for each group.
Step 3	Specifying the test termination time t_0.
Step 4	Conducting the inspection procedure and finding number of defectives (d).
Step 5	Accept the current lot if $d = 0$ and reject the current lot if $d > 1$.
Step 6	Accept the current lot if $d = 1$, provided that no defectives recorded in the preceding i lots.

Phase III: Determining the probability of lot acceptance

Figure 2 illustrates the tree diagram for the lot acceptance criteria for the GChSP-1 when there are two preceding lots. D and $\overline{D}$ represent defectives and non-defectives, respectively. This tree diagram can be used to derive the probability of lot acceptance for GChSP-1.

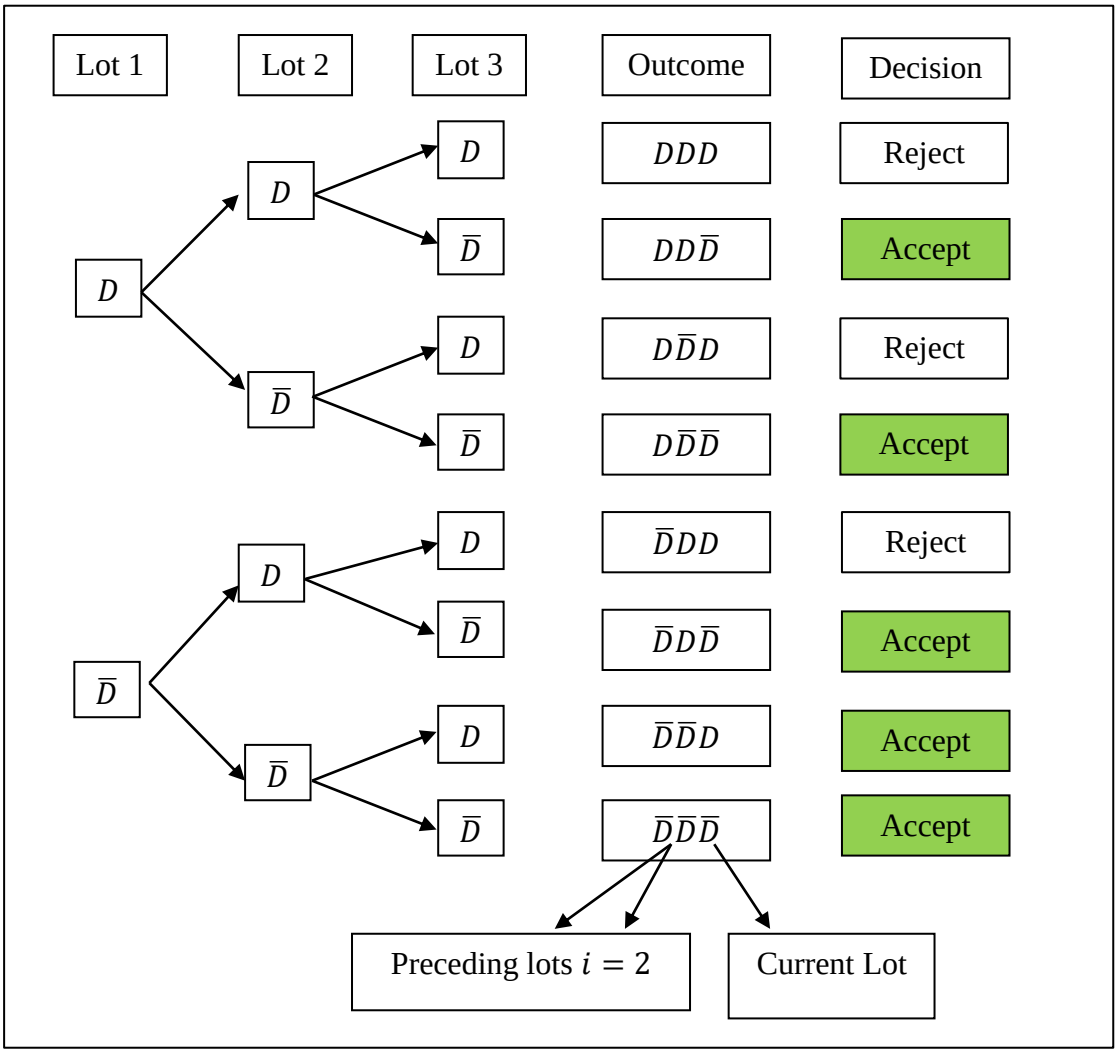

Figure 2: Tree diagram for the GChSP-1

There are five cases where the lot can be accepted, namely, $DD\overline{D}$, $D\overline{D}\overline{D}$, $\overline{D}D\overline{D}$, $\overline{D}\overline{D}D$ and $\overline{D}\overline{D}\overline{D}$. From that, the probability of lot acceptance for the GChSP-1 can be obtained as equation (2), where, P_0 and P_1 represent the probability of zero and one defective, respectively.

$$L(p)_{GChSP-1} = P_0P_0P_0 + P_0P_0P_1$$
$$L(p)_{GChSP-1} = P_0 + (P_0)^2P_1 \quad (2)$$

Equation (2) is derived for the number of preceding lots, $i = 2$. Then, generally for i preceding lots, the probability of lot acceptance for GhSP-1can be written as;

$$L(p)_{GChSP-1} = P_0 + (P_0)^iP_1 \quad (3)$$

Phase IV: Determining the probability of zero and one defectives

Probability of zero defects, P_0 implies the possibility of having no defects in the sample. Similarly, the probability of one defective, P_1 is the possibility of having exactly one defect in the sample. Both probabilities are essential in GChSP-1, as the acceptance criteria are determined by the occurrence of zero or one defect in the samples. Based on Figure 2, it can be derived that if no defects are found in the current sample, the lot is accepted. However, if one defect is found in the current sample, the lot can still be accepted provided that no defects were observed in the previous lot.

The P_0 and P_1 are derived as equations (4) and (5) using the binomial distribution, where g is the optimal number of groups, r is the number of items in each group, and the p is the fraction defective of the batch of items.

$$P_0(p) = \binom{gr}{0} * p^0 * (1-p)^{gr-0}$$
$$P_0(p) = (1-p)^{gr} \quad (4)$$

$$P_1(p) = \binom{gr}{1} * p^1 * (1-p)^{gr-1}$$
$$P_1(p) = (grp) * (1-p)^{gr-1} \quad (5)$$

Upon the simplification and the substitution of equations (4) and (5) into equation (3), the lot acceptance probability can be obtained.

$$L(p)_{GChSP-1} = (1-p)^{gr}\left[1 + \frac{grp(1-p)^{gri}}{(1-p)}\right] \quad (6)$$

The optimal number of groups, g is obtained at the AQL and LQL. Let $L(p_1)$ and $L(p_2)$ represent the probabilities at AQL and LQL, respectively. Then,

$$L(p_1) \geq 1 - \alpha \quad (7)$$
$$L(p_2) \leq \beta \quad (8)$$

Phase V: Determining the fraction defective for Generalized Exponential Distribution

The cumulative density function (CDF) of the generalized exponential distribution is given by;

$$p = \left[1 - exp\left(-\frac{t}{\sigma}\right)\right]^{\lambda}, t > 0, \lambda > 0 \quad (9)$$

σ and λ represent the scale and shape parameters, respectively.

The p^{th} Quartile point of the generalized exponential distribution is given by;

$$\theta_p = -\sigma \ln(1 - p^{1/\lambda}) \quad (10)$$

Then Equation (10) can be replaced in terms of the 3rd quartile (Q);

$$Q = -\sigma \ln(1 - (0.75)^{1/\lambda}) \quad (11)$$

Using equation (10) the scale parameter σ can be isolated as follows;

$$\sigma = \frac{\theta_p}{-\ln(1 - p^{1/\lambda})} \quad (12)$$

Furthermore, the test termination time, t_0 can be defined as the product of a specified constant, a and specified quartile life, Q_0; and it can be written as;

$$t = aQ_0 \quad (13)$$

Finally, the fraction defective for generalized exponential distribution can be obtained in the terms of 3rd quartile as follows.

$$p = \left[1 - exp\left(-\frac{aQ_0}{\frac{Q}{-\ln(1 - 0.75^{1/\lambda})}}\right)\right]^{\lambda} \quad (14)$$

Using the rules of logarithm equation (14) can be simplified as accordingly.

$$p = \left[1 - \left[(1 - 0.75^{\left(\frac{1}{\lambda}\right)}\right]^{\left(\frac{a}{Q/Q_0}\right)}\right]^{\lambda} \quad (15)$$

The calculation of the fraction defective, p, is conducted at both the AQL and the LQL. Specifically, the fraction defective at the AQL is represented as p_1, and it is computed with various 3rd quartile ratio values $\left(\frac{Q}{Q_0}\right)$ such as 2, 4, 6, 8, 10, and 12. Conversely, the fraction defective at the LQL is denoted as p_2 and is determined when the 3rd quartile ratio $\left(\frac{Q}{Q_0}\right)$ is fixed at 1.

Phase VI: Measuring the performance

In this study, the evaluation of the performance of the proposed novel GChSP-1 involves obtaining the optimal number of groups through various combinations of design parameters. Secondly, this study focuses on understanding how specific design parameters, such as the

specified constant (a), the number of preceding lots (i), the 3rd quartile ratio$\left(\frac{Q}{Q_0}\right)$, and the number of items (r), influence the optimal number of groups.

4. Results and Discussion

The optimal number of groups is proportional to the shape parameter of generalized exponential distribution based on the results (Tables 4-6). The shape parameter λ increases from 1 to 3 the number of groups increases from 5 to 53, while the other parameters remain constant $\left(a = 0.25, i = 1, r = 2, \frac{Q}{Q_0} = 12\right)$. The angle created by 5 groups is 16.75498° and the angle for 53 groups is 5.20496°. Applying the minimum angle theory leads to the conclusion that choosing 53 groups is more effective than selecting 5 groups, as it yields the smallest angle.

The second finding involves measuring the performance of the sampling plan when there is a change in the specified constant. The specified constant is increasing from 0.25 to 2, the optimal number of groups is decreasing from 19 to 1, while the other parameters are set to be $\left(\lambda = 2, i = 1, r = 2, \frac{Q}{Q_0} = 12\right)$. Therefore, it can be concluded that the optimal number of groups is inversely proportional to the specified constant of generalized exponential distribution, which obeys Teh (2022) and Aboobucker (2023).
The respective angles created by 19 groups and one group are 8.836903°and 42.35615°. This implies that 19 groups produce a smaller angle than one group. The reduction of the number of groups reduces the inspection cost, but it increases the time for the inspection. That implies 19 groups require less inspection time than one group. Since the angle created by 19 groups is small, it effectively differentiates the good and bad lots from the other.

The next finding concludes that the produced optimal number of groups is proportional to the 3rd quartile ratio. For instance, while the design parameters are set to be $(\lambda = 2, i = 1, r = 2, a = 0.25)$. Whenever the quartile ratio is increasing from 6 to 12, the optimal number of groups is increasing from 13 to 19, with the corresponding angles 8.92143° and 8.836903° respectively.

Finally, the performance of the sampling plan is measured by the changes in the number of preceding lots (i) and the number of items (r). The number of groups is inversely proportional to the number of preceding lots (i) and the number of items (r). For example, the optimal number of groups is 19 when $\left(\lambda = 2, i = 1, r = 2, a = 0.25, \frac{Q}{Q_0} = 12\right)$. And when the number of preceding lots and the number of items increased to 4 and 5, respectively, the optimal number of groups is equal to 7 while other parameters remain constant. From Table 4-6, there are many missing values marked by (-). This is because at one particular design parameter, the producer's risk, α and the consumer's risk, β fails to satisfy the condition as stated in Phase IV, that is, both α and β are set to be less than or equal to 0.1 no optimal groups can be found.

As a demonstration of the proposed sampling plan, let us assume an experimenter hypothesizes that the lifetime of a product follows a generalized exponential distribution. The aim is to determine whether the actual 3rd quartile life of the product is at least 1000 hours. If the

experiment is structured with the design parameters $\left(\lambda = 1, \frac{Q}{Q_0} = 12, i = 1, r = 2, a = 0.25\right)$, the optimal number of groups is 5. From that, the conclusion can be made that the experimenter should randomly select a sample of 10 items from the lot and assign two products to each group. The lot can be accepted when no defective found in the current sample within a 250-hour period of testing time, and further, the lot can be accepted if one defective item is recorded with no defective items observed in the previous lot.

Table 4: Optimal number of groups for GChSP-1 when $\lambda = 1$

Generalized Exponential Distribution, λ = 1										
			Specified Constant, α							
3rd Quartile Ratio	i	r	0.25	0.50	0.75	1.0	1.25	1.50	1.75	2.0
2	1	2	-	-	-	-	-	-	-	-
	2	3	-	-	-	-	-	-	-	-
	3	4	-	-	-	-	-	-	-	-
	4	5	-	-	-	-	-	-	-	-
4	1	2	-	-	-	-	-	-	-	-
	2	3	-	-	-	-	-	-	-	-
	3	4	-	-	-	-	-	-	-	-
	4	5	-	-	-	-	-	-	-	-
6	1	2	-	-	-	-	-	-	-	-
	2	3	-	-	-	-	-	-	-	-
	3	4	-	-	-	-	-	-	-	-
	4	5	-	-	-	-	-	-	-	-
8	1	2	-	-	-	-	-	-	-	-
	2	3	-	-	-	-	-	-	-	-
	3	4	-	-	-	-	-	-	-	-
	4	5	-	-	-	-	-	-	-	-
10	1	2	4 (17.04067°)	2 (27.14387°)	-	1 (36.36634°)	-	-	-	-
	2	3	-	-	-	-	-	-	-	-
	3	4	-	-	-	-	-	-	-	-
	4	5	-	-	-	-	-	-	-	-
12	1	2	5 (16.75498°)	2 (27.15349°)	-	1 (36.62911°)	1 (37.94919°)	-	-	-
	2	3	-	-	-	-	-	-	-	-
	3	4	-	-	-	-	-	-	-	-
	4	5	-	-	-	-	-	-	-	-

Table 5: Optimal number of groups for GChSP-1 when $\lambda = 2$

Generalized Exponential Distribution, λ = 2										
			Specified Constant, α							
3rd Quartile Ratio	i	r	0.25	0.50	0.75	1.0	1.25	1.50	1.75	2.0
2	1 2 3 4	2 3 4 5	- - - -	- - - -	- - - -	- - - -	- - - -	- - - -	- - - -	- - - -
4	1 2 3 4	2 3 4 5	10 (9.18541°) 5 (9.566894°) - -	3 (22.44308°) - - -	- - - -	- - - -	- - - -	- - - -	- - - -	- - - -
6	1 2 3 4	2 3 4 5	13 (8.92143°) 8 (9.07136°) 6 (9.207223°) 4 (9.304723°)	4 (21.9216°) 2 (22.47268°) 2 (22.82017°) 1 (23.32907°)	2 (30.97385°) 1 (31.86509°) 1 (32.1746°) -	1 (37.10598°) - - -	1 (38.63104°) - - -	- - - -	- - - -	- - - -

Generalized Exponential Distribution, λ = 2										
			Specified Constant, *a*							
3rd Quartile Ratio	*i*	*r*	0.25	0.50	0.75	1.0	1.25	1.50	1.75	2.0
8	1	2	15 (8.856659°)	5 (21.80655°)	3 (31.01803°)	2 (36.37643°)	1 (39.23043°)	1 (40.41526°)	1 (41.29709°)	-
	2	3	9 (8.936056°)	3 (22.03485°)	2 (31.57598°)	1 (36.63474°)	1 (40.21145°)	-	-	-
	3	4	7 (9.003534°)	2 (22.22428°)	1 (31.57186°)	1 (37.7408°)	-	-	-	-
	4	5	5 (9.058221°)	2 (22.57433°)	1 (31.98503°)	-	-	-	-	-
10	1	2	17 (8.839718°)	5 (21.78146°)	3 (30.93369°)	2 (36.33884°)	1 (39.69176°)	1 (40.83056°)	1 (41.59807°)	1 (42.09574°)
	2	3	11 (8.885666°)	3 (21.92853°)	2 (31.20555°)	1 (36.63257°)	1 (39.80578°)	1 (42.11779°)	-	-
	3	4	8 (8.925434°)	2 (22.08966°)	1 (31.47567°)	1 (37.04024°)	1 (41.19145°)	-	-	-
	4	5	6 (8.957735°)	2 (22.15427°)	1 (31.49749°)	1 (37.99526°)	-	-	-	-
12	1	2	19 (8.836903°)	6 (21.77804°)	3 (30.96325°)	2 (36.41433°)	2 (39.68166°)	1 (41.16596°)	1 (41.91368°)	1 (42.35615°)
	2	3	12 (8.865236°)	4 (21.87728°)	2 (31.10882°)	1 (36.7216°)	1 (39.73382°)	1 (41.77706°)	1 (43.26068°)	-
	3	4	8 (8.890977°)	3 (21.97053°)	1 (31.49714°)	1 (36.80435°)	1 (40.50193°)	1 (43.2452°)	-	-
	4	5	7 (8.913769°)	2 (22.0078°)	1 (31.33935°)	1 (37.32721°)	1 (41.68112°)	-	-	-

Table 6: Optimal number of groups for GChSP-1 when $\lambda = 3$

Generalized Exponential Distribution, λ = 3										
			Specified Constant, a							
3rd Quartile Ratio	i	r	0.25	0.50	0.75	1.0	1.25	1.50	1.75	2.0
2	1 2 3	2 3 4	- - -	- - -	- - -	- - -	- - -	- - -	- - -	- - -
	4	5	-	-	-	-	-	-	-	-
4	1	2	25 (5.221779°)	5 (18.79013°)	2 (29.99683°)	1 (36.91753°)	1 (38.74499°)	-		
	2	3	15 (5.28441°)	3 (19.11555°)	1 (31.02259°)	-	-	-	- -	- -
	3	4	11 (5.336538°)	2 (19.41603°)	1 (31.04615°)	-	-	-	- -	- -
	4	5	8 (5.383017°)	2 (19.74146°)	-	-	-	-		
6	1	2	34 (5.193708°)	7 (18.66036°)	3 (29.83°)	2 (36.33148°)	1 (39.74591°)	1 (40.91969°)	1 (41.71576°)	-
	2	3	21 (5.208256°)	4 (18.76136°)	2 (30.03893°)	1 (36.62098°)	1 (40.36738°)	-	-	-
	3	4	15 (5.220902°)	3 (18.83174°)	1 (30.4965°)	1 (37.12175°)	-	-	-	-
	4	5	12 (5.231881°)	2 (18.96286°)	1 (30.34824°)	1 (38.19557°)	-	-	-	-

Generalized Exponential Distribution, λ = 3										
			Specified Constant, *a*							
3rd Quartile Ratio	*i*	*r*	0.25	0.50	0.75	1.0	1.25	1.50	1.75	2.0
8	1	2	42 (5.19793°)	9 (18.68089°)	4 (29.90788°)	2 (36.51338°)	2 (40.09384°)	1 (41.60806°)	1 (42.25726°)	1 (42.57297°)
	2	3	26 (5.202329°)	5 (18.71412°)	2 (30.01313°)	1 (36.82737°)	1 (40.1382°)	1 (42.23526°)	1 (43.77269°)	-
	3	4	19 (5.206236°)	4 (18.73883°)	2 (30.0833°)	1 (36.72946°)	1 (40.71588°)	1 (43.6098°)	-	-
	4	5	15 (5.209852°)	3 (18.76256°)	1 (30.23661°)	1 (36.99736°)	1 (41.63166°)	-	-	-
10	1	2	48 (5.202237°)	10 (18.7034°)	4 (29.96961°)	3 (36.64449°)	2 (40.19479°)	1 (42.04838°)	1 (42.74203°)	1 (43.04413°)
	2	3	30 (5.203866°)	6 (18.71606°)	3 (30.00275°)	2 (36.72538°)	1 (40.25772°)	1 (42.15154°)	1 (43.29547°)	1 (44.11951°)
	3	4	22 (5.205344°)	5 (18.72974°)	2 (30.02597°)	1 (36.75093°)	1 (40.42174°)	1 (42.68651°)	1 (44.35086°)	-
	4	5	17 (5.206715°)	4 (18.74238°)	2 (30.10025°)	1 (36.79194°)	1 (40.77113°)	1 (43.47782°)	-	-
12	1	2	53 (5.20496°)	11 (18.71919°)	5 (30.0067°)	3 (36.70667°)	2 (40.30825°)	2 (42.22956°)	1 (43.06191°)	1 (43.40802°)
		3	34	7	3	2	1	1	1	1

	2 3 4	 4 5	(5.205663°) 24 (5.206305°) 19 (5.206903°)	(18.72474°) 5 (18.72978°) 4 (18.73449°)	(30.02147°) 2 (30.03911°) 2 (30.05562°)	(36.73852°) 1 (36.80993°) 1 (36.77776°)	(40.37646°) 1 (40.40156°) 1 (40.54452°)	(42.23449°) 1 (42.45864°) 1 (42.82033°)	(43.26737°) 1 (43.75064°) 1 (44.45808°)	(43.88374°) 1 (44.74928°) 1 (45.94674°)

The results obtained for the novel GChSP-1 with 3rd quartile is then compared with the GChSP-1 with the median (which is the 2nd quartile). The summary table is shown in following Table 7.

Table 7: Comparison on g and θ for GChSP-1 for 3rd Quartile and Median

	λ=1		λ=2		λ=3	
a	Median	3rd Quartile	Median	3rd Quartile	Median	3rd Quartile
0.25	10 (9.368341°)	5 (16.75498°)	46 (3.984866°)	19 (8.836903°)	98 (1.979615°)	34 (5.193708°)
0.50	5 (16.75498°)	2 (27.14387°)	13 (11.84188°)	6 (21.77804°)	18 (9.202207°)	7 (18.66036°)
0.75	3 (22.48811°)	-	6 (19.81252°)	3 (30.93369°)	7 (18.38568°)	3 (29.83°)
1.00	2 (27.14387°)	1 (36.36634°)	4 (26.37717°)	2 (36.33884°)	4 (26.3774°)	2 (36.33148°)
1.25	2 (30.07202°)	1 (37.94919°)	3 (31.32137°)	1 (38.63104°)	2 (32.21992°)	1 (38.74499°)
1.50	-	-	2 (34.78513°)	1 (40.41526°)	2 (36.13041°)	1 (40.91969°)
1.75	-	-	2 (37.42916°)	1 (41.29709°)	1 (38.01441°)	1 (41.71576°)
2.00	1 (36.36634°)	-	1 (38.45733°)	1 (42.09574°)	1 (40.12043°)	1 (42.57297°)

According to the Table 7 it can be observed that for the both median and the 3rd quartile, when shape parameter λ increases the optimal number of groups increase. The goal of designing the acceptance sampling plans is to obtain the optimal number of groups with the minimum angle. In this scenario $\lambda = 1$ produces optimal number of groups for both the quality parameters.

From the comparison of the performance of GChSP-1 with the two different quality parameters, median and the 3rd quartile with the design parameters $\left(\lambda = 1, \frac{Q}{Q_0} = 12, i = 1, r = 2, a = 0.25\right)$, it can be observed that the 3rd quartile produces 5 groups with the corresponding minimum angle of 16.75498° for GChSP-1 and the median produces 10 groups with the minimum angle of 9.368341°. By comparing the optimal number of groups produced by the two quality parameters for GChSP-1, it is sure that the 3rd quartile produces smaller number of groups (5 groups) than the median (10 groups). Finally, the findings ensure that the 3rd quartile produces the minimum number of groups for GChSP-1 rather than median while satisfying the requirements of MAM for given design parameters.

5. Conclusion

The purpose of this paper is to develop a novel GChSP-1 for the generalized exponential distribution for non-symmetrical data using minimum angle method using 3rd quartile as the quality parameter. The 3rd quartile ratio is used as the quality parameter to assure the hypothesized life of the items as the previous study has focused on the median. Thus, both of the quality parameters were finally compared to check the efficient quality parameter to satisfy the industry

personals to make sure a choice of quality parameter with reduced cost of and time of inspection under the natural non-symmetrical property of the data.

The optimal number of groups depends on five parameters such that the optimal number of groups is increasing while the shape parameter and the 3rd quartile ratio are increasing. Conversely, when the specified constant, number of preceding lots and number of items in the group is increasing the optimal number of groups are decreasing. The purpose of designing any acceptance sampling plan is to obtain minimum number of samples from the lot. In the case of proposed GChSP-1, it aims to obtain optimal number of groups with smallest angle. This paper proves that smaller values of shape parameter always produce smaller number of groups than the higher values of the shape parameter.

Finally, the comparison is made with the proposed GChSP-1 and the GChSP-1 with the median. The comparison ensures that that the 3rd quartile produces the minimum optimal number of groups rather than median for the GChSP-1 while satisfying the requirements of MAM. Therefore, it can be concluded that the proposed GChSP-1 can be applied as an alternative in the industry.

The aim of proposed GChSP-1 is to obtain the minimum sample sizes along with reducing both consumer's and producer's risks, and to enhance time and cost efficiency. Financially, GChSP-1 contributes to cost savings in the context of multiple inspections, aligning with organizational goals of productivity enhancement and operational cost reduction. This can be considered as a practical application of digital advancements in quality control aspects, optimizing industrial processes and financial outcomes through efficient acceptance sampling.

References

1. Aboobucker, H. M. (2023). New Family of Group Chain Acceptance Sampling Plans (GChSP) Using Minimum Angle Method (MAM) for Non-symmetrical Data. (Unpublished Master dissertation.) Universiti Utara Malaysia, Sintok, Kedah, Malaysia.

2. Aslam, M., & Jun, C. (2009). A Group Acceptance Sampling Plans for Truncated Life Tests based on the Inverse Rayleigh and Log-Logistic Distributions. *Pakistan Journal of Statistics, 25*(2), 107-119.

3. Epstein, B. (1954). Truncated life tests in the exponential case. *The Annals of Mathematical Statistics, 25*(3), 555-564.

4. Govindaraju, K., & Lai, C. (1998). A Modified ChSP-1 Chain Sampling Plan, MChSP-1, with very Small Sample Sizes. *American Journal of Mathematical and Management Sciences, 18*(3 & 4), 343-358.

5. Gupta, S. (1962). Life Test Sampling Plans for Normal and Lognormal Distributions. *American Statistical Association and American Society for Quality, 4*(2), 151-175.
6. Montgomery, D. C. (2009). *Introduction to Statistical Quality Control.* United States of America: John Wiley & Sons.

7. Mughal, A., Zain, Z., & Aziz, N. (2015). Time Truncated Generalized Chain Sampling Plan for Pareto Distribution of the 2nd Kind. *Research Journal of Applied Sciences, Engineering and Technology, 11*(3), 343-346.

8. Mughal, A., Zain, Z., & Aziz, N. (2015). Time Truncated Group Chain Sampling Strategy for Pareto Distribution of the 2nd Kind. *Research Journal of Applied Sciences, Engineering and Technology, 10*(4), 471-474.

9. Ramaswamy, A., & Jayasri, S. (2015). Time Truncated Modified Chain Sampling Plan for Selected Distributions. *International Journal of Research in Engineering and Science (IJRES), 3*(3), 01-18.

10. Rao, G., Kantam, R., Rosaiah, K., & Reddy, J. (2012). Acceptance Sampling Plans for Percentiles based on the Inverse Rayleigh Distribution. *Electronic Journal of Applied Statistical Analysis, 5*(2), 164-177.

11. Soundararajan, V., & Christina, A. (1997). Selection of single sampling variables plans based on the Minimum Angle. *Journal of Applied Statistics, 24*(2), 207-217.

12. Teh, M., Aziz, N., & Zain, Z. (2021). A New Method in Designing Group Chain Acceptance Sampling Plans(GChSP) for Generalized Exponential Distribution. *International Journal of Quality & Reliability Management, 38*(5), 1116-1129.

13. Teh, M., N., A., & Z., Z. (2018). Group Chain Sampling Plans beased on Truncated Life Test for Exponential Distribution. *International Journal of Pure and Applied Mathematics, 119*(3), 491-500.

14. Zain, Z., & Aziz, N. (2019). Constructing Two-Sided Group Chain Acceptance Sampling Plans for Non-Symmetrical Data. *International Journal of Supply Chain Management, 8*(5), 2051-3771.

Journal of Science-FAS-SEUSL (2025) 06(02) 115-122
ISSN:2738-2184

The Study of the role of CuSCN and Spiro-OMETAD in the hole transport of Sb_2S_3 solar cells

M.A. Farhana[a] and J. Bandara[b*]

[a]Department of Physical Sciences, Faculty of Applied Sciences, South Eastern University of Sri Lanka, Sammanthurai, Sri Lanka 32200
[b]National Institute of Fundamental Studies, Hantana Road, Kandy, Sri Lanka 20000

[*]jayasundera.ba@nifs.ac.lk

Abstract:
In this study, we systematically examine Sb_2S_3 solar cells featuring CuSCN and Spiro-OMETAD as hole-transport layers (HTLs) across four different configurations, such as a single layer of CuSCN (FTO/TiO_2/Sb_2S_3/CuSCN/Ag), a bilayer of CuSCN/Spiro (FTO/TiO_2/Sb_2S_3/CuSCN/Spiro/Ag), a bilayer of Spiro/CuSCN (FTO/TiO_2/Sb_2S_3/Spiro/ CuSCN/Ag), and a single layer of Spiro (FTO/TiO_2/Sb_2S_3/Spiro/Ag). Photovoltaic performance of the cells showed the highest power conversión efficiency (PCE) for a single layer of Spiro and followed by a bilayer of CuSCN/Spiro, a single layer of CuSCN, and a bilayer of Spiro/CuSCN. Due to the optimal energy level alignment and interface resistance of Spiro and Sb_2S_3, superior performance was obtained compared to other configurations. Architecture employing CuSCN exclusively delivered competitive power conversión efficiency consistent with reported favourable properties in solar cells. Introducing a CuSCN interlayer beneath Spiro yielded slightly low performance, while CuSCN at the top of Spiro yielded inferior performance. By carefully engineering bilayer stacks, the strength of both materials can be harnessed effectively without introducing interfacial impediments, and high-efficiency Sb_2S_3 photovoltaic designs.

Keywords: Bilayer, HTLs, Interface

1. Introduction

Solar cell technology is a key component in the transition to sustainable energy sources because of its versatility and scalability. The first solar cell was invented with a power conversion efficiency of just 1%, whereas current commercialised solar cells typically exhibit an efficiency of above 23% [1-2]. This explores a significant progress in solar cell technology. These commercial solar cells can be classified into four types: monocrystalline, polycrystalline, thin films, and passivated emitter and rear cell (PERC) solar panels. Monocrystalline solar panels are made from single-crystal silicon solar cells, while polycrystalline ones consist of multiple silicon fragments that are melted and poured. Both types have achieved top efficiencies of 23-26%. Thin-film solar cells are hundreds of times thinner than other solar panels, which makes them more flexible and lightweight. Different types of thin film solar panels include amorphous silicon, cadmium telluride (CdTe), and copper indium gallium selenide (CIGS), which have recently reached maximum efficiencies of 14%, 22.6%, and 23.6%, respectively [3].

Since solid-state solar cells simplify manufacturing and enhance durability, researchers are actively working to introduce new materials to address the scarcity and toxicity of traditional

Corresponding Author: jayasundera.ba@nifs.ac.lk

materials, such as CIGS and CdTe. Among the various components of solar cells, the front and back contacts, active material (absorber), and electron and hole transport layers are fundamental. Since the charge extraction is one of the crucial features, the Hole Transport Materials (HTMs) are widely investigated in solar cells. These HTMs are used to prevent the undesired charge recombination at the interface and facilitate the charge transaction. Consequently, our study examined the development of incorporating HTMs between Sb_2S_3 and the front contact, with Sb_2S_3 serving as the active layer (light absorber). Although some research has been conducted without HTMs, the efficiency remains lacking.

2. Literature Review

The amorphous nature, good conductivity with dopants, and high melting point of spiro-OMeTAD make it one of the most adaptable HTMs. Since pristine spiro-OMeTAD has relatively low hole mobility (10^{-4}-10^{-5} cm^2 V^{-1} s^{-1}) and low conductivity, it exhibits poor performance. Therefore, spiro-OMeTAD is prepared by doping with LiTFSI and tBP [4-5]. These types of organic HTMs are widely used for their high efficiency in solar cells. However, the organic materials are much expensive compared to inorganic materials also require complex synthesis. Due to the high hole mobility (0.01-0.1 cm^2 V^{-1} s^{-1}) and thermal stability, CuSCN is an extensively studied inorganic compound in solar cell applications as a HTM [6-7]. Since this resource is abundant and relatively inexpensive, the fabrication cost can be reduced. In recent years, CuSCN has been widely used in perovskite solar cells and solid-state dye-sensitized solar cells (SSDSSC). Moreover, numerical studies of CuSCN as a HTM show that with a particular architecture, efficiency can reach 25% in perovskite solar cells [8] and 17% in SSDSSC [9]. Therefore, we used CuSCN and spiro as HTMs in this study to evaluate the Sb_2S_3 solar cells.

3. Methodology

3.1 Preparation of TiO_2 layer

A mixture of 50 µl of di-ethanolamine and 910 µl of butan-1-ol was stirred for 10 minutes. Then, 75 µl of TTIP was added to the above mixture to prepare a clear precursor solution of 0.25 mM TiO_2. The prepared solution was spin-coated on the cleaned FTO glass at 3000 rpm for 30 s. The TiO_2 layer was fabricated with four spinning cycles. After every spinning cycle, the TiO_2 films were heated on the hot plate at 180 ^oC for 5 minutes. Finally, TiO_2 was sintered inside the furnace at 500 ^oC for 1 hour with 1 1-hour ramp and followed the natural cooling. They were used as an electron transport layer in our solar devices.

3.2 Preparation of active (Sb_2S_3) layer

114 mg of thiourea (TU) was mixed with 1 ml of 2-methoxyethanol and stirred until completely dissolved. Then, 228 mg of $SbCl_3$ was added to the TU solution and stirred for 30 minutes. The precursor solution was spin-coated at 4000 rpm for 30 s on the TiO_2 layer. It was heated inside the tube furnace at 180 °C for 1 min and followed by annealing inside the tube furnace at 280 °C for 10 minutes under N_2 gas.

3.3 Preparation of hole transport layer

A 20 mg of CuSCN was dissolved in 1 ml of 2-Ethylsulfide to prepare the CuSCN solution. Then, the Spiro solution was prepared by using 3.6 mg of Spiro-OMeTAD in 100 μl of chlorobenzene, 1.0 μl of Li+ solution, and 1.5 μl of TBP. The Li+ solution was prepared by adding 520 mg of bis (trifluoromethane sulfonyl) imide lithium salt to 1 ml of acetonitrile. The prepared solutions of the above CuSCN and Spiro were spin-coated on Sb_2S_3 at 3000 rpm for 30 s. The coated cells were heated on the hot plate at 100 ^oC for 20 minutes.

3.4 Counter electrode preparation

Finally, 70 nm of silver (Ag) layer was deposited by the thermal evaporation technique.

3.5 Cell assembly

The following sets of cells were fabricated separately.

i. FTO/TiO_2/Sb_2S_3/CuSCN/Ag;
ii. FTO/TiO_2/Sb_2S_3/CuSCN/Spiro/Ag;
iii. FTO/TiO_2/Sb_2S_3/Spiro/CuSCN /Ag;
iv. FTO/TiO_2/Sb_2S_3/Spiro/Ag

3.6 Characterizations

The cells were fabricated with an effective area of 0.18 cm^2. Current–Voltage measurements and EIS were done of each cell using Metrohm Autolab under the illumination of 100 mW cm^{-2} with AM 1.5 spectral filter. IPCE curves were measured as a function of wavelength from 300 nm to 800 nm using the Bentham PVE300 photovoltaic Device Characterization System.

4. Results and Discussion

4.1 Current Density-Voltage (J-V) analysis

Figure 1 presents the J-V characteristic curves of the devices with various HTM configurations, and photovoltaic parameters, including short circuit current density (Jsc), open circuit voltage (Voc), fill factor (FF), and power conversion efficiency (PCE) are summarized in Table 1. The cell of FTO/TiO_2/Sb_2S_3/Spiro/CuSCN/Ag showed poor performance, while FTO/TiO_2/Sb_2S_3/Spiro/Ag demonstrated superior performance. The cell with Spiro reached a PCE of 3.72%, with a Jsc of 14.9 mA cm^{-2}, Voc of 585.6 mV, and a fill factor of 42.6%. This efficiency was nearly 16 times greater than the cell of FTO/TiO_2/Sb_2S_3/CuSCN/Ag. The electronic properties of Spiro and CuSCN are illustrated in Table 2. It was noted that photogenerated holes quickly localize on sulfur atoms in Sb_2S_3, creating sulfide radical species. A two-step hole injection was noted across the Sb_2S_3/CuSCN interface. It was indicated by the exponential time constant of the transfer of the trapped holes to CuSCN [10]. However, the formation of large CuSCN crystals impedes the efficiency of hole transfer, leading to a poor interfacial contact and increased recombination losses. Additionally, the hole extraction can be hindered by the defect at the CuSCN/Sb_2S_3 interface, which reduces the device performance.

The material with high hole mobility reduces losses during hole transport. But, the interface of Sb_2S_3/CuSCN in solar cells exhibits a lower hole extraction than the electron extraction. Therefore, most of the holes are laying in Sb_2S_3, which leads to the recombination at TiO_2/Sb_2S_3. Hence, due to the poor hole transfer, the cell reached low efficiency with CuSCN. For the effective extraction of holes, the lowest unoccupied molecular orbital (LUMO) level of HTM must be well-matched with the LUMO level of the acceptor (Sb_2S_3) to minimize charge injection losses. Figure 2 illustrates the energy levels of different components in our solar cell. The reported values of LUMO of Sb_2S_3, CuSCN, and doped Spiro-OMETAD are 5.4, 5.3, and 5.2 eV. The barrier height decreases as the work function increases when the electrode contacts the p-type material [11]. Due to energy level alignment, excitons can be efficiently separated by the built-in electric field, transmitted to the surface layer and back layer, and collected by the corresponding electrodes. The HOMO and LUMO levels of TiO_2, Sb_2S_3, and HTMs increase gradually, which can improve the PCE. Since CuSCN/Spiro is better aligned compared to Spiro/CuSCN, this results in smooth charge transfer that reduces energy loss due to mismatched energy levels. Furthermore, a superior interface is formed by the CuSCN with the absorber layer, which leads to lower interfacial defect densities, then it helps to suppress non-radiative recombination and improves Voc and FF. This indicates that the efficiency in the CuSCN/Spiro configuration is higher compared to that in Spiro/CuSCN in our cells.

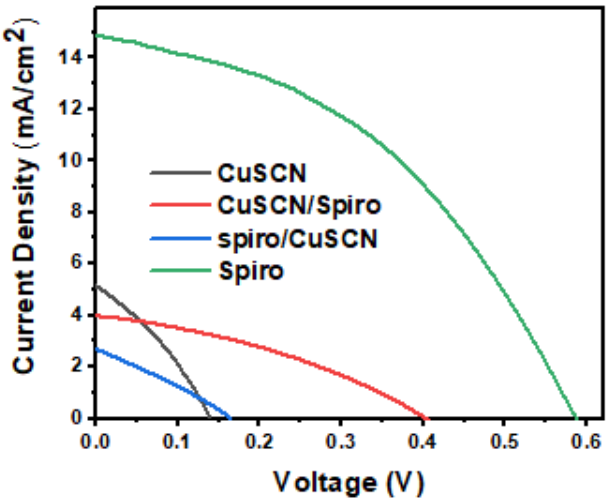

Figure 1: Current density-Voltage (J-V) curves of the devices with various configurations of HTMs

However, the FTO/Sb_2S_3/Spiro/Ag cell exhibits higher efficiency than FTO/TiO_2/Sb_2S_3/CuSCN/Spiro/Ag because the CuSCN surface is rough. The non-passivated interface introduces trap states, which can produce non-radiative recombination, leading to the low Voc compared to the spiro film.

Table 1: Photovoltaic parameters of the devices with various configurations of CuSCN and Spiro as HTMs

HTM	J_{SC} (mA cm^{-2})	V_{OC} (mV)	FF (%)	PCE (%)
CuSCN	5.01	136.8	33.2	0.23
CuSCN/Spiro	4.1	398.4	36.3	0.60
Spiro/CuSCN	2.7	161.0	29.5	0.13
Spiro	14.9	585.6	42.6	3.72

Table 2: The electronic properties of P3HT, Spiro-OMeTAD, and CuSCN [12, 13]

HTM	Energy gap (eV)	Conductivity (S cm^{-1})	Hole Mobility ($cm^2 V^{-1} S^{-1}$)	Hole Diffusion Co-efficient ($cm^2 s^{-1}$)
Spiro-OMeTAD	3.1	5.92×10^{-4}	2×10^{-5}	2.3
CuSCN	3.5	10^{-2}	1×10^{-1}	5.2×10^{-6}

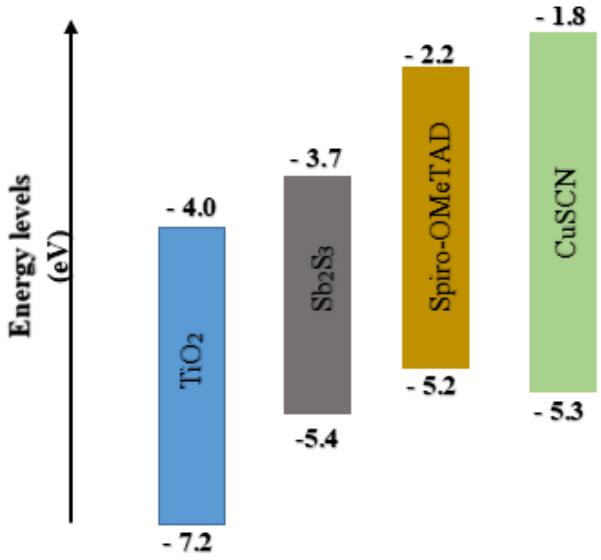

Figure 2: Schematic diagram of the energy levels of TiO_2, Sb_2S_3, Spiro-OMeTAD, and CuSCN

4.2 External Quantum Efficiency (EQE) measurement

The obtained IPCE spectra for the different configurations of HTMs are shown in Figure 3. The device with Spiro exhibits nearly 67% EQE, while the devices with CuSCN, CuSCN/spiro, and Spiro/CuSCN exhibit 20%, 15%, and 6%, respectively. These EQE responses align well with the Jsc values of the devices, which were obtained from J-V measurements. This spectrum indicates that charge collection in FTO/TiO_2/Sb_2S_3/Spiro/Ag is superior to that of the other configurations. Devices with a single layer of Spiro exhibited the

highest EQE spectral, consistent with superior Jsc. The single layer of CuSCN showed a strong and stable long- wavelength hole extraction due to optical transparency. Spiro on CuSCN showed a slight dip in the region of 400-600 nm. It can be due to the additional absorption or extraction loss at this combination. Because some of the incident light may have been absorbed by the HTL layers (CuSCN or Spiro) themselves, preventing those photons from reaching the Sb_2S_3 absorber and contributing to current. Spiro/CuSCN underperformed across all wavelengths, matching its high interfacial resistance.

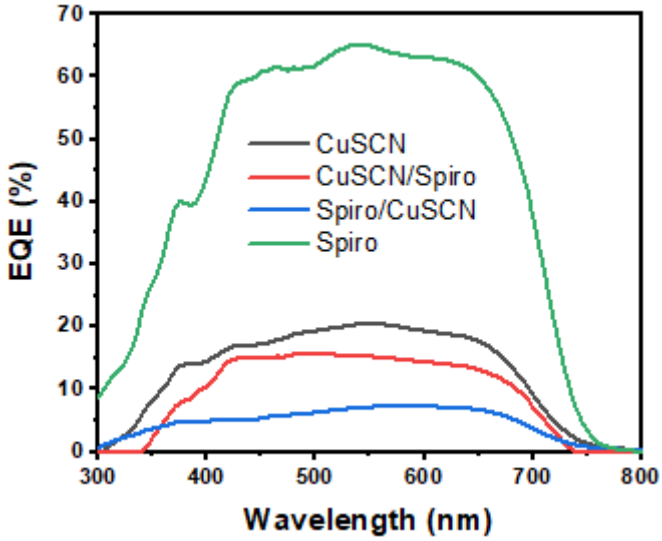

Figure 1: The EQE response curves of the devices with various configurations of HTM

4.3 Electrochemical Impedance Spectroscopy (EIS)

Figure 4 shows the EIS plot for the devices with different combinations of CuSCN and Spiro as HTM. The extracted impedance parameters from the fitting curves are listed in Table 3. The arc at high frequency corresponds to the hole transport. This hole transport affects FF, which contributes to the series resistance. The Rs represent the series resistance, while R_1 and R_2 are the charge transfer resistance at Sb_2S_3/HTM and TiO_2/Sb_2S_3.

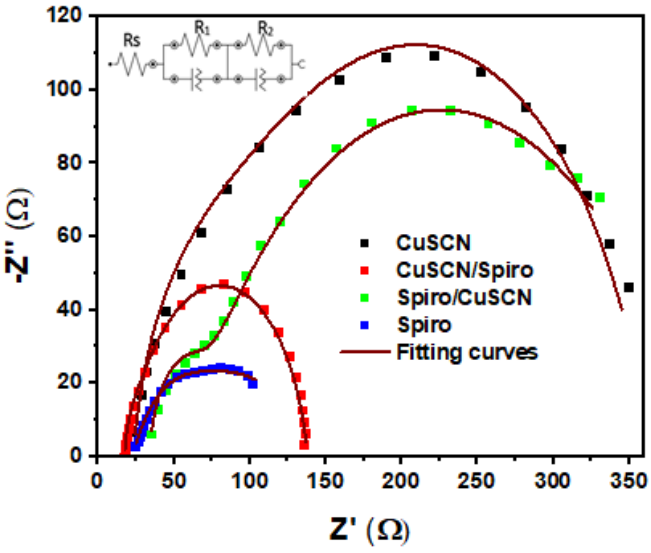

Figure 2: EIS plot with the equivalent circuit of the devices with various configurations of CuSCN and Spiro as HTMs

If the interface is not passivated well, it may introduce trap states**,** which increase non-radiative recombination**,** and the inhomogeneities create shunting paths or hinder complete coverage. This leads the charge transfer resistance. In the devices with CuSCN, the hole extraction is hard. Therefore, R_1 is considerably high in FTO/TiO_2/Sb_2S_3/CuSCN/Ag. Due to the recombination process at TiO_2/Sb_2S_3, the R_2 could be high. By introducing Spiro on CuSCN as HTM, the R_1 reduces because of the band alignment and the ability of hole transfer of Spiro. It reduces the R_S value too. But, for the device with Spiro/CuSCN as HTM, the band alignment with Sb_2S_3 is being interrupted. Therefore, the resistance is increasing. However, the device with Spiro as HTM shows very low R_1 compared to others, which could surpass the R_2 and R_S.

By comparing the R_2 values of the devices with CuSCN/Spiro and Spiro, the device with Spiro exhibits a higher value than CuSCN/Spiro. But the device with Spiro reveals a higher efficiency than CuSCN/Spiro. Because, after the separation of photogenerated carriers, they get recombined before reaching the selective contacts in CuSCN/Spiro.

Table 1: Impedance parameters of the devices with various configurations of CuSCN and Spiro as HTMs

HTM	Rs (Ω)	R_1 (Ω)	R_2 (Ω)
CuSCN	23.3	281	58.5
CuSCN/Spiro	17.6	115	6.07
Spiro/CuSCN	33.4	334	26.0
Spiro	22.0	99.2	22.5

5. Conclusion

This study systematically evaluated the performance of Sb_2S_3 solar cells employing various hole transport layers, including CuSCN and Spiro, and their combinations. Electrochemical Impedance Spectroscopy analysis revealed considerably less series resistance (Rs) and charge transfer resistances (Rct) for a single layer of spiro, which attributes the compactness of spiro as HTL. Spiro/CuSCN layer showed higher Rs and Rct compared to CuSCN/Spiro. The reduction of charge transfer resistance implies the mínimum recombination and efficient hole transfer. External quantum efficiency spectra aligned with Jsc trends and proved that the Spiro over CuSCN introduces an unfavourable interface morphology, leading to the losses. EQE of a single CuSCN showed a stable performance. Our findings indicate that the sequence of HTL deposition significantly influences device efficiency. Device employing Spiro as the HTL achieved the highest power conversion efficiency attributed to its favourable energy level alignment, especially interfacial connection and efficient hole extraction capabilities. The CuSCN configuration exhibited intermediate performance, suggesting that the sequence of a HTL deposition influences both charge transport and interfacial interactions.

.

References

1. Martin A. Green. (2019). The Path to 25% Silicon Solar Cell Efficiency: History of Silicon Cell Evolution. *Prog. Photovolt: Res. Appl.*, 17:183–189.
2. Jason Svarc. (2025). Most efficient solar panels 2025. Retrieved March 20, 2025.
3. NREL transforming energy, Best Research Cell Efficiencies. 2025 [online] Available at: https://www.nrel.gov/pv/interactive-cell-efficiency.html [Accessed 18 June 2025].
4. Rombach, F.M., Haque, S. A., Macdonald, T.J. (2021). Lessons learned from spiro-OMeTAD and PTAA in perovskite solar cells. *Energy & Environmental Science*.
5. Li, G., et al. (2022). Inhibited Aggregation of Lithium Salt in Spiro-OMeTAD for Perovskite Solar Cells. *Crystals*, 12(2), 290.
6. Chen, J., Park, N.G. (2018). Inorganic hole transporting materials for stable and high efficiency perovskite solar cells. *The Journal of Physical Chemistry C*, 122(25), 14039-14063.
7. Matebese, F., Taziwa, R., Mutukwa, D. (2018). Progress on the synthesis and application of CuSCN inorganic hole transport material in perovskite solar cells. *Materials* 11(12), 2592.
8. Syed Zulqarnain Haider, Hafeez Anwar, and Mingqing Wang. (2019). Theoretical Device Engineering for High-Performance 2 Perovskite Solar Cells Using CuSCN as Hole Transport Material Boost the Efficiency Above 25%. Phys. *Status Solidi A*, 1900102.
9. O'Regan B., Lenzmann F., Muis R., A. (2002). solid-state dyesensitized solar cell fabricated with pressure-treated P25-TiO_2 and CuSCN: Analysis of pore filling and IV characteristics. *Chem. Mater.*, 12, 5023–5029.
10. Christians, J.A., Kamat, P.V., (2013). Trap and transfer. Two-step hole injection across the Sb_2S_3/CuSCN interface in solid-state solar cells. *Acs Nano* 7(9), 7967-7974.
11. Feng, P., et al. (2010). Nonvolatile resistive switching memories-characteristics, mechanisms and challenges. *Progress in Natural Science:* Materials International 20, 1-15.
12. Jiménez-López, J., et al. (2017). Charge injection, carriers recombination and HOMO energy level relationship in perovskite solar cells. *Scientific reports* 7(1), 1-10.
13. Madhavan, V.E., et al. (2019). CuSCN as hole transport material with 3D/2D perovskite solar cells. *ACS Applied Energy Materials* 3(1), 114-121.

Journal of Science-FAS-SEUSL (2025) 06(02) 123-132
ISSN:2738-2184

Comparative Study of Mn^{2+} and Ni^{2+} Doping Effects on TiO_2 Quantum dot Photoconductive UV Photodetectors Fabricated by Doctor Blading Method

R.F. Zahra and U.L. Zainudeen*

Department of Physical Sciences, Faculty of Applied Sciences, South Eastern University of Sri Lanka, Sammanthurai, Sri Lanka 32200

*ulzdeen@seu.ac.lk

Abstract

Semiconductor quantum dots have been identified as potential materials for optoelectronic devices because of their size-dependent properties such as tunable bandgap and generation of multi-excitons. In this work, a systematic comparative study of the doping influence of Mn^{2+} and Ni^{2+} on the responsivity of TiO_2 quantum dot-based photoconductive ultraviolet detectors is reported. TiO_2 quantum dots were deposited on fluorine-doped tin oxide (FTO) substrates and doped with 5 mM concentrations of Mn^{2+} and Ni^{2+} ions using varying volumes (5-35 µl) to optimize the detection efficiency for 395 nm UV radiation. The results showed that the optimized volumes for Ni^{2+} and Mn^{2+} doping were 15 µl and 25 µl, respectively, resulting in responsivities of 128.3 µA/W and 22.66 µA/W, respectively, representing a 5.7 times enhancement with Ni^{2+} doping compared to a 1.4 times enhancement with Mn^{2+} doping compared to undoped TiO_2 (0.09 µA/W). Optical absorption spectroscopy analysis confirmed that the optimized quantum dot size resulted in a bandgap of 3.18 eV, which was exactly the same as the 395 nm wavelength of detection due to quantum confinement. FTIR spectroscopy analysis has confirmed the formation of Ti-O-Ni bonds and shown the degradation of the environment due to C=O contamination. This study has shown that Ni^{2+}-doped TiO_2 quantum dots, produced using scalable and low-cost techniques, are promising materials for the application of UV photon detection.

Keywords: TiO_2 quantum dots, Doctor blade technique, Nickel doping, Manganese doping

1. Introduction

Ultraviolet (UV) photodetectors have received considerable attention from the research community owing to their diverse applications in environmental monitoring, chemical/biological sensing, optical communication systems, flame sensors, and space exploration missions [1, 2]. A UV photodetector with high sensitivity, fast response time, stability, low power consumption, and simple and inexpensive fabrication processes is highly desirable [3]. Conventional UV detectors employing silicon photodiodes are complex and expensive because of the narrow bandgap of silicon (1.1 eV), which allows visible and infrared light to pass through [4].

The semiconductors with wide band gaps, such as GaN, SiC, ZnO, and TiO_2, provide inherent visible-blind UV detection without the need for filtering [5]. Among these, titanium dioxide (TiO_2) has been found to be a highly promising material owing to its chemical inertness, non-toxicity, low cost, and suitable bandgap value (~3.2 eV for anatase phase), which corresponds to an absorption edge of ~387 nm [6]. Nevertheless, the undoped TiO_2 photodetectors have been found to have low responsivity owing to the fast recombination of electron-hole pairs and poor charge transport properties [7].

Corresponding Author: ulzdeen@seu.ac.lk

Several approaches have been explored to improve the performance of TiO_2 photodetectors, such as the creation of heterojunctions [8], surface plasmon resonance effects [9], and doping with elements [10]. Doping with ions of transition metals leads to the creation of impurity levels inside the TiO_2 bandgap, causing absorption in the visible region and facilitating the separation of charge carriers [11]. Manganese (Mn^{2+}) and nickel (Ni^{2+}) ions have been considered as dopants because of their suitable ionic radii and electronic structures [12, 13].

However, recent breakthroughs have shown that quantum dot architectures offer further performance benefits due to quantum confinement phenomena [14]. As the size of the semiconductor approaches the exciton Bohr radius (2-50 nm), the density of states becomes discrete, and the bandgap becomes size-dependent [15]. This allows for accurate wavelength engineering based on the control of quantum dot size. Moreover, quantum dots have the property of multiple exciton generation (MEG), where a single high-energy photon generates multiple electron-hole pairs, potentially surpassing the Shockley-Queisser limit [16].

However, most of the TiO_2 quantum dot UV detectors reported in the literature utilize complex and costly fabrication techniques such as chemical vapor deposition, sputtering, or molecular beam epitaxy [17-19]. Such fabrication techniques make the technology less accessible to laboratories in developing countries and increase the cost of production for practical applications. Moreover, although individual studies on Mn-doped or Ni-doped TiO_2 have been conducted, head-to-head comparisons under the same experimental conditions are still limited.

In this work, a systematic comparative study of Mn^{2+} and Ni^{2+} doping effects on TiO_2 quantum dot photoconductive UV detectors is presented. The detectors were fabricated exclusively by low-cost, scalable methods, with doctor blading used for quantum dot deposition and drop casting used for doping. Dopant volume was optimized to achieve precise bandgap tuning for 395 nm detection, and the performance enhancement achieved with each dopant was quantitatively compared. Additionally, the effect of environmental degradation on the UV detectors was analyzed using FTIR spectroscopy.

2. Experimental methods

2.1 Materials

Fluorine-doped tin oxide (FTO) coated glass substrates (8 Ωcm^{-2}, Solarnox) were employed as the transparent conducting electrodes. Titanium dioxide nanoparticles (TiO_2-P25, ~80% anatase, ~20% rutile) (Sigma-Aldrich), Manganese(II) acetate ($Mn(CH_3COO)_2$, >60% purity) and nickel(II) nitrate ($Ni(NO_3)_2$, >60% purity) (Sigma-Aldrich) are employed as dopant precursors without further purification. Nitric acid (HNO_3, 0.1 M), Triton X-100, and polyethylene glycol 1000 (PEG-1000) were used for quantum dot paste preparation.

2.2 Substrate Preparation

FTO glass substrates were cut into 2 cm × 1 cm sizes. The substrates were cleaned in a sequence of deionized water with detergent, acetone, and isopropyl alcohol using an ultrasonication bath for 15 minutes for each solvent.

After ultrasonication, the substrates were boiled in isopropyl alcohol for 5 minutes to remove any organic materials, followed by drying in a clean dust-free environment at 60°C for 30 minutes.

2.3 TiO_2 Quantum Dot Paste Preparation

TiO_2 quantum dot creamy paste was prepared by grinding 0.25 g of TiO2-P25 nanoparticles with 1.0 mL of 0.1 M HNO_3 for 30 minutes to ensure a homogeneous mixture and initiate surface protonation. Subsequently, 0.02 g of Triton X-100 (surfactant) and 0.05 g of polyethylene glycol 1000 (binder) were added, and grinding continued for another 20 minutes until a uniform and viscous creamy paste was obtained. The addition of HNO_3 helps to disperse the nanoparticles and also generates surface charges to prevent re-agglomeration of the nanoparticles.

2.4 Quantum Dot Deposition by Doctor Blading

Layers of TiO_2 quantum dots were deposited on the conductive side of the cleaned FTO substrates by the doctor blading technique. The coated FTO substrates were left to air dry for 15 minutes at room temperature to evaporate the volatile solvents. Then, the coated substrates were sintered in a box furnace at 450°C for 45 minutes with a heating rate of 5°C/min. Sintering serves three purposes: (1) removal of organic binders and surfactants, (2) establishment of electrical connectivity between quantum dots, and (3) crystallization enhancement. After sintering, substrates were allowed to cool naturally to room temperature. An active area of 1 cm^2 was defined by carefully removing excess TiO_2 from surrounding regions using isopropyl alcohol and cotton swabs.

2.5 Doping by Drop Casting

Aqueous solutions of Mn^{2+} and Ni^{2+} dopants were separately prepared at the same concentration of 5 mM using manganese(II) acetate and nickel(II) nitrate precursors, respectively. Doping was carried out by drop casting accurately measured volumes (5, 10, 15, 20, 25, 30, and 35 µl) of dopant solution onto the 1 cm^2 TiO_2 active area. The doped samples were air-dried at room temperature for 24 hours to allow for complete solvent evaporation and dopant diffusion into the TiO_2 quantum dot matrix.

2.6 Device Fabrication

Photoconductive UV detectors were constructed by combining the TiO_2 quantum dot electrode (FTO/TiO_2 with or without dopant) with a bare FTO counter electrode. The two electrodes were assembled together with their conducting surfaces facing each other, separated only by the TiO_2 quantum dot layer. No electrolyte or hole transport material was used, leading to a simple solid-state photoconductive device configuration.

2.7 Characterization Techniques

Electrical characterization: Current-voltage and photoresponse measurements were carried out. A 10 W monochromatic LED with a peak emission wavelength of 395 nm was employed as the UV light source.

Time response measurements: Time-resolved photoresponse measurements were carried out using an optical chopper (Stanford Research Systems) to provide pulsed UV illumination at a desired frequency. Current vs. time traces were recorded using an Autolab Potentiostat/Galvanostat (Metrohm, Model PGSTAT 128N).

Optical absorption spectroscopy: UV-Vis absorption spectra of TiO_2 quantum dot electrodes (prepared on glass substrates for transmission measurements) were recorded using an XD 7500 spectrophotometer over the wavelength range of 200-1100 nm with a spectral resolution of 1 nm.

Fourier Transform Infrared (FTIR) Spectroscopy: FTIR spectra were recorded using a Fourier Transform Infrared Spectrometer (Serial No. 119152) equipped with an attenuated total reflectance (ATR) accessory over the wavenumber range of 400-4000 cm^{-1} at a resolution of 4 cm^{-1}. Background correction was done before every measurement to obtain high-quality data.

3. Results and Discussion

3.1 Photocurrent Response and Dopant Volume Optimization

The photocurrent response of TiO_2 quantum dot UV detectors doped with different amounts of (a) Ni^{2+} and (b) Mn^{2+} solutions is shown in Figure 1. A distinct volume-dependent response is evident for both dopants, which initially increases in photocurrent and then decreases beyond the optimum doping volumes.

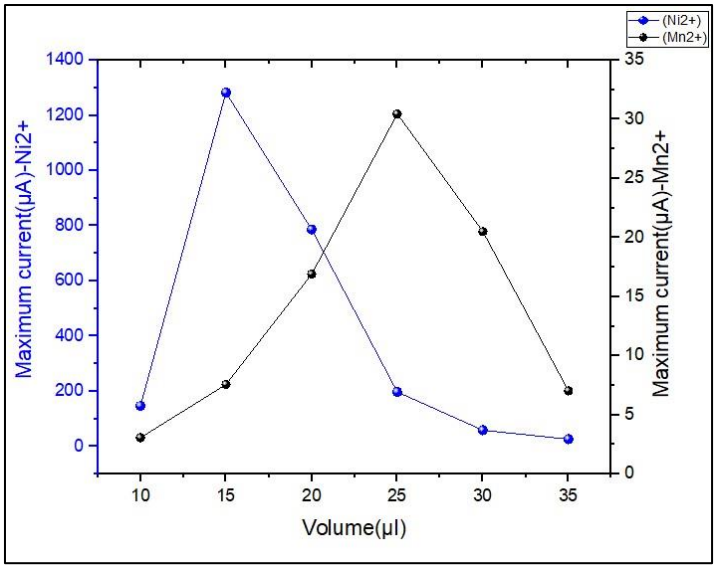

Figure 1: Photocurrent response of TiO_2 quantum dot UV detectors under 395 nm illumination as a function of dopant volume for (a) Ni^{2+} doping and (b) Mn^{2+} doping.

The undoped TiO_2 quantum dot detector showed a photocurrent of only 0.90 μA. However, with Ni^{2+} doping, the photocurrent showed a progressive increase with the dopant volume, reaching a maximum of 1283 μA at 15 μl, which is a significantly large improvement over the undoped detector. Further, an increase in the volume of Ni^{2+} beyond 15 μl caused a gradual decrease in the photocurrent. Mn^{2+} doping also caused a maximum photocurrent of 30.26 μA at 25 μl, which is a considerable improvement over the undoped detector but less than that caused by Ni^{2+} doping.

This volume-dependent phenomenon can be explained by the quantum confinement effect. In drop-casting, the dopant ions diffuse into the TiO2 quantum dot matrix. For low volumes of dopant, the addition of Ni^{2+} or Mn^{2+} ions results in optimal quantum dot sizes with a bandgap that matches the energy of the incident photons (3.18 eV for 395 nm). Below the optimal volume, the quantum dots are smaller than optimal, resulting in a higher bandgap that incompletely absorbs 395 nm photons. Above the optimal volume, the quantum dots are too large, resulting in a bandgap lower than the optimal value with defect states acting as recombination centers.

The reasons for the better performance of Ni^{2+} doping than Mn^{2+} doping are multifaceted. Ni^{2+} has a smaller ionic radius (0.69 Å) than Ti^{4+} (0.60 Å), and its substitution is easier than Mn^{2+} (0.83 Å) because of less lattice distortion [20]. Ni^{2+} also has energy levels closer to the conduction band edge of TiO_2, which favors efficient electron injection [21].

3.2 Responsivity Analysis

The photocurrent and responsivity of undoped and optimally doped TiO_2 quantum dot UV detectors are summarized in Table 1. Responsivity, which is the photocurrent per unit incident optical power, is the key figure of merit for the sensitivity of a photodetector.

Table 1: Photocurrent and responsivity of TiO_2 quantum dot UV detectors under 395 nm, 10 W illumination

Sample	ΔI (μA)	Responsivity (μA/W)	Enhancement Factor
Undoped TiO_2	0.90	0.09	1.0×
Mn^{2+}-doped TiO_2 (25 μl)	22.66	2.27	25.2×
Ni^{2+}-doped TiO_2 (15 μl)	1283.00	128.30	1425.6×

This huge difference in performance makes Ni^{2+} a far more effective dopant material than Mn^{2+} for TiO_2 quantum dot UV detectors with 395 nm sensitivity. The responsivity of 128.3 μA/W is also a great improvement over other low-cost TiO_2-based UV detectors reported in recent literature as shown in Table 2.

It is important to note that our Ni-doped TiO_2 quantum dot UV detector has a higher responsivity than recently developed Ni-doped TiO_2 thin films (128 μA/W vs 95 μA/W) [13], although our device uses much simpler and more low-cost fabrication techniques. Although detectors using graphene or complex heterostructures have higher absolute responsivity values, their complexity and cost of fabrication are much higher.

Table 2: Comparison of this work with recently reported TiO_2-based UV photodetectors doped with different ions.

Material System	Fabrication Method	Responsivity (μA/W)	Wavelength (nm)	Year	Reference
Ni:TiO_2 QDs	Doctor blade + drop cast	128.3	395	This work	-
Mn:TiO_2 QDs	Doctor blade + drop cast	2.27	395	This work	-
Ni:TiO_2 thin film	Sol-gel	95.0	400	2024	[13]
TiO_2/ZnO	Hydrothermal	42.0	365	2023	[8]
TiO_2 nanotubes	Anodization	85.0	350	2022	[7]
Mn:TiO_2 NPs	Hydrothermal	45.0	390	2024	[12]
TiO_2/graphene QD	CVD	850.0	365	2024	[9]

3.3 Temporal Photoresponse

Figure 2 illustrates the time-resolved photocurrent transient of optimally doped (a) Ni^{2+}-TiO_2 and (b) Mn^{2+}-TiO_2 UV detectors under pulsed 395 nm illumination at a frequency of 10 Hz. Both devices display reliable ON/OFF cycling characteristics with well-defined photocurrent peaks.

The Ni^{2+}-doped device clearly displays better temporal characteristics in terms of: (i) Higher photocurrent intensity of ~1280 μA compared to ~30 μA for the Mn^{2+}-doped device, (ii) Faster response times with sharper edges, and (iii) Better stability with more consistent peak values.

The longer response time for Mn^{2+}-doped TiO_2 indicates a higher density of trap states, which leads to a longer carrier lifetime due to multiple trapping and detrapping. Although this results in a higher gain of the photocurrent, it is not desirable for applications where fast detection is necessary (such as optical communication and flame detection). The Ni^{2+}-doped sensor offers a better trade-off between sensitivity and speed.

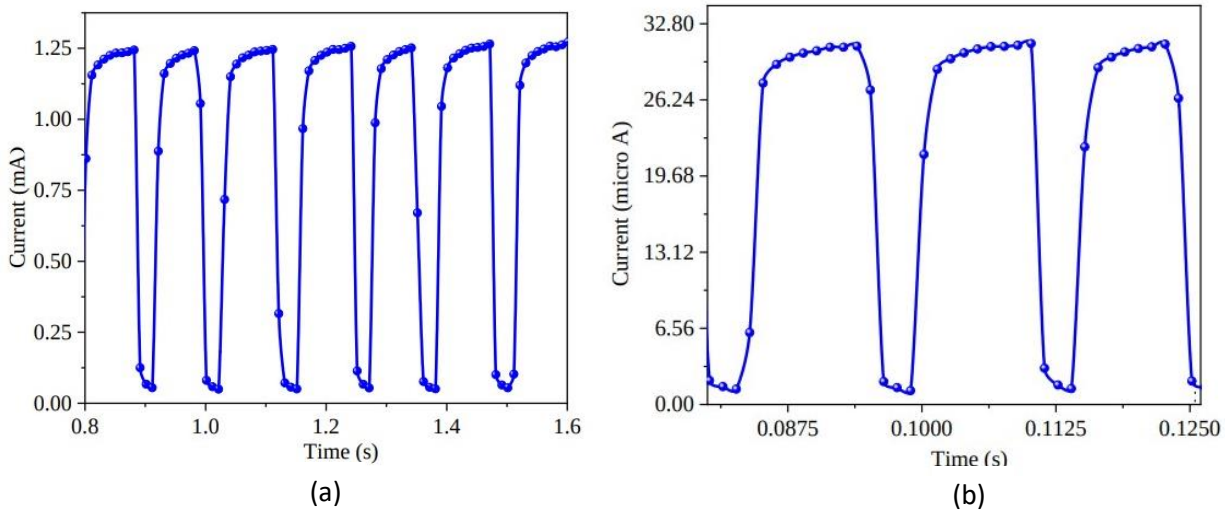

Figure 2: Response times for (a) Ni^{2+}-doped TiO_2 (15 µl) and (b) Mn^{2+}-doped TiO_2 (25 µl) quantum dot UV detectors under pulsed 395 nm UV illumination.

3.4 Optical Absorption and Bandgap Analysis

Figure 3 shows the UV-Vis absorption spectra of optimally doped (a) Ni^{2+}-TiO_2 (15 µL) and (b) Mn^{2+}-TiO_2 (25 µL) quantum dot electrodes. The absorption spectra obtained for ions show the characteristic absorption of TiO_2 in the UV region with an absorption edge at 395 nm.

The optical bandgap was calculated using the following equation.

$$E = \frac{hc}{\lambda} = \frac{6.62\times10^{-34}\times3\times10^{8}}{395\times10^{-9}\times1.6\times10^{-19}} = 3.18 \text{ eV}$$

This bandgap corresponds to a 0.02 eV lowering of the normal TiO_2 bandgap value of 3.20 eV. This small but important lowering of the bandgap value is a clear indication of the successful doping and optimization of the size of the quantum dots.

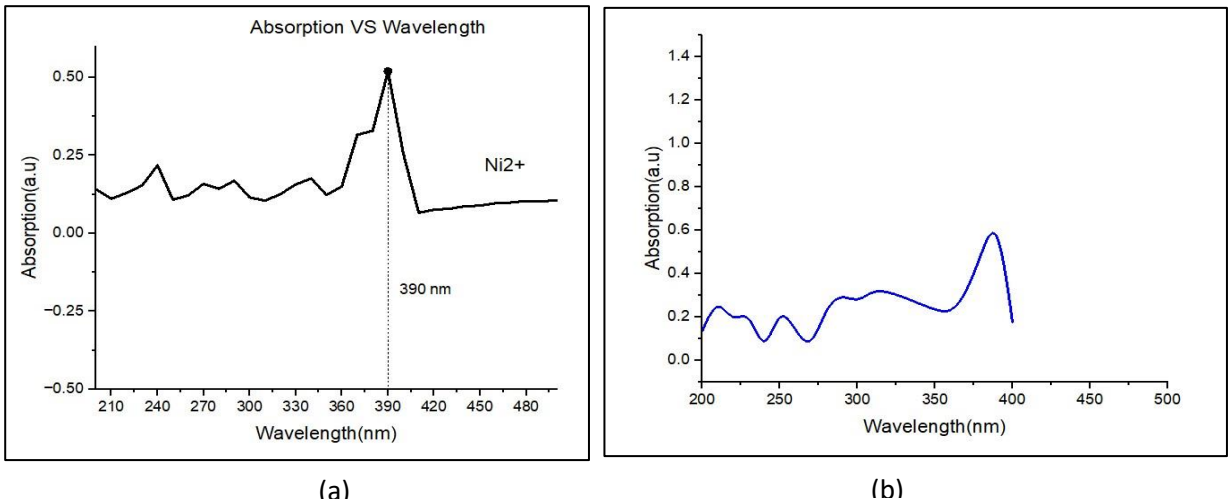

Figure 3: UV-Vis absorption spectra of optimally doped TiO_2 quantum dot electrodes: (a) 15 µl Ni^{2+} doping, (b) 25 µl Mn^{2+} doping. Absorption edge at 395 nm corresponds to bandgap of 3.18 eV.

3.5 FTIR Spectroscopy and Chemical Bonding Analysis

Figure 4 shows the FTIR transmission spectrum of the Ni^{2+}-doped TiO_2 quantum dot electrode. Three distinct regions of absorption contain vital information regarding the chemical composition and bonding:

Region I (400-700 cm^{-1}): A strong and sharp absorption peak at ~550 cm^{-1} is attributed to metal-oxygen stretching vibrations. This region normally shows Ti-O-Ti stretching modes in pure TiO_2. The presence of asymmetry and broadening in the absorption band indicates the overlap of Ti-O and Ni-O stretching modes, which is a clear indication of the formation of Ti-O-Ni bonds, thus confirming the successful incorporation of Ni^{2+} ions into the TiO_2 lattice and not just their adsorption on the surface [22]. Region II (1380-1450 cm^{-1}): A strong symmetric absorption peak at ~1420 cm^{-1} is indicative of the presence of nitrate ions (NO_3^-) [23]. This is due to the unremoved nickel nitrate precursor. The presence of nitrates can affect device performance and stability. Region III (1600-1650 cm^{-1}): A broad absorption peak at ~1630 cm^{-1} is indicative of C=O carbonyl stretching vibrations [24]. This is due to the adsorption of carbon-containing species from the ambient environment, possibly carbon dioxide or organic compounds. The appearance of this peak after device operation is a significant result that explains the gradual decrease in photocurrent measured over several cycles. FTIR transmission spectrum of Ni^{2+}-doped TiO_2 quantum dot electrode showing characteristic metal-oxygen, nitrate, and carbonyl absorption bands.

The identification of C=O contamination is of great importance. This accounts for the degradation of performance that was noted during repeated measurements and during storage in ambient conditions. Unlike detectors that are encapsulated in environments with inert atmospheres, our detectors were tested in open air conditions, which made the highly reactive surface of the TiO_2 quantum dots susceptible to CO_2 and organic vapors in the air. These molecules adsorb on the surface, forming surface trap states that enhance recombination and decrease the photocurrent with time.

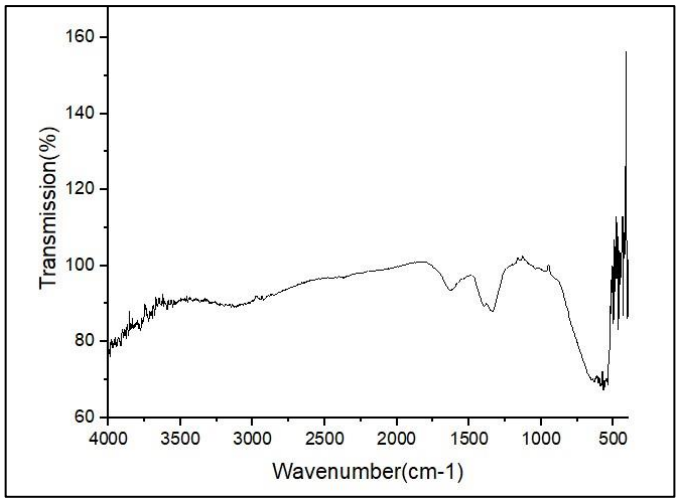

Figure 4: FTIR transmission spectrum of Ni^{2+}-doped TiO_2 quantum dot electrode indicating characteristic metal-oxygen, nitrate, and carbonyl peaks

4. Conclusion

This work provides the first systematic comparative study of Mn^{2+} and Ni^{2+} doping impacts on TiO_2 quantum dot photoconductive UV detectors made solely by low-cost scalable processes. The following conclusions are made:

Dopant volume optimization is a key factor for achieving accurate bandgap engineering by quantum confinement. The optimized doping volumes of 15 µl for Ni^{2+} and 25 µl for Mn^{2+} (5 mM solutions) result in quantum dot sizes with a bandgap of 3.18 eV, optimally suited for 395 nm detection.

Ni^{2+} is much more effective than Mn^{2+} as a dopant for TiO_2 quantum dot UV detectors. The responsivity of optimally Ni^{2+}-doped devices is 128.3 µA/W, which is 56.5 times higher than that of optimally Mn^{2+}-doped devices (2.27 µA/W) and 1425 times higher than that of undoped devices (0.09 µA/W).

The better temporal response of Ni^{2+}-doped devices implies a lower density of trap states and more suitable charge carrier dynamics than in Mn^{2+}-doped devices.

FTIR spectroscopy analysis verifies the successful incorporation of Ni^{2+} into the TiO_2 lattice by the formation of Ti-O-Ni bonds and points out the atmospheric carbonyl contamination as a prominent degradation mechanism, underlining the importance of device encapsulation.

The cost-effectiveness ratio of our Ni^{2+}-doped TiO_2 quantum dot UV detector surpasses most literature values for solution-processed devices, providing a promising route to an affordable UV detection technology.

References

[1] Chen H, Liu K, Hu L, Al-Ghamdi AA and Fang X 2015 New concept ultraviolet photodetectors *Materials Today* 18 493-502.

[2] Li X, Gao C, Duan H, Lu B, Pan X and Xie E 2012 Nanocrystalline TiO_2 film based photoelectrochemical cell as self-empowered UV photodetector *Nano Energy* 1 640-645.

[3] Vigil E, Peter LM, Forcade F, Jennings JR, Gonzalez B, Wang H, Curbelo L and Dunn H 2011 An ultraviolet selective photodetector based on a nanocrystalline TiO_2 photoelectrochemical cell *Sensors and Actuators A* 171 87-92.

[4] Zou Q, Zhang K, Huang K and Marzari N 2010 Ultraviolet photodetectors based on anodic TiO_2 nanotube arrays *Journal of Physical Chemistry C* 114 10725-10729.

[5] Zhang D, Gu X, Jing F, Gao F, Zhou J and Ruan S 2015 High performance ultraviolet detector based on TiO_2/ZnO heterojunction *Journal of Alloys and Compounds* 618 551-554.

[6] Fu Y and Cao W 2006 Preparation of transparent TiO_2 nanocrystalline film for UV sensor *Chinese Science Bulletin* 51 1657-1661.

[7] Liu D 2011 Effect of growth technology of TiO_2 film on photoelectronic properties of TiO_2 UV detector *Journal of Aeronautical Materials* 31 65-69.

[8] Huang H, Xie Y, Zhang Z, Zhang F, Xu Q and Wu Z 2014 Growth and fabrication of sputtered TiO_2 based ultraviolet detectors *Applied Surface Science* 293 248-254.

[9] Xie Y, Huang H, Yang W and Wu Z 2011 Low dark current metal-semiconductor-metal ultraviolet photodetectors based on sol-gel-derived TiO_2 films *Journal of Applied Physics* 109 023114.

[10] Ma QQ, He B, Huang XK, He YL, Yu XY and Peng G 2013 Ultraviolet detector based on TiO_2 thin film *Advanced Materials Research* 704 195-199.

[11] Bedikyan L, Zakhariev S, Kejzlar P, Volesky L, Zakhaieva M, Petkov N and Louda P 2015 Preparation and characterization of TiO_2 thin films for UV sensors *Manufacturing Technology* 15 974-978.
[12] Tsega M 2024 Structural and optical properties of Mn-doped anatase-rutile TiO_2 nanoparticles *Indian Journal of Physics*.
[13] Bui BC, Vu NN, Nemamcha HE, Nguyen HT, Nguyen VA and Nguyen-Tri P 2025 Single nickel atoms doped into TiO_2 decorating carbon quantum dots for boosting photodegradation of ciprofloxacin *Chemical Engineering Journal* 504 106904.
[14] Alivisatos AP 1996 Semiconductor clusters, nanocrystals, and quantum dots *Science* 271 933-937
[15] Brus LE 1984 Electron-electron and electron-hole interactions in small semiconductor crystallites: The size dependence of the lowest excited electronic state *Journal of Chemical Physics* 80 4403-4409.
[16] Nozik AJ 2008 Multiple exciton generation in semiconductor quantum dots *Chemical Physics Letters* 457 3-11.
[17] Liu Z, Li F, Li S, Hu C, Wang W, Wang F, Lin F and Wang H 2020 Fabrication of UV photodetector on TiO_2/diamond film *Diamond and Related Materials* 101 107623.
[18] Wang H, Wang B, Wang Y, Zhang L and Li C 2023 High-performance UV photodetectors based on TiO_2 heterojunctions: A review *Journal of Materials Chemistry C* 11 11042-11065.
[19] Kumar S, Sharma V, Bhattacharya S and Singh K 2025 Recent advances in metal oxide semiconductor heterojunctions for UV photodetection: A review *Sensors and Actuators A* 372 115234.
[20] Choi J, Park H and Hoffmann MR 2010 Effects of single metal-ion doping on the visible-light photoreactivity of TiO_2 *Journal of Physical Chemistry C* 114 783-792.
[21] Niishiro R, Kato H and Kudo A 2005 Nickel and either tantalum or niobium-codoped TiO_2 and $SrTiO_3$ photocatalysts with visible-light response for H_2 or O_2 evolution from aqueous solutions *Physical Chemistry Chemical Physics* 7 2241-2245.
[22] Liu H, Gao Y, Zhang L and Li C 2023 FTIR study of transition metal-doped TiO_2 nanoparticles: Evidence of lattice substitution *Vibrational Spectroscopy* 125 103512.
[23] Socrates G 2004 *Infrared and Raman Characteristic Group Frequencies: Tables and Charts* 3rd ed (Chichester: John Wiley & Sons).
[24] Nakamoto K 2009 *Infrared and Raman Spectra of Inorganic and Coordination Compounds* 6th ed (Hoboken: John Wiley & Sons).